BNWL-1315-1
UC-41

[redacted]

NUCLEAR SAFETY QUARTERLY REPORT
NOVEMBER, DECEMBER, 1969, JANUARY 1970
FOR
USAEC DIVISION
OF REACTOR DEVELOPMENT AND TECHNOLOGY

March 1970

[redacted]

AEC RESEARCH & DEVELOPMENT REPORT

BNWL-1315-1

BATTELLE NORTHWEST
BATTELLE MEMORIAL INSTITUTE PACIFIC NORTHWEST LABORATORIES
BATTELLE BOULEVARD, P. O. BOX 999, RICHLAND, WASHINGTON 99352

LEGAL NOTICE

PACIFIC NORTHWEST LABORATORY
RICHLAND, WASHINGTON
operated by
BATTELLE MEMORIAL INSTITUTE
for the
UNITED STATES ATOMIC ENERGY COMMISSION UNDER CONTRACT AT(45-1)-1830

AEC-RL RICHLAND, WASH.

BNWL-1315-1
UC-41, Health and Safety

NUCLEAR SAFETY QUARTERLY REPORT
NOVEMBER, DECEMBER, 1969, JANUARY 1970

FOR

USAEC DIVISION OF REACTOR DEVELOPMENT AND TECHNOLOGY

By

The Staff of Battelle-Northwest

March 1970

BATTELLE MEMORIAL INSTITUTE
PACIFIC NORTHWEST LABORATORIES
RICHLAND, WASHINGTON 99352

Printed in the United States of America
Available from
Clearinghouse for Federal Scientific and Technical Information
National Bureau of Standards, U.S. Department of Commerce
Springfield, Virginia 22151
Price: Printed Copy $3.00; Microfiche $0.65

NUCLEAR SAFETY QUARTERLY REPORT
NOVEMBER, DECEMBER, 1969, JANUARY 1970
FOR
USAEC DIVISION OF REACTOR DEVELOPMENT AND TECHNOLOGY

By
The Staff of Battelle-Northwest

FOREWORD

This report is the twelfth of a series in which Pacific Northwest Laboratories reports its nuclear safety-related studies being performed for the USAEC Division of Reactor Development and Technology.

PREVIOUS REPORTS IN THIS SERIES

BNWL-433	January, February, March	1967
BNWL-537	April, May, June	1967
BNWL-754	July, August, September, October	1967
BNWL-816	November, December, 1967, January	1968
BNWL-885	February, March, April	1968
BNWL-894	May, June, July	1968
BNWL-926	August, September, October	1968
BNWL-1009	November, December, 1968, January	1969
BNWL-1084	February, March, April	1969
BNWL-1187	May, June, July	1969
BNWL-1266	August, September, October	1969

CONTENTS

NUCLEAR SAFETY QUARTERLY REPORT
NOVEMBER, DECEMBER, 1969, JANUARY 1970
FOR
USAEC DIVISION OF REACTOR DEVELOPMENT AND TECHNOLOGY

By
The Staff of Battelle-Northwest

1. SUMMARY

ENGINEERED SAFETY SYSTEMS STUDIES

Containment Systems Experiment (CSE)

Two large scale runs to evaluate the performance of recirculating air cleaning systems were completed in the CSE containment vessel during the quarter. The initial containment atmosphere comprised saturated steam and air at 250 °F and about 48 psia. In both runs the air cleaning system included a high efficiency particle filter and three charcoal filters. One run included a heat exchanger and demister at the inlet of the air cleaning system. In the other run, these two components were omitted to evaluate the effect of larger moisture loadings on the filter components.

In both runs, concentrations of airborne iodine forms and particles decreased in close agreement with predictions made assuming a well mixed atmosphere and 100% filtering efficiency. Elemental iodine was removed somewhat more rapidly than predicted with these assumptions, and this behavior is attributed to the increased removal by natural processes because of higher gas phase velocities when the air cleaning system operates.

The initial removal rates continued until airborne concentrations were less than 1% of initial values. Further removal continued, but at a slower rate. Operation of the

loop without the heat exchanger and demister did not reduce loop cleanup effectiveness; although the pressure drop did increase with time.

The distribution of iodine between gas and liquid phases is a critically important factor in determining the iodine removal from containment vessel atmospheres by both spray systems and natural transport. Two experiments were performed in 900 liter stainless steel vessel to investigate gas-liquid partition of iodine for a pH 9.5 base-borate solution at 80 °C. The prime difference in the runs was that in one run, the elemental iodine was released into the gas phase. In the other, release was to the liquid phase. The liquid was recirculated through a spray header with about an 8-min liquid turnover time to achieve rapid equilibrium between the gas and liquid phases. Gas phase samples were collected frequently with CSE Maypacks, and analyzed for both inorganic and organic forms. Total iodine was also determined frequently in liquid samples.

Tentative conclusions made from these experiments on pH 9.5 base borate systems at 80 °C are; (1) the transfer mechanisms for volatile iodine forms are reversible, (2) the overall partition coefficient for inorganic forms of iodine was about 6500 at zero time, **(3)** the coefficient increases slowly with time as a result of a slow (400-min half time) reaction which depletes volatile species, and (4) the physical partition coefficient of an unidentified inorganic species (perhaps HOI) was about 30.

Six blowdown experiments with no internals in the CSE reactor simulator vessel were made during the quarter. The major purpose of this series was to measure liquid level and liquid swelling behavior for comparison with predictions of computer codes. In addition, measurements were made of fluid void fraction in the exit pipe and high-speed movies were taken of bubbles in the exit to measure bubble size and velocity.

Data from the current runs, together with that of earlier runs with the dummy core plate installed, have shown that FLASH2 predictions of liquid mass remaining at the end of blowdown from middle and top nozzles are in error in a non-conservative direction. There is evidence that the magnitude of the error has a dependence on break size (or ratio of break size to vessel cross section), and the error is larger for runs with the dummy core plate.

Initial high-speed photography data on size and velocity of bubbles in the exit pipe were obtained, and some degree of agreement found between the fluid quality inferred from observed bubble sizes and numbers and that inferred from the neutron densitometer void fraction data.

PRESSURE BEARING COMPONENT EVALUATION AND MONITORING STUDIES

Crack Detection in Pressure Piping by Acoustic Emission

Investigation of acoustic emission signal propagation in pipe specimens has shown that propagation characteristics in pipes can be unique from that in flat plates. Wall thickness, wall thickness to diameter ratio, and helical propagation paths are significant factors. It appears that plate wave theory will permit selecting a detection arrangement for a given configuration which will minimize propagation velocity ambiguities and thus enhance general source location accuracy.

Limited additional work to investigate the effect of temperature on generation of detectable emission in stainless steel has shown no discernible effect up to 600 °F.

FIXATION OF RADIOACTIVE RESIDUES

To date, 27 radioactive demonstrations in WSEP have been completed with simulated wastes containing approximately 41 MCi of mixed radionuclides being converted to solids.

During the report period, the eleventh and final phosphate glass demonstration run in WSEP was completed. An

LMFBR Waste simulating core fuel only (100,000 MWd/tonne at 200 MW/tonne) and aged 1.5 years was successfully processed to produce a solidified waste having a heat rate density of 196 W/liter. Equipment problems were encountered with a newly installed screw feeder (for delivering feed to the melter) and with alignment of the melt stream to give an unimpaired entry into the receiver pot. During the eleven phosphate glass runs, a total of 19.3 MCi of radioactivity has been interfused into 630 liters of solidified product.

A fast reactor waste flowsheet operable in the spray solidifier was developed. Substitution of aluminum for 20% of the iron and addition of 20% excess rare earths to the waste did not affect the melt viscosity or feed flow stability appreciably.

A study was initiated to determine the effects of recycling secondary waste streams (recovered acid and water) from solidification to a fuel reprocessing plant as makeup water and acid for dissolution and first solvent extraction cycles.

The relative volatilities of antimony, selenium, tellurium, and tin from LMFBR wastes were determined for the phosphate glass and spray solidification processes. Antimony and tin were not volatile. About 5% of the tellurium and 50% of the selenium was found in the phosphate glass melter condensate, and about 30% of the selenium was found in the spray solidifier condensate.

Solids Storage Engineering Test Facility exposure of the waste container from pot calcination demonstration Run PC-6, in air and at a maximum temperature of 600 °C, was started.

Regression analysis of spray solidification product thermal conductivity data revealed that a value of 1.2 $W/(m^2)$ (°C/m) can be used as a value for effective thermal conductivity

(k_{eff}) over the temperature range 100 to 600 °C. Corresponding work showed that for phosphate glass product, k_{eff} [(W/(m^2)(°C/m)] equals 0.719 + 6.630 × 10^{-4}t, where t(°C) is the average product temperature.

HEAVY SECTION STEEL TECHNOLOGY PROGRAM

Irradiation Effects on the Fracture of Heavy Section Pressure Vessel Steels

Planning, engineering, and procurement has been completed for the installations of electrical heaters in the ETR M-3 loop to provide greater temperature flexibility during specimen irradiation. Postirradiation annealing of A533-B pressure vessel steel specimens revealed that the reduction of irradiation hardening commenced above 540 °F and was 70% complete by 650 °F. A fluence increase from 2 to 4.4 × 10^{19} n/cm^2 (E > 1 MeV) produced only a modest increase in strength. The fatigue crack behavior indicated the propensity for crack propagation hindrance.

2. ENGINEERED SAFETY SYSTEMS STUDIES

CONTAINMENT SYSTEMS EXPERIMENT - G. J. Rogers

Fission Product Transport Studies - R. K. Hilliard, J. D. McCormack, and L. F. Coleman

Large Air Cleaning System Experiments - J. D. McCormack

Demonstration tests of air cleaning systems operating in postaccident environments were continued in the Containment Systems Experiment (CSE). Two experiments were made during the current reporting period, both with internally located, recirculation type filter loops operating in a 250 °F saturated steam-air atmosphere at about 48 psia. The salient features of each test are listed in Table 2.1.

A full set of filter loop components, typical of systems used in many PWRs, was used in Run A-14. In Run A-15 the heat exchanger and demister were removed to demonstrate the effect of operation without these components.

New loop components were installed before each run. The heat exchanger used for Run A-14 was a copper finned unit, four tubes deep by six tubes high, with a face area of 4.1 ft^2 and an estimated fin area of 163 ft^2. With the loop operating at 1000 actual ft^3/min, about 4300 Btu/min were removed from the inlet steam-air, resulting in a AT of about 2.5 °F. The demister* was made of Teflon yarn—stainless steel wire mesh and was 18 in. in diameter by 2 in. thick. Flow was upward through the mesh. Other filter loop components (prefilter, HEPA filter and charcoal beds) were described in a previous report.(1)

After installation in the containment vessel (but before use) the loop and components were tested at room temperature and pressure for leakages, with results as shown in Table 2.2.

---

* *York-type 321-SR, Otto H. York Company, West Orange, New Jersey.*

TABLE 2.1. Summary of Test Conditions

CSE Run Number:	A-14	A-15
Date:	10-14-69	11-11-69
Containment Atmosphere:	Sat'd steam-air	Sat'd steam-air
Temperature, °F	250	250
Pressure, psia	48	48
Loop flow, acfm	1000 to 500	1000
Flow duration, min.	1000	2500
Loop Components:	Heat exchanger Demister Prefilter HEPA filter (3) charcoal beds each 1 in. deep	Prefilter HEPA Filter (3) charcoal beds each 1 in. deep
Vessel Volume, Main Room:	595 m^3	21,000 ft^3
Middle Room:	59 m^3	2,090 ft^3
Lower Room:	96 m^3	3,385 ft^3
Aerosol Release:	10 minute except UO_2 20 minutes	Same
Aerosol Conc., Initial in Main Room, $\frac{mg}{m^3}$: Iodine[a]	90	100
CH_3I	5	5,5[b]
Cesium	3	1.5
U-Zr	1.5	2

a. *Excludes CH_3I.*

b. *Two CH_3I releases were made.*

TABLE 2.2. Filter Loop Leakage Tests, Pre-Run

	A-14	A-15
Duct in-leakage, %[a]	0.01	0.02
DOP penetration, %	<0.03	<0.03
CH_3I penetration, %	0.02	0.001

a. % of *flow at estimated operating AP.*

After the integrity of the loop and components was demonstrated, the CSE vessel was brought to 250 °F with steam and the fission product simulant aerosol was released. After allowing 30 min for sampling to determine the removal rate by natural processes, the air cleaning loop fan was started. Sampling of the vapor and liquid stream continued for the duration of the runs, so that the removal rate and loop effectiveness could be determined.

Typical gas space concentrations versus time are plotted in Figures 2.1 and 2.2 for the two runs. Most of the removal of material from the gas had been accomplished by 200 min. The methyl iodide increase late in Run A-14 resulted from combined effects of transfer from the middle room to the main room, by diffusion and by flow caused by decreasing main room temperature when the steam feed stopped.

Heating of the charcoal beds by water adsorption was noted when the steam flow started through the dry charcoal beds. A peak AT of 34 °F was noted in Run A-15, decreasing to 1 °F in about 60 min. The heating of the charcoal beds reduced the humidity of the air during the initial CH_3I removal, as shown in Figure 2.3, and may be an important factor in the bed performance. To test CH_3I removal by water-saturated charcoal beds at 100% RH, a second CH_3I release was made late in Run A-15 when the bed heating had abated. Figure 2.4 indicates that moisture-saturated charcoal reduced the radioactivity of the CH_3I with a 19 min half-time rather than 14.7 as during the first release. This is equivalent to about 77% efficiency and demonstrates that a recirculating loop can effectively reduce the concentration even while operating at a reduced efficiency. The iodine impregnated charcoal (BC 727) reduced the radioactive methyl iodide by isotopic exchange. However, inspection of the total CH_3I concentration as measured by gas

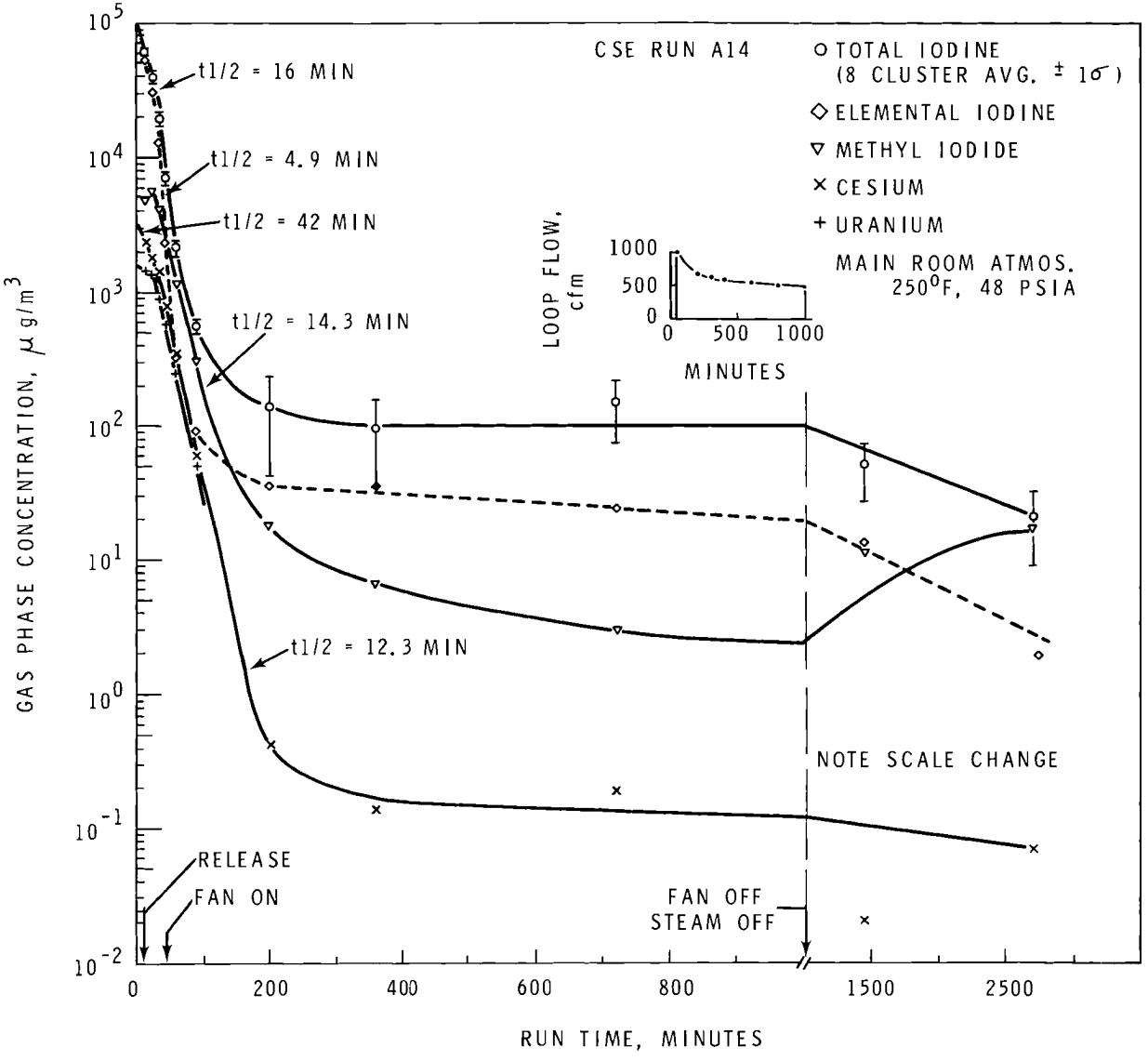

FIGURE 2.1. Main Room Gas Phase Concentration, Run A-14

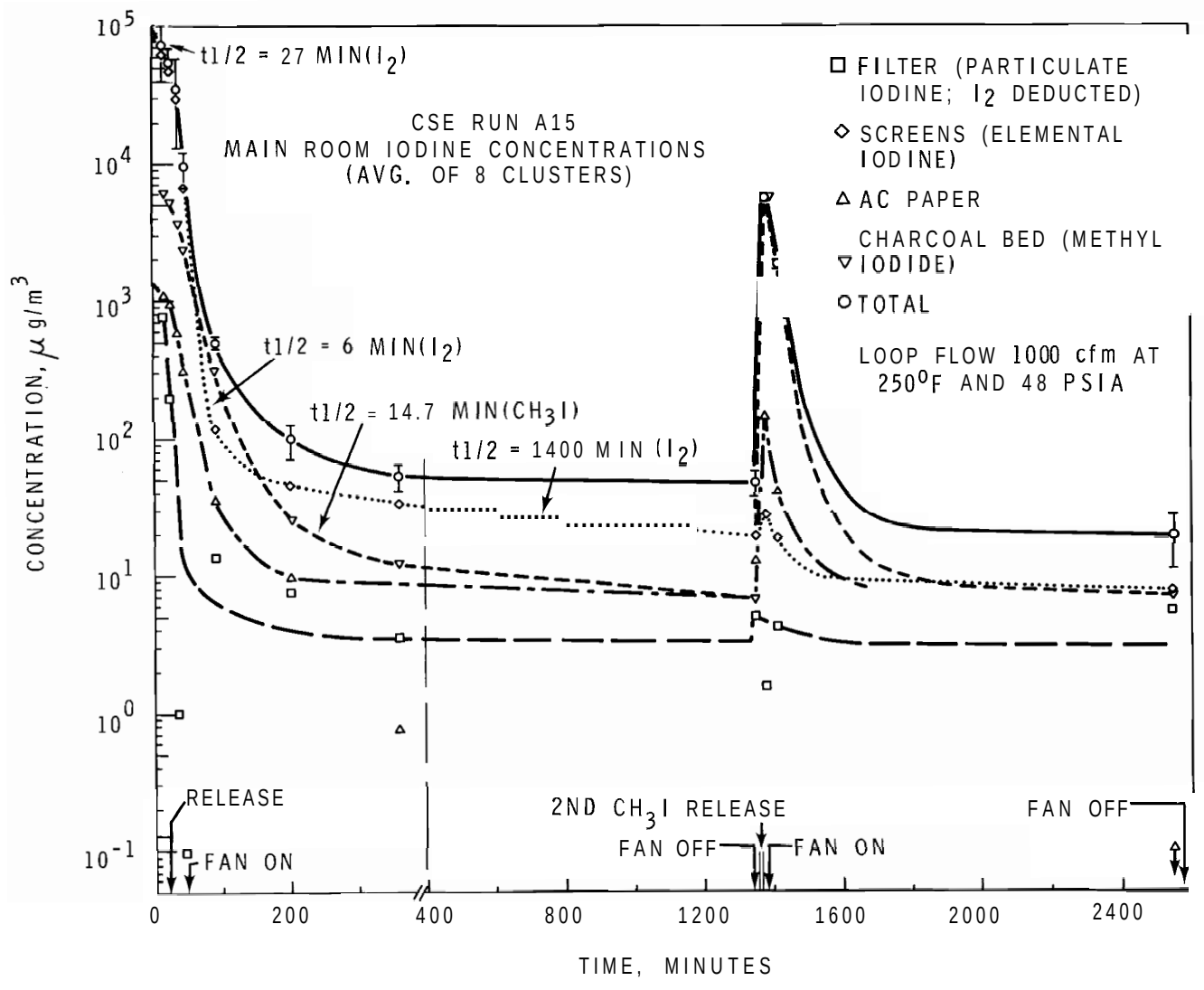

FIGURE 2.2. Main Room Gas Phase Iodine Concentration, Run A-15

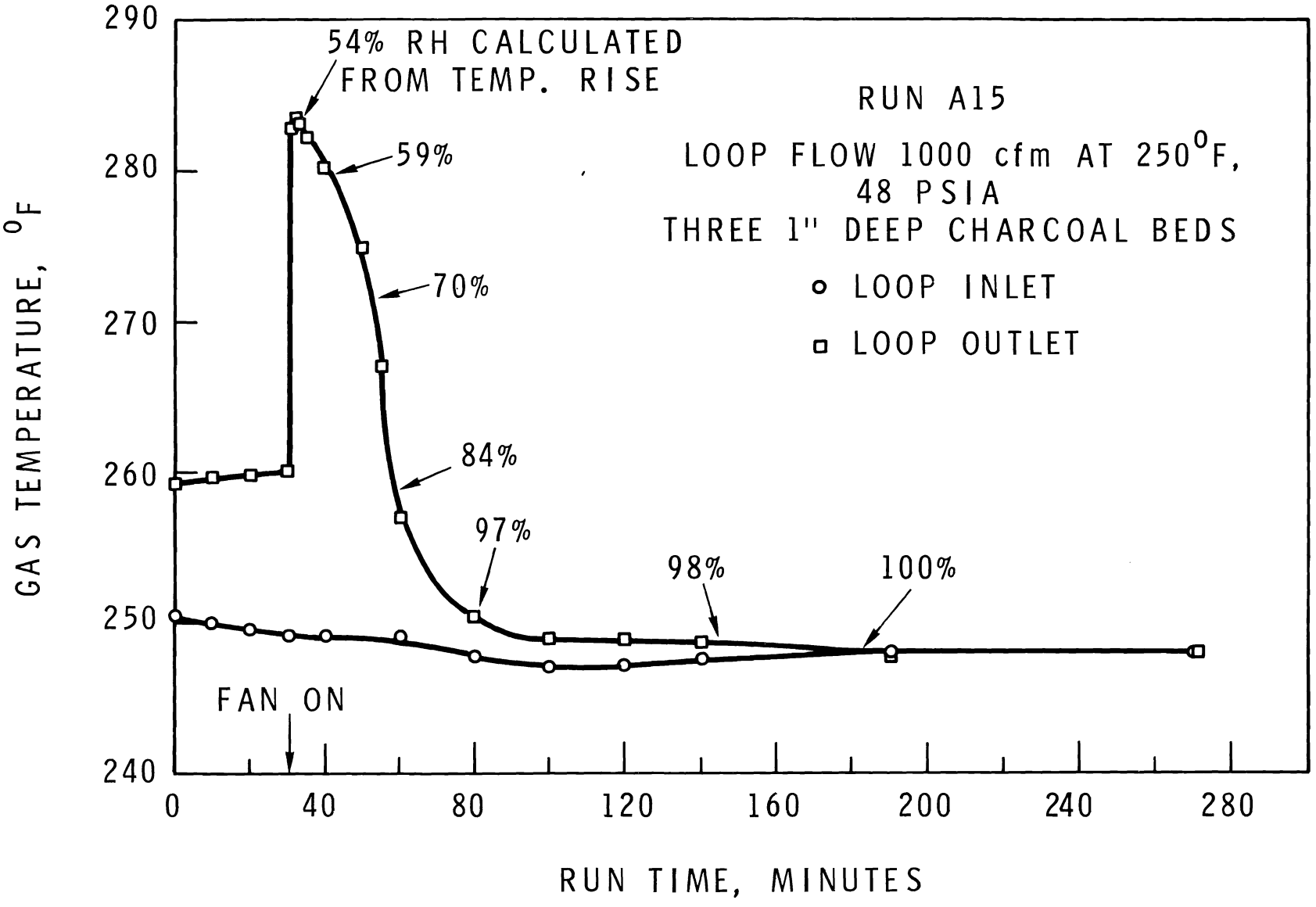

FIGURE 2.3 Heating Resulting from Moisture Adsorption on Charcoal Beds, Run A-15

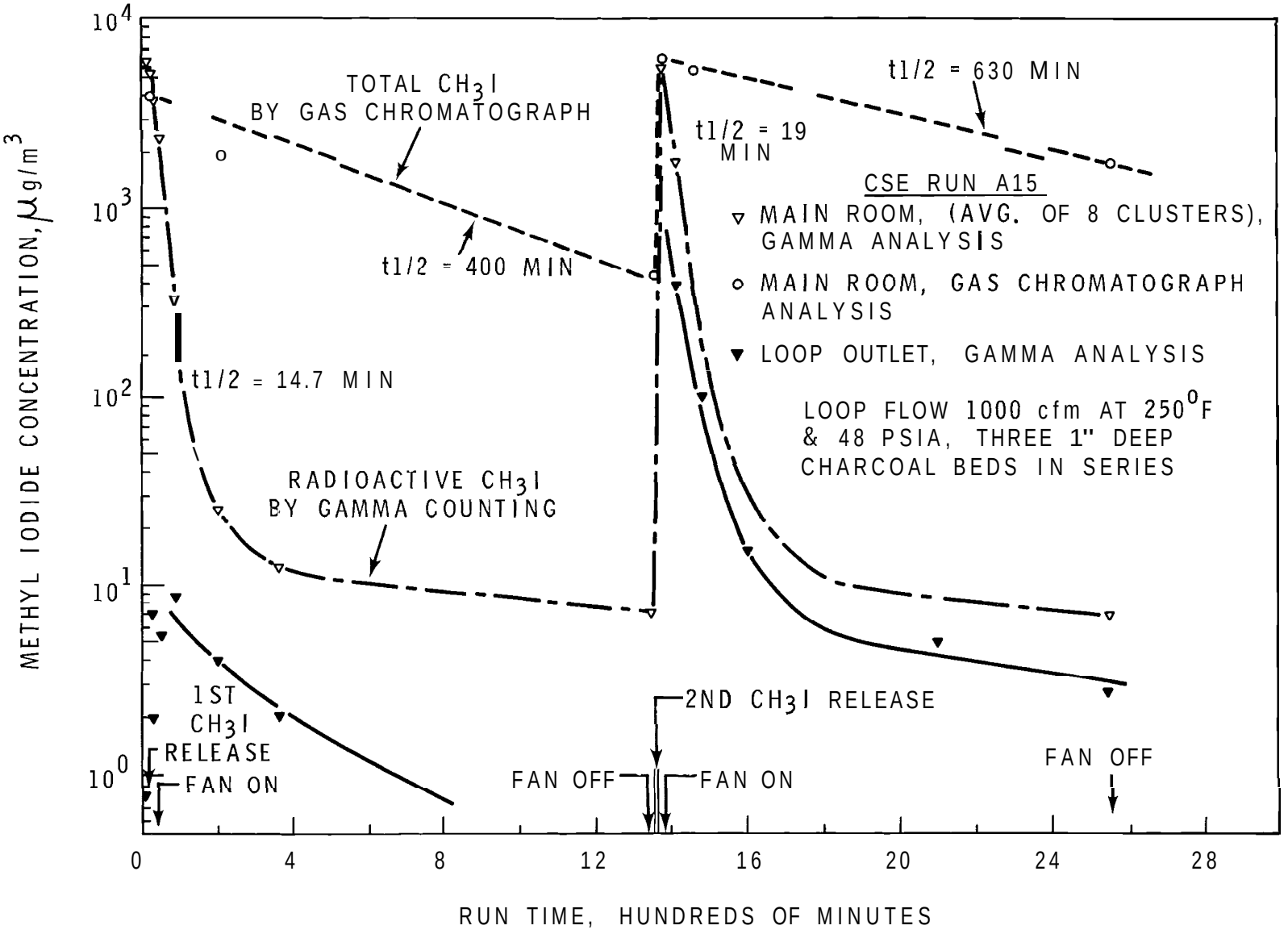

FIGURE 2.4. Methyl Iodide Removal by Impregnated Charcoal, Run A-15

WL-1315-1

chromatography also shows removal by adsorption, although at a slower rate. The loop outlet concentrations are also shown. The removal of material from the gas space is summarized in Table 2.3.

TABLE 2.3. Aerosol Behavior in CSE Runs A-14 and A-15

	Concentration Half-Time, min							
	Natural[a]		Natural Plus Loop[b]		Loop[b] Only		C/C_o[d] at 1000 min	
	A-14	A-15	A-14	A-15	A-14	A-15	A-14	A-15
Total Iodine	-	-	-	-	-	-	1×10^{-3}	5×10^{-4}
Elemental Iodine	16	27	4.9	6	7.1	7.7	2×10^{-4}	2×10^{-4}
Particulate Iodine	27	27	9	10.3	13.5	16.7	3×10^{-3}	3×10^{-3}
Methyl Iodide	∞	∞	14.3	14.7	14.3	14.7	1×10^{-3}	1×10^{-3}
Cesium	42	85	12.3	11	17.4	12.5	3×10^{-4}	$<1 \times 10^{-4}$
Uranium	85	90	13	12	15.4	13.9		$<5 \times 10^{-4}$
Average					13.5	13.1		
Calc. $t_{1/2}$, = 0.693 V/F, min					13.5[c]	14.6		

a. *0 to 30 min. Loop started at t = 30 min*

b. *30 to 100 min*

c. *at 30 min*

d. *C = Concentration at time t*
C_o = Concentration at time t_o

Excellent agreement with the half-time calculated on the basis of a well mixed gas space and 100% efficiency is noted. Elemental iodine, however, was removed faster than predicted, apparently resulting from enhanced deposition on surfaces caused by increased gas velocities which result from the loop operation. After each test the loop was DOP tested (and CH_3I

tested in Run A-14) and the components sampled for iodine and cesium to determine the amount of materials removed by various sections of the loop. This is shown in Table 2.4 as a percentage of the amount airborne in the main room when the loop flow was started. A calculated total percentage on the loop is given, based on the observed removal rates. The amount recovered is consistently higher than that calculated, caused in part from transport to the main room from the middle room and possibly induced by iodine desorption from surfaces. Neither of these sources was considered in the simple model used.

The iodine distribution through the charcoal is quite different in Run A-15 than in A-14. Two explanations of the increased amounts in beds 2 and 3 are possible: (1) penetration from the second CH_3I release, and (2) the lengthened flow duration from 1000 to 2500 min may have swept the activity farther downstream. It should be noted, however, that significant iodine release from the charcoal was not detected in the loop outlet samples.

The efficiency of the various loop components was measured at several times early in the run by sampling the gas between components. Table 2.5 gives the decontamination factors obtained in Run A-14. Similar data are given in Table 2.6 for Run A-15.

The diminishing DF with time results in part to difficulties in analysis of the very low concentrations downstream of the loop, although some reduction in DF would be expected as the inlet concentrations drop. No major differences are noticeable between Runs A-14 and A-15 with and without the heat exchanger and demister.

Pressure drop across the loop and components was measured and is shown in Figure 2.5 for Run A-15. A definite increase

TABLE 2.4. Iodine and Cesium Distribution in Loop Components

Component	wt% of Starting Material[a]			
	Cesium		Iodine[b]	
	A-14	A-15	A-14	A-15
Heat Exchange (condensate)	2.9		0.20	
Demister	70	-	2.4	-
Prefilter	0.02	1.5	0.11	0.02
HEPA filter	40	100	16	17
Char bed No. 1				
First 1/2 in.		-	31	30
Second 1/2 in.		-	14	12
Char bed No. 2				
First 1/2 in.		-	0.48	6.1
Second 1/2 in.		-	0.20	4.2
Char bed No. 3				
First 1/2 in.	-	-	0.60	4.2
Second 1/2 in.	-	-	0.30	3.0
Total	113	102	65	77
Calculated[c]	89	75	56	54

a. *Basis: Amount of material airborne in main room at time loop was started.*

b. *Includes methyl iodide.*

c. *Based on loop flow and observed* $t_{1/2}$ *at 30 min.*

was noted, primarily across the HEPA filter and the first charcoal bed. The pressure increase was not permanent. Upon return to normal atmospheric conditions following the run, pressure drops close to the original values were observed. Run A-14, because of changing flow, did not yield information about filter pressure change with time. DOP tests of the HEPA filters after each run showed no increase in penetration.

In summary, the two filter loop tests in steam-air environments cleaned the containment vessel main room gas space as

TABLE 2.5 Measured Loop Decontamination Factors, CSE Run A-14

Time, Minutes[d]	Decontamination Factor[a]											
	Cs	I	CH_3I	Cs	I	CH_3I	Cs	I	CH_3I	Cs	I	CH_3I
	35			60			90			200		
HEX and Demister	3.5	1.4		2.5	2.3		3	2.2		7	2.8	
Prefilter	1.7	1.6		1	1.1		1	1		1	1	
HEPA	6,800	1.7	1	8,700	1	1	2,500	1	1	4.7	1	1
First Charcoal Bed		>1,500	4.2		>100	2.9		>70	2		>30	2.6
Second Charcoal Bed		∿10	122		∿3	5		∿3	4		∿1	(c)
Third Charcoal Bed		(c)	(c)			5			4			(c)
Overall[b]	41,000	>55,000	420	22,000	>2,300	65	7,700	>176	32	33	>40	3.3

a. *DF = Conc. in/conc. out; efficiency = 1 - $\frac{1}{DF}$.*

b. *Includes all components. Best estimate of performance is given.*

c. *Indeterminant.*

d. *Loop flow started at t = 30 min.*

TABLE 2.6. Measured Loop Decontamination Factors, CSE Run A-15

Time, min[b]	Decontamination Factor[a]								
	Cs	I	CH_3I	Cs	I	CH_3I	Cs	I	CH_3I
	35			90			200		
Prefilter	1	1	(c)	(c)	1	(c)	(c)	(c)	(c)
HEPA	(c)	1.6	1	(c)	1.9	1	(c)	1.6	1
First Charcoal Bed	(c)	1,420	2.5	(c)	>60	1.7	(c)	(c)	1.4
Second Charcoal Bed	(c)	(c)	80	(c)	(c)	4.6	(c)	(c)	(c)
Third Charcoal Bed	(c)	(c)	10	(c)	(c)	4.1	(c)	(c)	(c)
Overall[d]	6000	>250,000	2,000	2,000	>1,000	34	10	>400	6.5

a. *DF = Conc. in/conc. out; efficiency = 1 - $\frac{1}{DF}$.*

b. *Loop flow started at 30 min.*

c. *Indeterminant.*

d. *Includes all components. Best estimate of performance is given.*

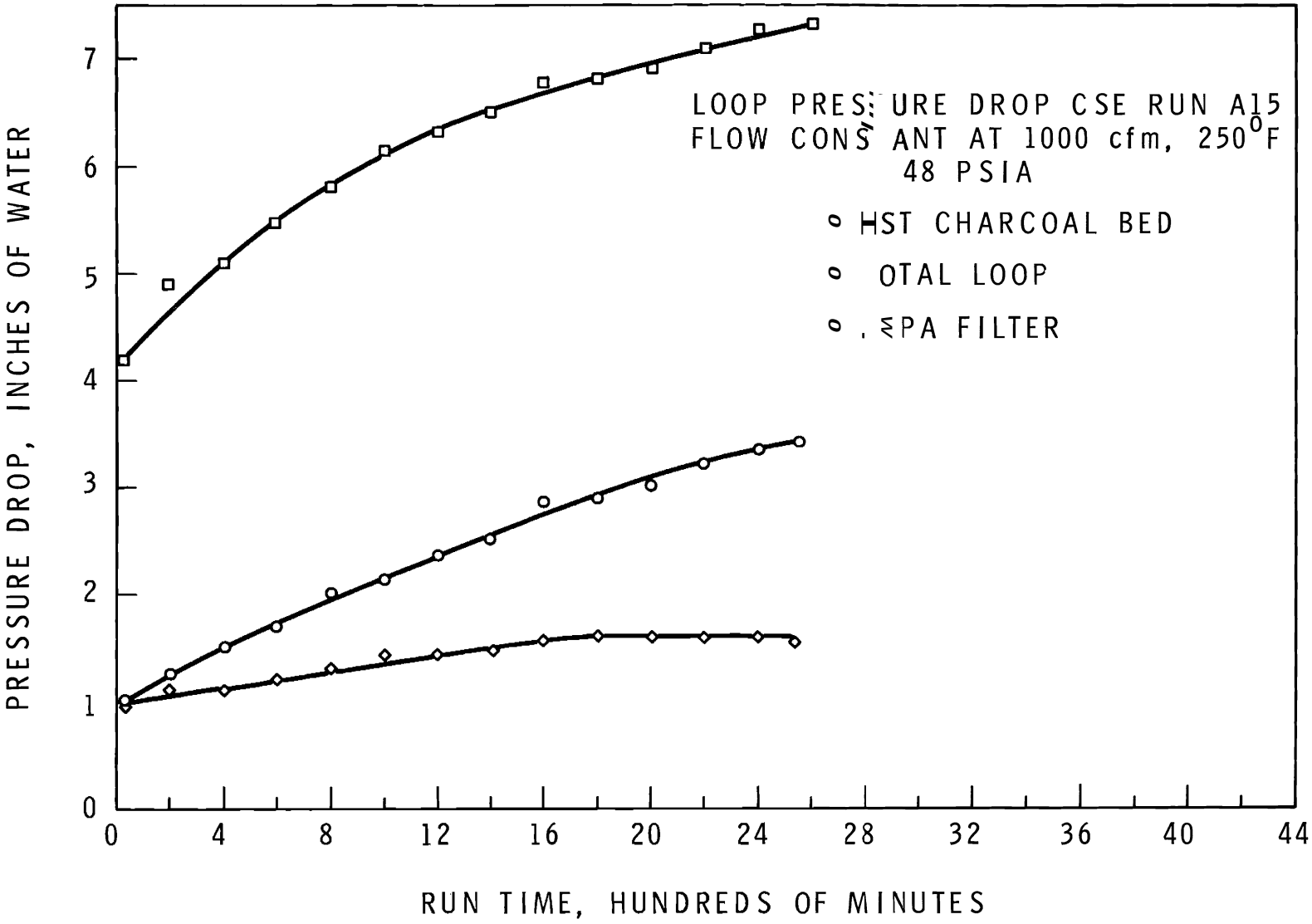

FIGURE 2.5. Loop Pressure Drop During Run A-15

predicted for particles and methyl iodide. Elemental iodine was removed faster than would be estimated from the loop flow and vessel volume. These removal rates persisted until the concentrations were less than 1% of initial value, after which the rate slowed. The impregnated charcoal effectively removed the methyl iodide by both exchange and adsorption from the steam-air atmosphere. Operation of the loop without the heat exchanger or demister did not reduce the loop effectiveness, although the pressure drop did increase with time.

Iodine Gas-Liquid Partition - L. F. Coleman

The equilibrium distribution of iodine between gas and liquid phases is a critical factor in determining both the kinetic and equilibrium behavior of iodine in water reactor systems. Any mechanistic predictive model of iodine behavior requires foreknowledge of the distribution coefficient, H, where H is defined as the ratio of concentration of total iodine in the liquid phase to that of the iodine species of interest in the gas phase at equilibrium.

$$H = \left(\frac{C_L}{C_G}\right)_{\text{equilibrium}} \qquad (1)$$

The true magnitude of H probably lies between two extreme values: (1) physical adsorption only, in accordance with Henry's Law, giving a temperature-dependent value in the range of 10 to 100 for elemental iodine, (note that this is the reciprocal of the usual way of expressing Henry's Law constant) and (2) sufficient chemical reaction so that the liquid acts as a perfect sink for iodine, equivalent to an infinite value for H. A theoretical study by Eggleton[2] suggests that the value of H can range from 10 to $>10^5$, depending on concentration, temperature and pH. The results of experiments in the CSE indicate that the value of H for inorganic

iodine is in the range 10^3 to 10^5 for conditions existing in reactor postaccident situations, and is not as sensitive to temperature, pH and iodine concentration as Eggleton's theoretical treatment would suggest.

Basic-borate solution, one of the containment spray solutions used in the CSE, is one of the spray solutions currently considered for use in power reactor containment spray systems. It is a solution of boric acid containing 1500 to 3000 ppm boron with sodium hydroxide added to give a pH of about 9.5. In five large-scale spray experiments in the CSE the gas phase iodine depletion rate at early times after spray initiation was essentially limited by gas phase diffusion.[3] This showed that H was large (>1000), but did not provide a quantitative measurement. Assuming that gas and liquid phases were in equilibrium after many hours and recirculation of the liquid through the spray nozzles, the value of H was about 10^4 for nonorganic iodine.

Two experiments were made in the 900 liter stainless steel SAT vessel to investigate the iodine partition behavior under accident conditions. Figure 2.6 shows the experimental arrangement. Isothermal conditions were maintained by steam-heated or water-cooled coils located in the 100-liter liquid pool. Liquid from the pool was circulated to a circumferential spray header at the top of the vessel which impinged the liquid against the wall at low velocity. Thus, the walls were covered with liquid of the same chemical composition as the pool and gas and liquid phases were at the same temperature. At the liquid volume used (100 liter), pool turnover time was once every 8 min. The steam to air ratios at a given temperature were approximately those expected for a vessel initially filled with air at room temperature and atmospheric pressure, to which steam is added to raise the

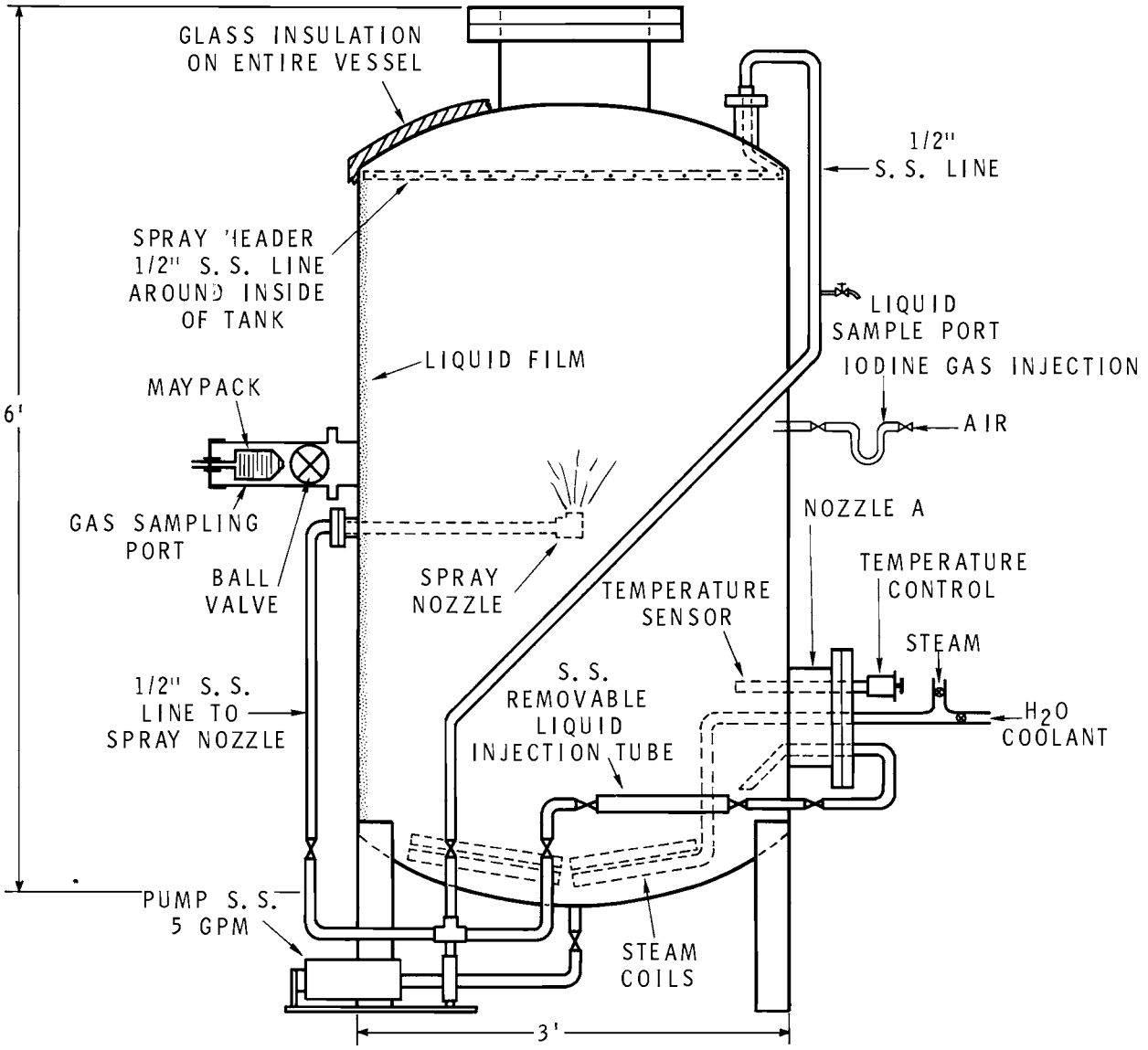

FIGURE 2.6. **Equipment Arrangements for Iodine Partition Experiments**

temperature and pressure to predetermined values. The large liquid to gas volume ratio was chosen to avoid depletion of iodine by sampling or equilibrium shifts and to ensure more uniform temperatures. Sampling of gas space was by insertion of CSE type Maypacks through an airlock. Liquid samples were taken from the external portion of the liquid recirculation line.

Iodine was introduced by different methods in each test. In Run E-1 elemental iodine, prepared by the iodide-dichromate oxidation technique, was volatilized directly into the gas space. In Run E-2 a concentrated iodine solution was injected directly into the liquid phase. Both tests used ^{131}I spike for analytical purposes. All other conditions were essentially the same in both tests, and are listed in Table 2.7. The conditions listed in Table 2.7 applied for the first 300 min. For the remainder of the experiment several variations were made (air purge and temperature cycling) to determine what mechanisms were of importance.

Figure 2.7 illustrates the results of the first exploratory test where iodine was released to the gas phase. Samples of the gas phase were collected with CSE type Maypacks.[4] The filters, screens, and charcoal-impregnated paper components were analyzed as a unit to give a measure of total inorganic forms of iodine while the charcoal bed gave a measure of methyl iodide concentration.

The first point of interest is the rapid initial removal of inorganic iodine (~1.2 min half-life). This agrees well with published data[5,6] and is related to elemental iodine removal. The slower removal rate observed after about 80 min of elapsed time appears related to a chemical reaction in the aqueous phase. The chemical nature of the iodine species involved and the reaction mechanism were not determined. Other

researchers[7] have suggested that hypoiodous acid, a hydrolysis product of elemental iodine, is the iodine form involved.

TABLE 2.7. Initial Test Conditions for Iodine Partition Experiments

	Run E-1	Run E-2
Temperature, °C	80 ± 1	80 ± 1
Pressure, psia	23.9	23.9
Gas volume, liter	800	800
Liquid volume, liter	100	100
Iodine mass release, mg	1.10	0.95
Maximum possible gas concentration, mg/liter	0.00137	0.00119
Iodine injection location	Gas	Liquid
Solution composition		
ppm B	3000	3000
pH	9.5	9.5
Iodine concentration in liquid		
Observed maximum, mg/liter	0.0110	0.0098
Observed minimum, mg/liter	0.0103	0.0095
Observed average, mg/liter	0.0109	0.0095

After 300 min., the gas phase was purged with air until about 4.3 vessel volumes of gas were expelled to see if the system would re-equilibrate to prepurge levels. During the purge the methyl iodide gas phase concentration decreased by a factor of 0.01, while the inorganic fraction decreased only by a factor of about 0.1 and then continued decomposition at the previous rate. Methyl iodide behavior was in agreement with ideal gas behavior, continuous gas-liquid equilibria, without further production or depletion of this species by chemical equilibrium shifts or reactions. A methyl iodide

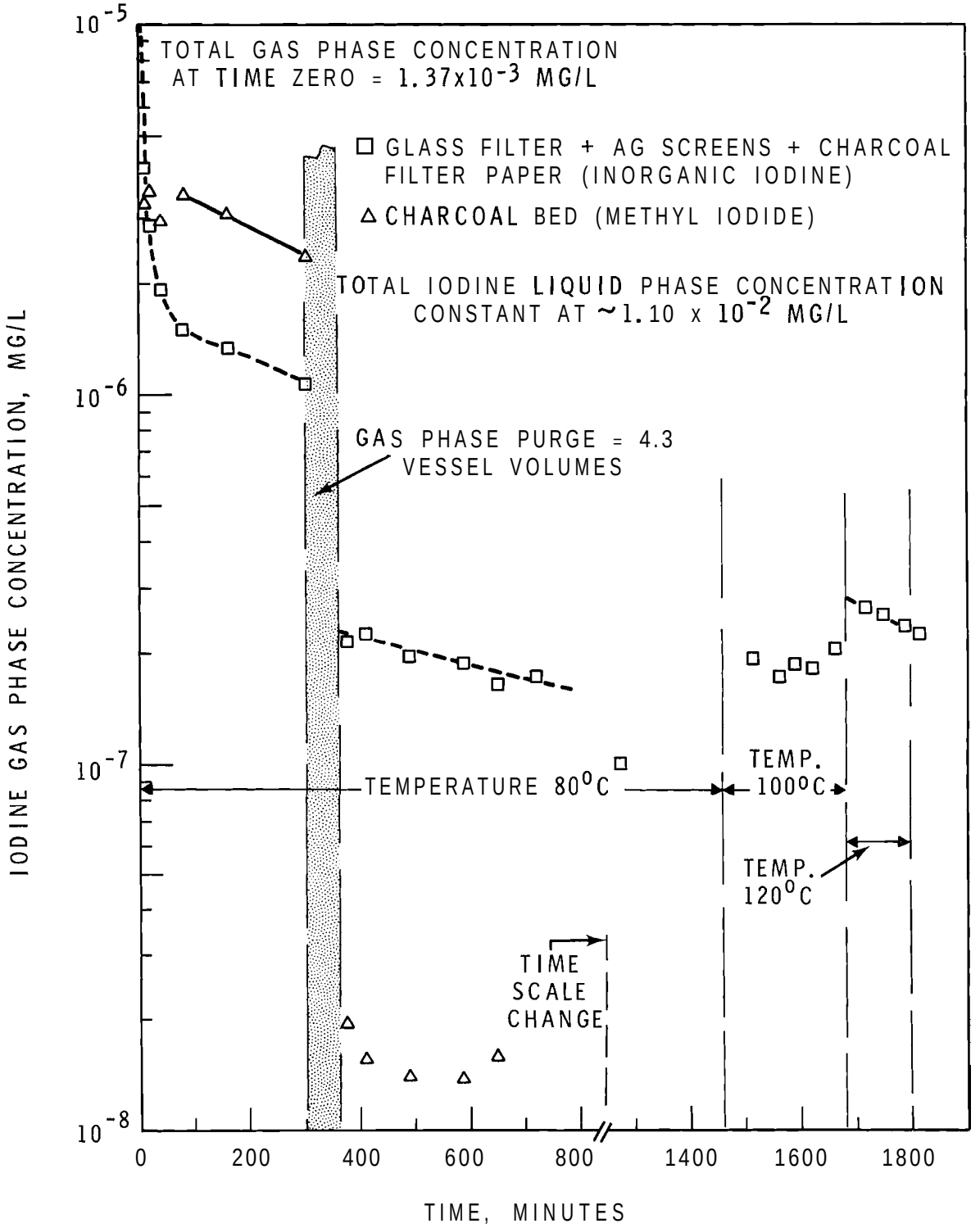

FIGURE 2.7. Iodine Partition Experiment E-1, Gas Phase Release

partition coefficient of 1.5 was used in this calculation. If the same criteria are applied to the inorganic iodine fraction, a partition coefficient for physical absorption

$$\frac{\text{Concentrated species i in solution}}{\text{Concentrated species i in gas phase}}$$

of about 30 is obtained for the nonelemental species. Using this value for the physical partition coefficient would show 0.5% of injected iodine to be in this form or converted to this form after contact with the aqueous phase.

Increasing the temperature to 100 and 120 °C caused a slight increase in iodine gas phase concentration. However, at 120 °C the decomposition rate was accelerated. Methyl iodide concentrations showed a slight increase with temperature but were at near background levels and the concentration values became very imprecise.

The concentration of iodine in the liquid phase remained essentially constant throughout the experiment, but Figure 2.7 shows that the concentration in the gas phase decreased with time. Although a true equilibrium was not attained during the experiment, a partition coefficient can be calculated for the quasi-equilibrium state by dividing the liquid concentration by the gas concentration extrapolated back to zero time. A value for H of 6400 is obtained for inorganic iodine at 80 °C by this method.

Gas phase behavior data for experiment E-2 are illustrated in Figure 2.8. Iodine was introduced directly to the aqueous phase. The general behavior was similar, but several differences were observed. Methyl iodide concentration was less than 0.1% of the initial airborne iodine fraction and was at background count rate levels throughout the test and is not

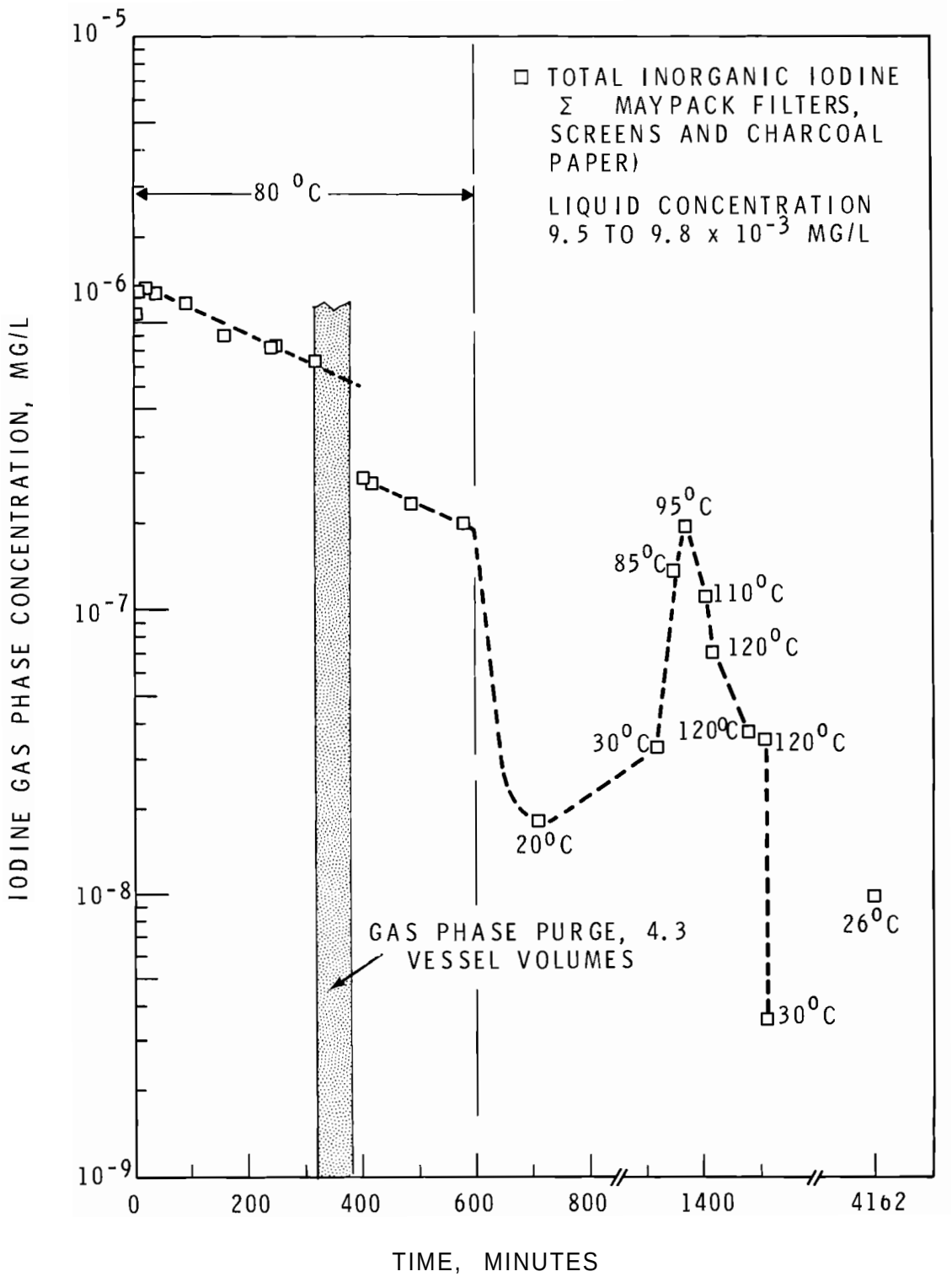

FIGURE 2.8. Iodine Partition Experiment E–2, Solution Phase Release

illustrated in Figure 2.8. Also, the inorganic decomposition rate was slightly more rapid in experiment E-2 and the concentration reduction during the purge period was less.

After the purge, the gas concentration of inorganic iodine continued to decrease at its prepurge rate. When the temperature was lowered from 80 to 20 °C the gas concentration decreased, as expected. Upon reheating, the gas phase concentration returned to its previous level. At 120 °C, the decomposition rate again accelerated. The equilibrium partition coefficient for inorganic iodine in Run E-2, calculated by extrapolation to zero time was 6800, in good agreement with the value of 6400 obtained in Run E-1.

Some tentative conclusions from these two experiments can be made. The similar results obtained by injecting iodine into gas and into liquid phases showed that transfer mechanisms of volatile forms were reversible. The overall partition coefficient for inorganic forms at 80 °C was about 6500 at zero time. The physical partition coefficient of an unknown inorganic species (perhaps HOI) was about 30 at 80 °C. Finally, a slow liquid phase chemical reaction occurred which depleted the volatile species with a half-time of about 400 min at 80 °C, causing H to increase with time. These conclusions apply for the pH 9.5 base-borate solution and are not considered to be general for all systems.

Coolant Blowdown Studies - R. T. Allemann, W. C. Townsend, and A. S. Neuls

A reactor simulator vessel with a volume of 150 ft^3 and designed for operation at 600 °F and 2750 psig is being used in experiments to study loss-of-coolant accidents. The objectives of the experiments include testing the validity of mathematical models used for predicting the consequences of a loss-of-coolant reactor accident. The vessel is mounted in a steel framework with the discharge nozzle directed horizontally.

The blowdown apparatus is instrumented to measure internal pressures, temperatures, liquid level, void fraction of the fluid in the exit duct, mass of fluid remaining in the vessel, thrust reaction forces, shell stress, and forces on reactor dummy core structures (Figure 2.9).

During this reporting period six blowdown experiments were made with the fluid discharged from the middle blowdown nozzle B (Figure 2.9). Simulator reactor internal structures were not installed in the vessel for this series of experiments. The purpose of this experimental series was to

- Measure the void fraction of fluid in the discharge pipe,
- Determine bubble size and bubble velocity variations with nozzle break size and initial fluid conditions,
- Measure the liquid level swell behavior, and correlate these data with bubble rise computer codes.

Initial conditions for these runs are given in Table 2.8. Not all data have been reduced for these runs as yet. The discussions following are preliminary results and subject to revision following complete data analysis.

TABLE 2.8. Blowdown Run Conditions

Run No.	Nozzle and Break Diameter	Pressure, psia		Temperature, °F	Nom. Vessel, vol% Full
		Initial	Saturation		
B-80	B/8	1000	681	500	100
B-81	B/8	↓	1000	545	60
B-82	B/6	↓	1000	545	60
B-83	B/6	↓	681	500	100
B-84	B/4	↓	681	500	100
B-85	B/2	↓	681	500	100

The results show that calculations of the water remaining after blowdown may be nonconservative, and that using saturation pressure as an orifice boundary condition during subcooled decompression is not adequate at small values of subcooling. The

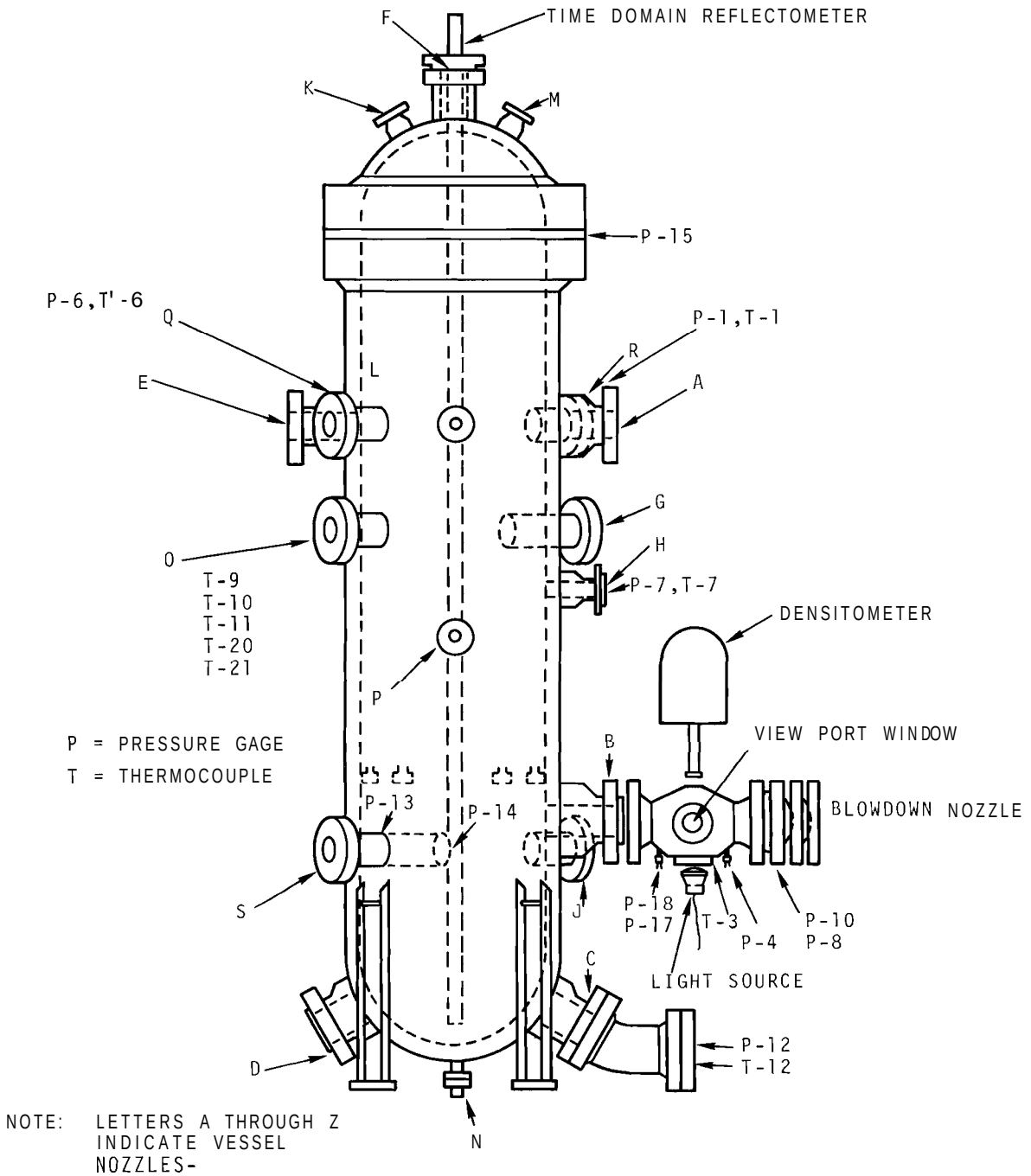

FIGURE 2.9. **CSE Blowdown Test Vessel**

high speed motion pictures of exit fluid that were taken have given preliminary information on the nature of the fluid leaving the vessel during blowdown.

Residual Water Remaining After Blowdown - W. C. Townsend

Using data from earlier blowdowns as well as those of Table 2.8, the weight of water remaining after a blowdown is completed has been compiled for a group of top and middle nozzle blowdowns. These observed data were based on liquid level data and the fluid density at measured fluid conditions.

These observations are compared with predictions from the FLASH2 code in Figure 2.10. Acceptability of FLASH2[11] predictions were based on agreement with measured pressures and liquid level during the blowdown. In all cases the FLASH2 residual mass predictions are nonconservative. Percentage error figures are shown alongside the predicted points. The difference between measured and predicted residual water for the top nozzle experiment varied between 9.6% and 46.8%, whereas for the middle nozzle the difference varied between 28% and 194%. The percentage difference between predicted and measured residual water is larger for the middle nozzle, than for the top nozzle blowdowns. Furthermore, an apparent dependence of the error on break size is evident in Figure 2.10.

The effect of the sieve plate in the vessel in residual mass is shown in Figure 2.11 for middle nozzle blowdowns. FLASH2 predicts a larger residual mass for the runs made without the sieve plate. Predicted mass error is noted to be significant and increases with break size. Furthermore, the experimental data indicate that the break area affect is more significant for the runs with the sieve plate.

FLASH2 predictions are all too high or nonconservative. These predictions were made with a discharge coefficient chosen to provide agreement between vessel pressure and mass velocity during the blowdown. The observed discharge rate is 50 to 80%

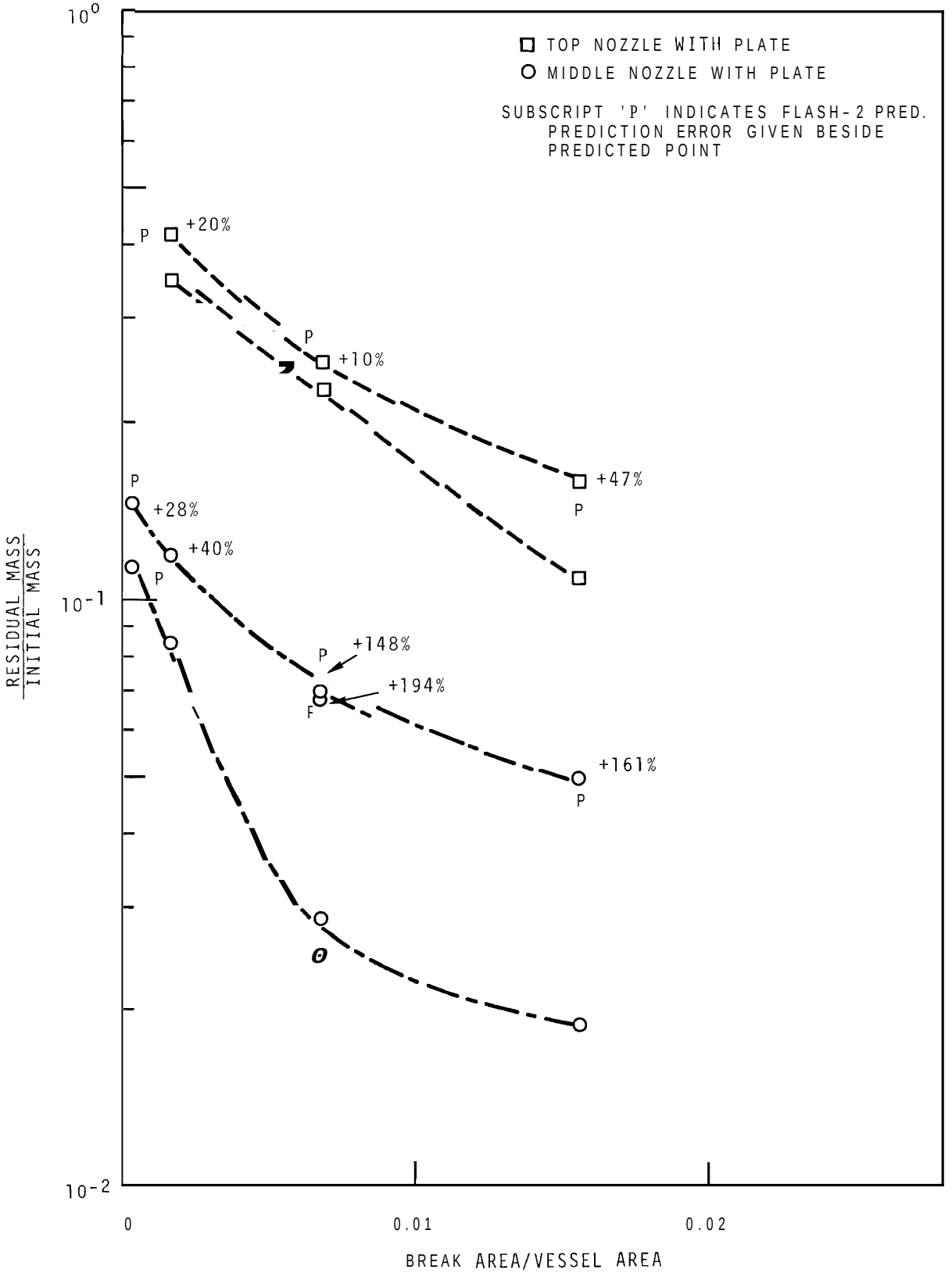

FIGURE 2.10. **Residual Water in Vessel After** Blowdown

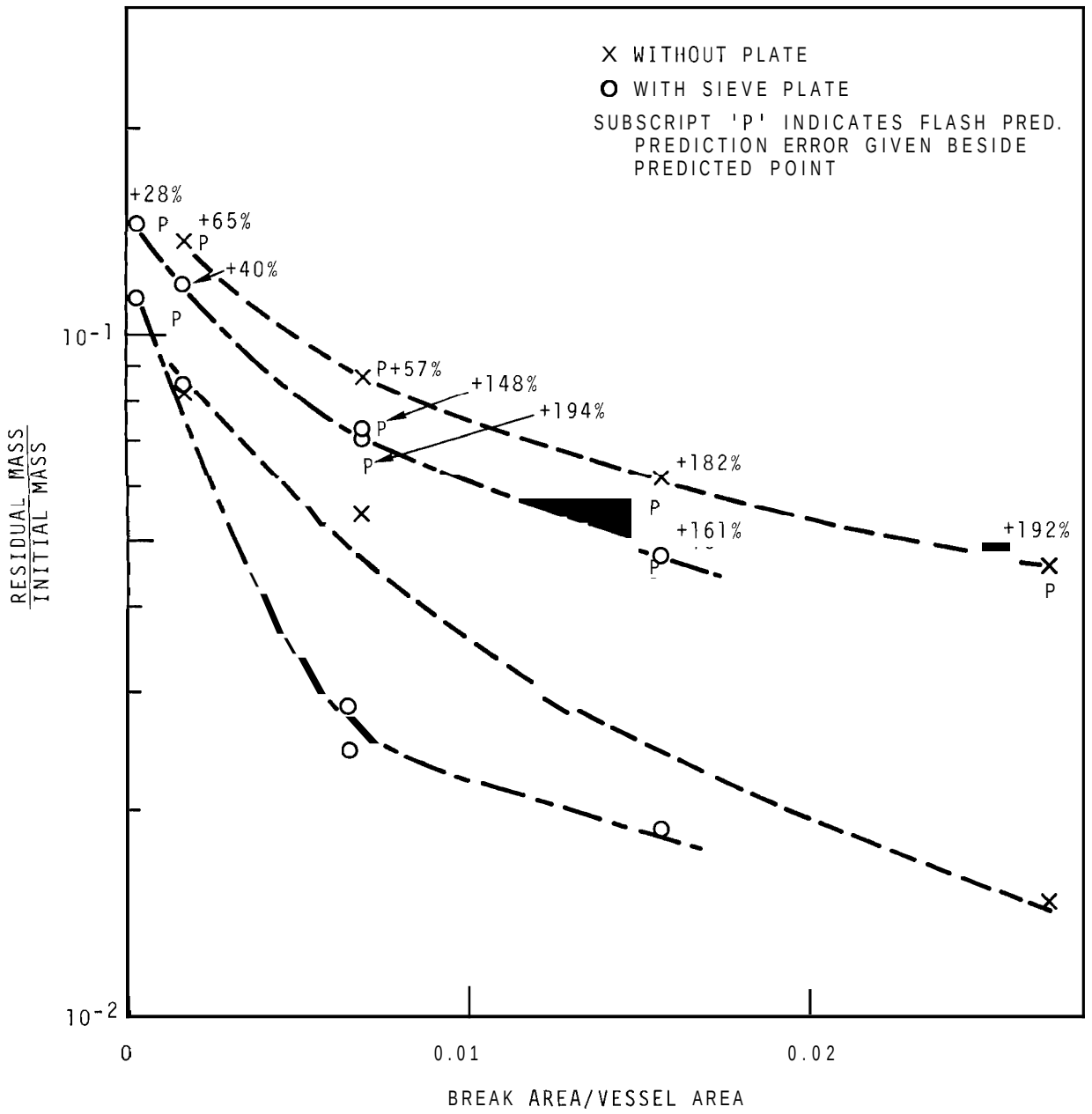

FIGURE 2.11. Residual Water in Vessel After Blowdown - Middle Nozzle

of that in the Moody[8] flow model. The Moody discharge rate would provide somewhat better agreement on residual mass predictions.

The differences between prediction and experiment results (Figures 2.10 and 2.11) may be caused by the entrained fluid discharged from the vessel during blowdown. Entrainment is not considered in FLASH2; however, with the fluid velocities (choked exit flow) at transition and the violent fluid motion even immediately after transition entrainment is believed to be significant. Residual pool vaporization has been considered and does not account for the difference because sufficient heat is not transferred from the wetted region of the vessel to the fluid. Detailed radiant heat transfer calculations have not been made because of the relatively low differential temperature and hence, the low radiant energy transfer.

CSE and other[9] experimental data of residual water following blowdown were compared in Figure 2.12. CSE data were reduced to the same nondimensional basis for comparison. Agreement in the low area ratio range is good; however, the CSE data, with a large vessel area, do not reach the "knee" shown in Figure 2.12. The residual mass data from the CSE top nozzle blowdown with core-plate experiments can be summarized in the equation

$$\ln R_M = -0.91364 - 83.5723\, R_A$$

where

$$R_M = \frac{\text{Mass Liquid Remaining}}{\text{Initial Mass}}$$

$$R_A = \frac{\text{Break Area}}{\text{Vessel Area}}.$$

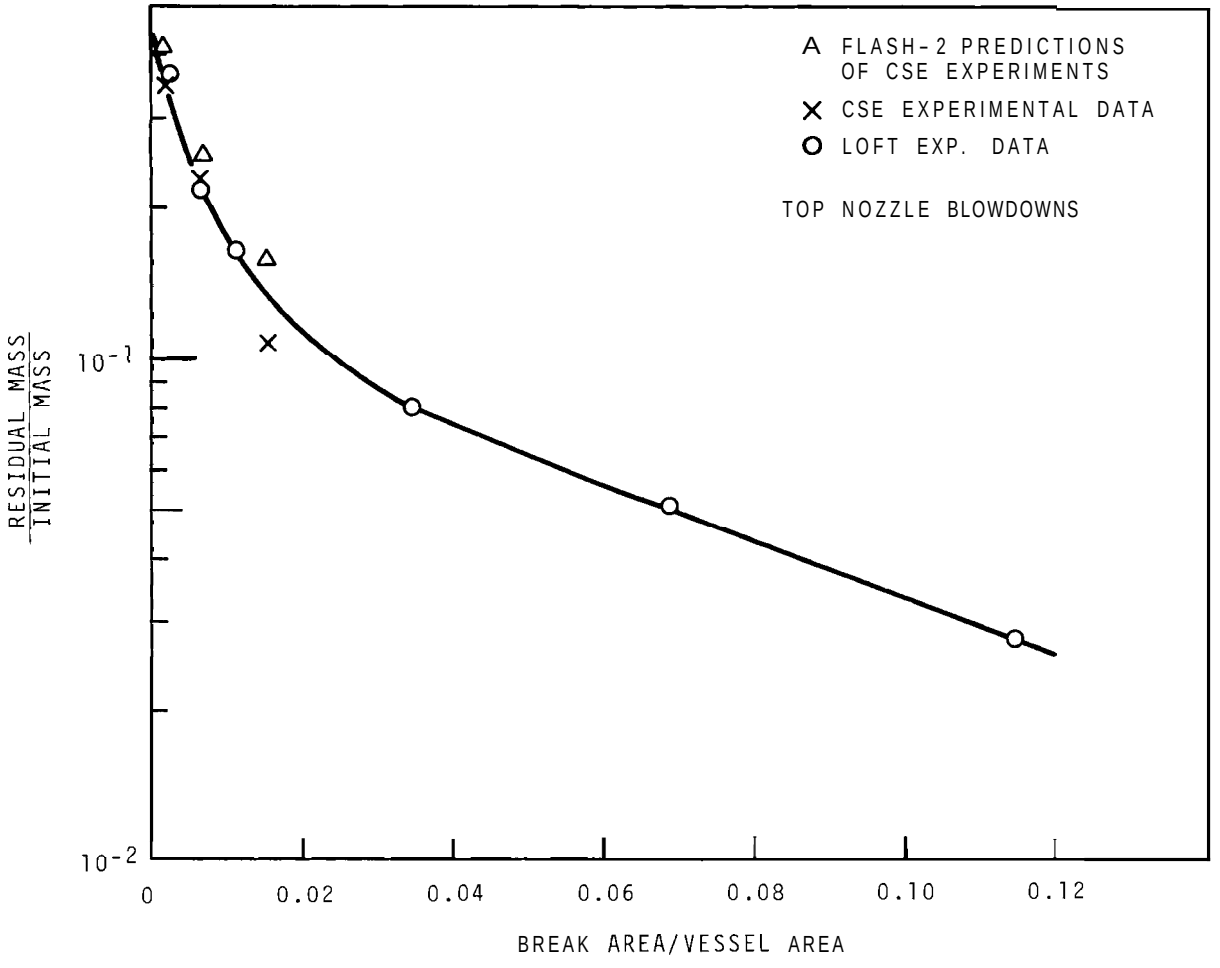

FIGURE 2.12. **Residual Water in Vessel After Blowdown - Top Nozzle**

High-Speed Motion Pictures of Fluid in the Test Section - R. T. Allemann

The Test B-85 was made from subcooled initial conditions shown in Table 2.8. In addition to the normal pressure and temperature sensors, this run included a special outlet test section consisting of a nominal 8-in. pipe with glass windows capable of withstanding the initial pressure and temperature (Figure 2.8). High speed (2000 to 8800 frames/sec) motion pictures were taken of the fluid in the test section by lighting at 90° (from view) a narrow, flat channel (2 × 2 × 1/4 in.) on which the camera was focussed. A stainless shim stock "flag" with fiducial marks was placed in the pipe in the light beam and was used to show when blowdown began by its movement out of the pipe and to give a calibration of the film for measuring the bubble diameter. The system was moderately successful in that bubble size and velocity could be measured. Not very many bubbles were to be seen.

Based on the viewed and illuminated volume and the bubbles seen on each frame, the number of bubbles per unit volume was calculated and results are shown in Figure 2.13.

The pressure and saturation pressure (obtained from the temperature) in the test section are also shown during this period of high-speed motion picture, lasting about 2 sec. Although pressure errors of ±10 psi may be present there appears to be a correlation between the bubbles seen and the super saturation value. The bubbles appeared in two groups; the first corresponding to an underpressure of 20 psi. The second group showed more bubbles and appears to be continuing as the film ended.

The bubble diameter was in the range 1/32 to 1/16 ± 1/64 in., well into the skin cooling controlled region of bubble growth (growth limited by heat transfer). The velocity along the flow

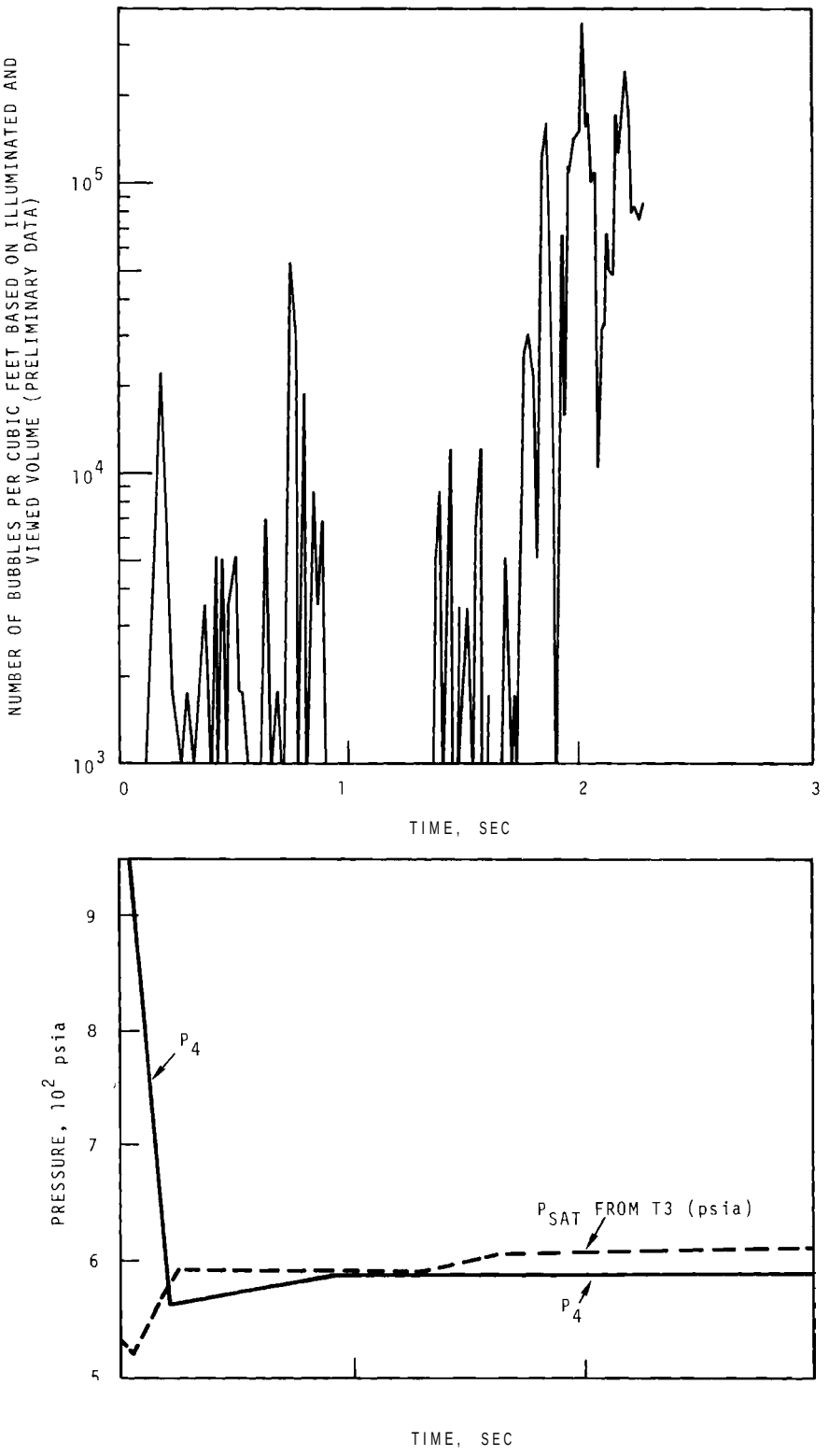

FIGURE 2.13. **Motion Picture and Pressure History in Outlet Test Section**

direction obtained from five bubbles which stayed in the illuminated region for 10 frames or more ranged from 6.8 to 8.6 ft/sec (8.0 ft/sec average). Calculations made with the bubble information gave a bubble rise velocity of 0.6 to 0.75 ft/sec in a 1 g potential field. This rise velocity is slower than ordinarily used in such codes as FLASH2. Possibly the bubble sampling was poor because of the small volume observed and because the low flow rate induces few bubbles into the outlet stream. Further tests with larger illuminated fields may show if there are larger bubbles with high velocities. The mass flow rate obtained from the bubble velocity was 85 to 105 lb/sec which corresponds to the data of the liquid level probe of 91 lb_m/sec (assuming few bubbles), and the weight load cell data of ∿89 lb_m/sec. The mass flow rate predicted by the Moody[8] model at these conditions is also about 97 lb_m/sec so that the flow coefficient as applied to Moody's flow rate based on most observed bubble velocities would be greater than one. At least one bubble velocity measured came within the range of the other data. A possible cause of the high bubble velocity is the presence of a velocity profile in the test section, being highest in the center where the camera views. The profile could be the result of wall friction or the velocity potential field caused by the contraction of flow area from the test section to the orifice. The best correlation of FLASH2, which uses the Moody flow rates, is given when an overall coefficient of 0.80 is used for the run conditions of B-85. The quality obtained for 10^5 bubbles per ft^3 is 7×10^{-3} for 1/16 in. bubbles and 7.6×10^{-4} for 1/32 in. bubbles. This compares with 2 to 8×10^{-3} obtained nearby with the neutron densitometer void fraction detector.

The motion picture data so far have raised more questions than they have solved. The existence of bubbles in the exit pipe has been shown but the small size observed does not lend

itself to the separation theories currently in use. Another question which appears is that of the slow recovery to saturation of the pressure. The time delay appears to be on the order of 0.3 to 1 sec.

Acoustic Pressure Oscillations During a BWR-Type Blowdown - A. S. Neuls

A current study shows that the WHAM subcooled decompression code[10] can be applied to a BWR-type system with reasonable accuracy. Improvements of the exit nozzle depressurization treatment should improve the code's capability to predict acoustic behavior in a saturated system.

The WHAM code was applied to CSE Run B-27B.[11] This run was a 3.44-in. diameter, BWR-type, middle-nozzle blowdown. The initial pressure and temperature were 1010 psia and 552 °F. This corresponds to approximately 12 to 160 psi overpressure in vessel and nozzle extension respectively. The WHAM code was applied to the run to investigate the code's capability to predict acoustic pressure oscillations during the blowdown of a partially full vessel, initially at or near saturated conditions.

Important features to be considered in the application included the steam dome, the outlet nozzle back pressure, the break opening time, and the sonic velocity. The steam dome was modelled by utilizing the pressurizer option in WHAM. The pressurizer node was held at constant pressure for this study but the code could be modified to allow for some prescribed pressure history. The exit orifice back pressure was assumed to be atmospheric. Recent applications of WHAM to LOFT semi-scale data use a back pressure equal to the saturation pressure.[12] However, this back pressure would leave little or no driving force to create the observed rarefaction waves. A

linear break-area opening was used, fully opened at 0.56 msec. The time of 0.56 msec was determined for a previous 3.44-in. blowdown.[13] No attempt was made to use an arbitrary back pressure or break opening function to model the shape of the initial rarefaction wave in the exit pipe.[14] The initial fluid temperature was determined from an average of the initial values of the numerous thermocouples in the vessel. There was no noticeable temperature gradient. The sonic velocity at the initial temperature was determined from Reference (17). The full sonic velocity was used, not 90% of the value as suggested by other users.[15]

The vessel approximation for the WHAM calculations was detailed and included 27 "legs" with a total of 850 nodes. The approximation was, however, a one-dimensional model of a three-dimensional system. Care was taken to use actual areas and minimum wave transport distances since area changes and wave transport times are important in the WHAM calculations. There is no need to conserve volumes at the expense of proper areas as has been suggested at LOFT.[16]

Figure 2.14 shows a comparison of the pressure history at the instrument ring (in the steam dome) and the constant pressure used in WHAM. The small 15 psi drop in pressure would not have much effect on the calculated pressure oscillation in the liquid phase.

Figure 2.15 shows the measured and calculated pressure in the exit orifice. The magnitude of the initial decompression wave predicted by WHAM is very close to that of the measured wave as indicated by the drop in pressure following rupture. However, the shape of the wave is quite different from the measured wave. The shape of the initial decompression wave suggest the possibility of a nonlinear break opening. The measured wave is complicated by pressure oscillations that

start about 4 msec before the large decompression wave that indicates rupture. The oscillation preceding rupture seems to be characteristic of the double-disc over-pressurization rupture technique used at CSE and LOFT. Considering the assumptions used to calculate the initial decompression wave, the agreement between the measured and calculated pressure at the orifice suggests that the use of a back pressure well below the saturation pressure is a useful technique for using the WHAM code.

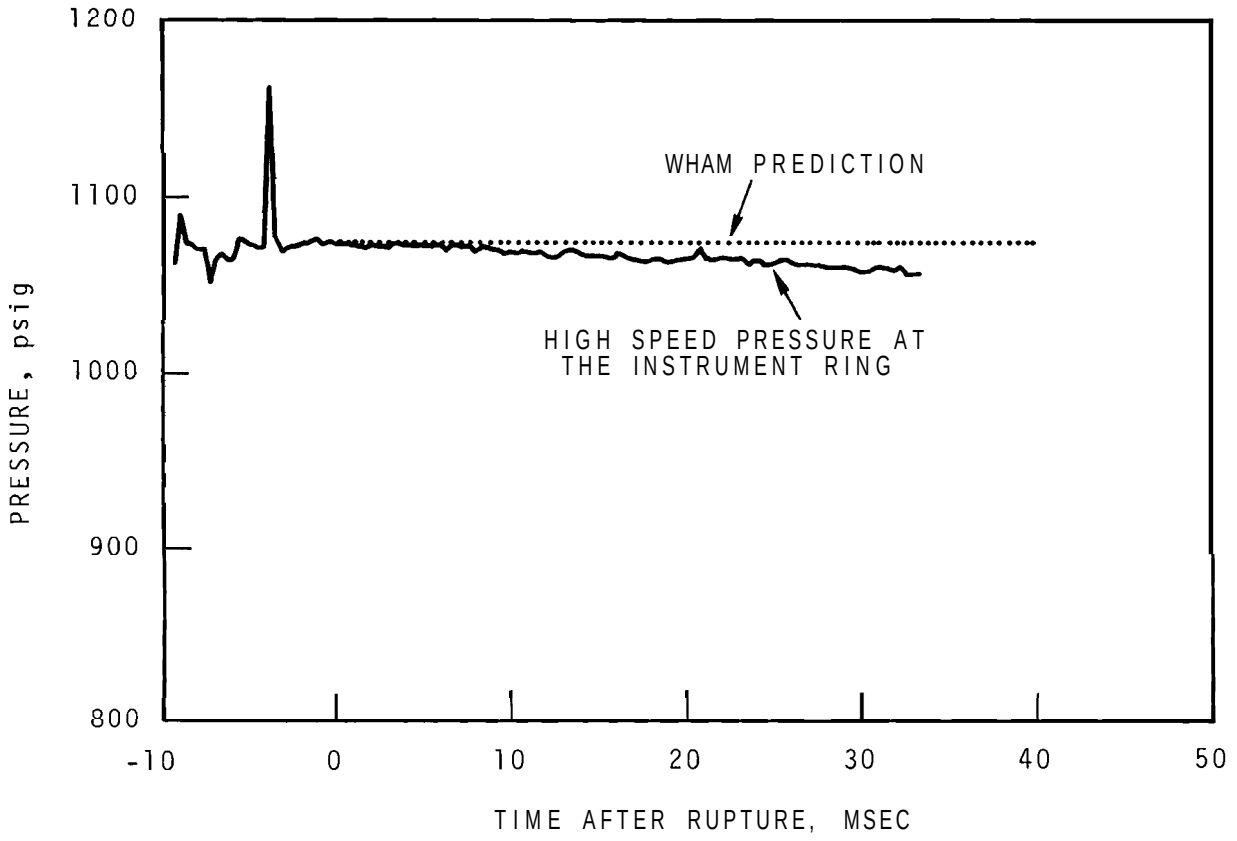

FIGURE 2.14. **Comparison of Experimental and Assumed Pressure in the Steam Dome**

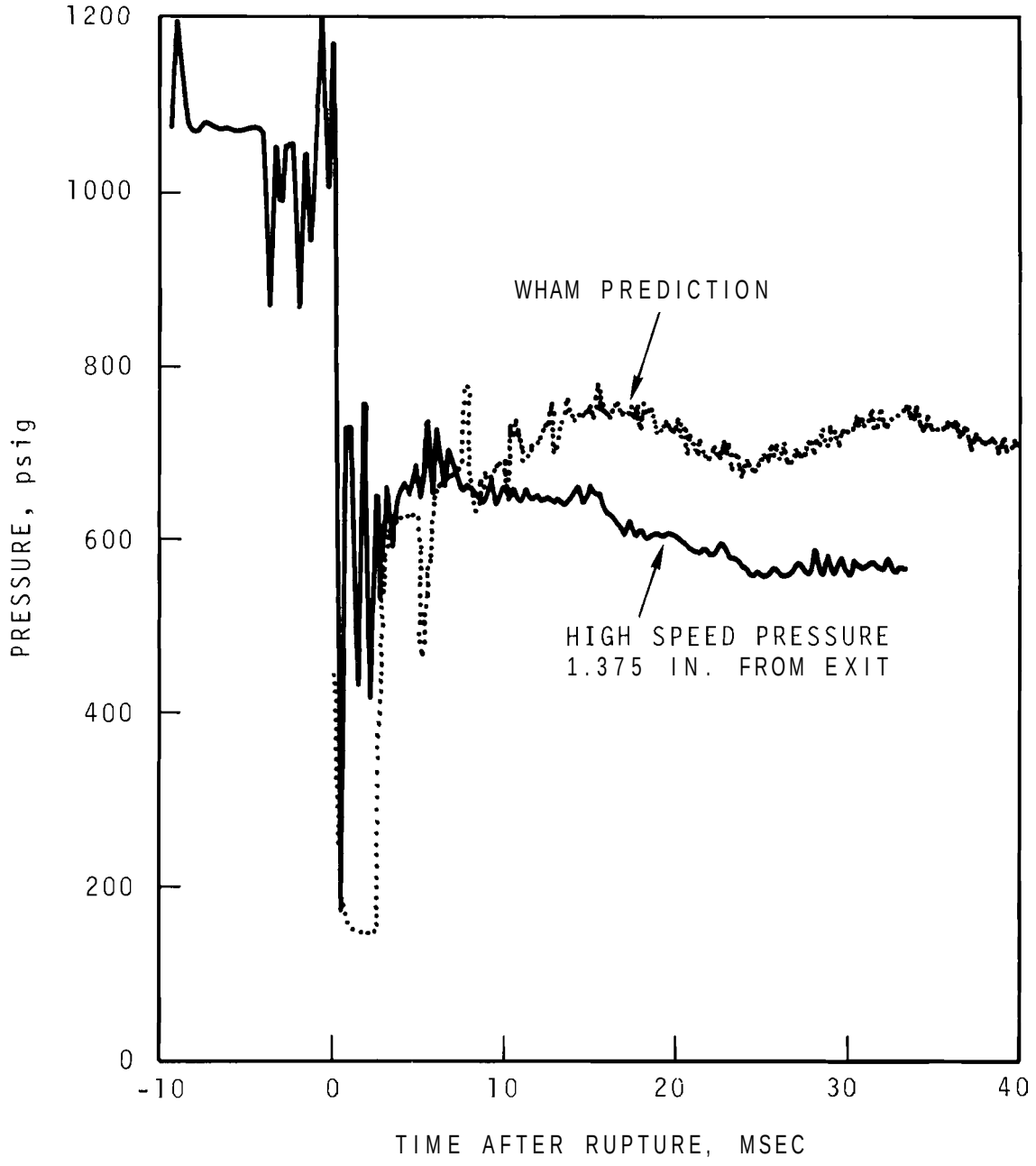

FIGURE 2.15. **Comparison of Experimental and WHAM-Calculated Pressure in the Orifice**

Figure 2.16 is a comparison of the measured and calculated pressure in the vessel just below the plate. Although the magnitude of the calculated major pressure oscillations are too

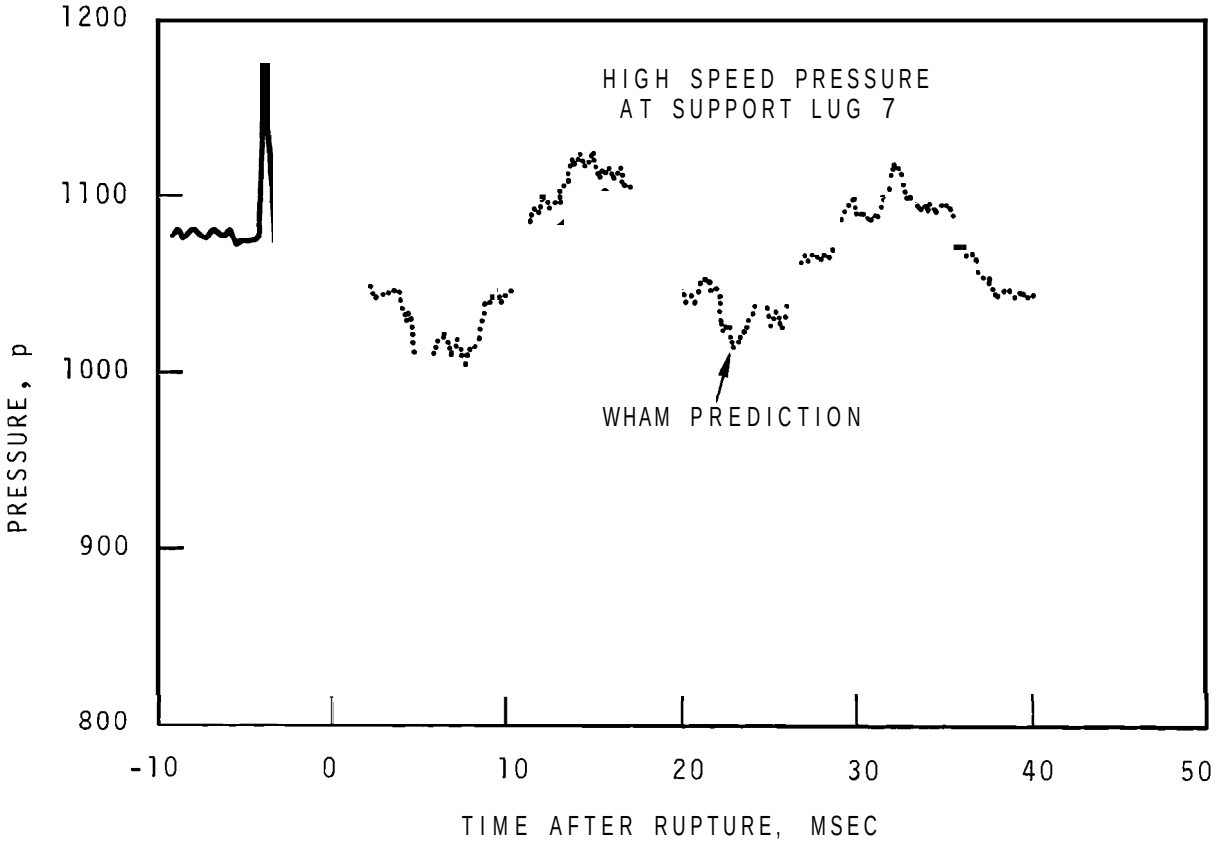

FIGURE 2.16. Comparison of Experimental and WHAM-Calculated Pressure in the Vessel at Support Lug 7

large, the frequency is very close, indicating the use of the pressurizer option in WHAM was justified. The agreement of the pressures is within 40 psi during the measuring time. However, because the magnitude of the measured oscillation is only about 70 psi, and the error is a large percentage of the oscillation, it is doubtful that the present study has sufficient accuracy to predict the pressure drop across the thin sieve plate in the CSE vessel.

The back pressure history at the exit used as an input to WHAM depressurization code should, as a general rule, not be the saturation pressure because this treatment does not give correct results at low subcooling. Atmospheric pressure gives reasonable results, probably because of a delayed time of the flashing at the exit.

References

1. Nuclear Safety Quarterly Report, July, August, September, 1969, BNWL-1266. Battelle-Northwest, Richland, Washington, December 1969.

2. A. E. J. Eggleton. A Theoretical Examination of Iodine-Water Partition Coefficients, AERE-R-4887. Atomic Energy Research Establishment, Harwell, Berkshire, February 1967.

3. Nuclear Safety Quarterly Report, November, December, 1968, January 1969, BNWL-1009. Battelle-Northwest, Richland, Washington, p. 2.20. March 1969.

4. J. D. McCormack. Maypack Behavior in the Containment Systems Experiment-A Penetrating Analysis, BNWL-1145. Battelle-Northwest, Richland, Washington. August 1969.

5. R. K. Hilliard, L. F. Coleman, and J. D. McCormack. Comparisons of the Containment Behavior of a Simulant with Fission Products Released from Irradiated UO_2, BNWL-581. Battelle-Northwest, Richland, Washington, March 1968.

6. J. G. Knudsen and R. K. Hilliard. Fission Product Transport by Natural Processes in Containment Vessels, BNWL-943. Battelle-Northwest, Richland, Washington. January 1969.

7. F. O. Cartan et al. Evidence for the Existence of Hypoiodus Acid as a Volatile Iodine Species Produced in Water-Air Mixtures, Proceedings of the 10th AEC Air Cleaning Conference, New York, N. Y., August 28, 1968. CONF-680821, pp. 342-353. 1968.

8. F. J. Moody. Maximum Two-Phase Vessel Blowdown from Pipes, APED-4827. Atomic Power Equipment Department, General Electric Company, San Jose, California.

9. LOFT Quarterly, IDO-17213. Idaho Operations Office, Idaho Falls, Idaho.

10. S. Fabic. Computer Program WHAM, Kaiser Engineers Report No. 67-49-R, November 2967, Argonne Code Center, Abstract 278.

11. Nuclear Safety Quarterly Report, May, June, July, 1969, BNWL-1187. Battelle-Northwest, Richland, Washington, September 1969.

12. *Quarterly Technical Report, LOFT Program Office, July 1 to September 30, 1968, IDO-17266. Phillips Petroleum Company, Idaho Falls, Idaho, February 1969. p. 18.*

13. *Nuclear Safety Quarterly Report, February, March, April, 1968, BNWL-885. Battelle-Northwest, Richland, Washington, October 1968.*

14. *Quarterly Technical Report, Step Project, January through March 1966, IDO-17186, Phillips Petroleum Company, Idaho Falls, Idaho, November 1966. p. 38.*

15. *Quarterly Technical Report, LOFT Program Office, October 1 - December 31, 1968, IDO-17267, Phillips Petroleum Company, Idaho Falls, Idaho, July 1969, p. 27.*

16. *G. H. Hanson. Subcooled-Blowdown LOFT—Quarter-Scale Experimental Pressures and Calculated Transients Using the WHAM-Code. Presented June 18, 1969 at ANS meeting, Seattle, Washington.*

17. *Handbook of Chemistry and Physics, 46th edition. CNC, Cleveland, Ohio, 1965, p. E-29.*

3. PRESSURE BEARING COMPONENT EVALUATION AND MONITORING STUDIES

CRACK DETECTION IN PRESSURE PIPING BY ACOUSTIC EMISSION -

P. H. Hutton and J. B. Vetrano

Introduction

A program to develop application of the "acoustic emission" phenomenon to detect flaw growth in reactor pressure piping and vessels has been sponsored at Battelle-Northwest since February, 1966 by the USAEC's Division of Reactor Development and Technology. The purpose of the program is to strengthen the safety of nuclear facilities further.

The term "acoustic emission" is defined as elastic waves produced in solids by energy released during deformation and fracture.

A related program concerned with the in-plant application phase is also sponsored by DRDT at the Idaho Test Site, Idaho Falls.

This program is also pertinent to the integrity surveillance portion of the LMFBR program, however, it has not yet included consideration of the special problems of high temperature and radiation which must be overcome for adaptation to LMFBR.

Activity on this program has been curtailed during the last quarter to accommodate a realignment of program scope by the sponsor.

Discussion

Task 1-Signal Analysis and Characterization

Propagation characteristics of both crystal generated signals and real acoustic emission signals in steel pipe of various sizes and wall thicknesses has been investigated.

The purpose is to improve understanding of signal propagation in various pertinent material geometries and thus provide for a judicious approach to signal detection under any given circumstance.

Pipes used - all mild steel - were 3 3/4 in. OD × 1 in. wall thickness × 182 in. long, 4 1/4 in. × 1 in. × 240 in., 6 in. x 1 in. × 144 in., 4 1/2 in. × 1/4 in. × 252 in., and 8 1/2 in. × 1/4 in. × 120 in.

Comparison of signals received by the standard 0.080 in. diameter transducer and a wedge mounted shear crystal were studied as a function of distance between signal source and sensor transducer. The effect of circumferential location of source with respect to sensor on signal propagation time was also investigated. Surface wave dampening putty was used for most experiments. Detection system frequency was set at 600 kHz to about 1 MHz.

Effects of Pipe Diameter

A pipe is a more complete wave guide or trap for acoustic signals than is a plate. In a large plate, some of the spherical stress waves radiating from a point source will be captured between the plate surface boundaries and thus be guided along the plane of the plate in a direction of interest. The balance of the original waves escape in lateral directions where no reflector turns them back to the direction of interest. In a pipe, however, the energy radiating in lateral directions is forced to travel circumferential and helical paths down the pipe. Thus, in a typical pipe, more of the original energy ultimately arrives at a detector position down the pipe than would be the case in a large plate - which is effectively unbounded in the lateral directions. The effect is such that pipes with a small ratio of OD to wall thickness approach solid cylinders in their acoustic behavior, whereas pipes with a large ratio of OD to wall thickness approach plates in their

acoustic behavior. In many cases - where the sensor transducer is sufficiently distant from the source and particularly where a small diameter pipe is being used - the higher velocity components may travel one or more helical routes around the pipe arriving at a sensor before the earliest arriving shear components. The angle of arrival of these helical route components would be such as to excite vibration in a shear crystal. Thus it is expected that the arrival of shear components would not be as sharply defined in a pipe as in a plate - particularly when a wedge-mounted shear crystal is used as the detector. The experiments under discussion here were not intended to test this theory. The described effect may be of some significance as shear signals in pipes were often found to not be defined sharply by either type of transducer. For example, in Figure 3.1, it is seen - for the 4 1/4 in. × 1 in. × 240 in. pipe - that the time position of shear signal arrival is not ideally defined by either the 0.080 in. transducer or the wedge transducer.

This photo also illustrates the negligible effect of differing angular relationships between source and sensor. In general, the most significant effect pipe diameter plays in the transient characterization of a received signal is to introduce an additional source location error in the axial direction - caused by the unknown amount of circumferential travel. Error becomes less with increasing distance in axial direction and also with decreasing pipe diameter. For the general case, where a transient signal is being investigated and it is wished to consider either the shear wave component or the earliest arriving signal component regardless of vibration direction, the pipe may be treated approximately as a plate.

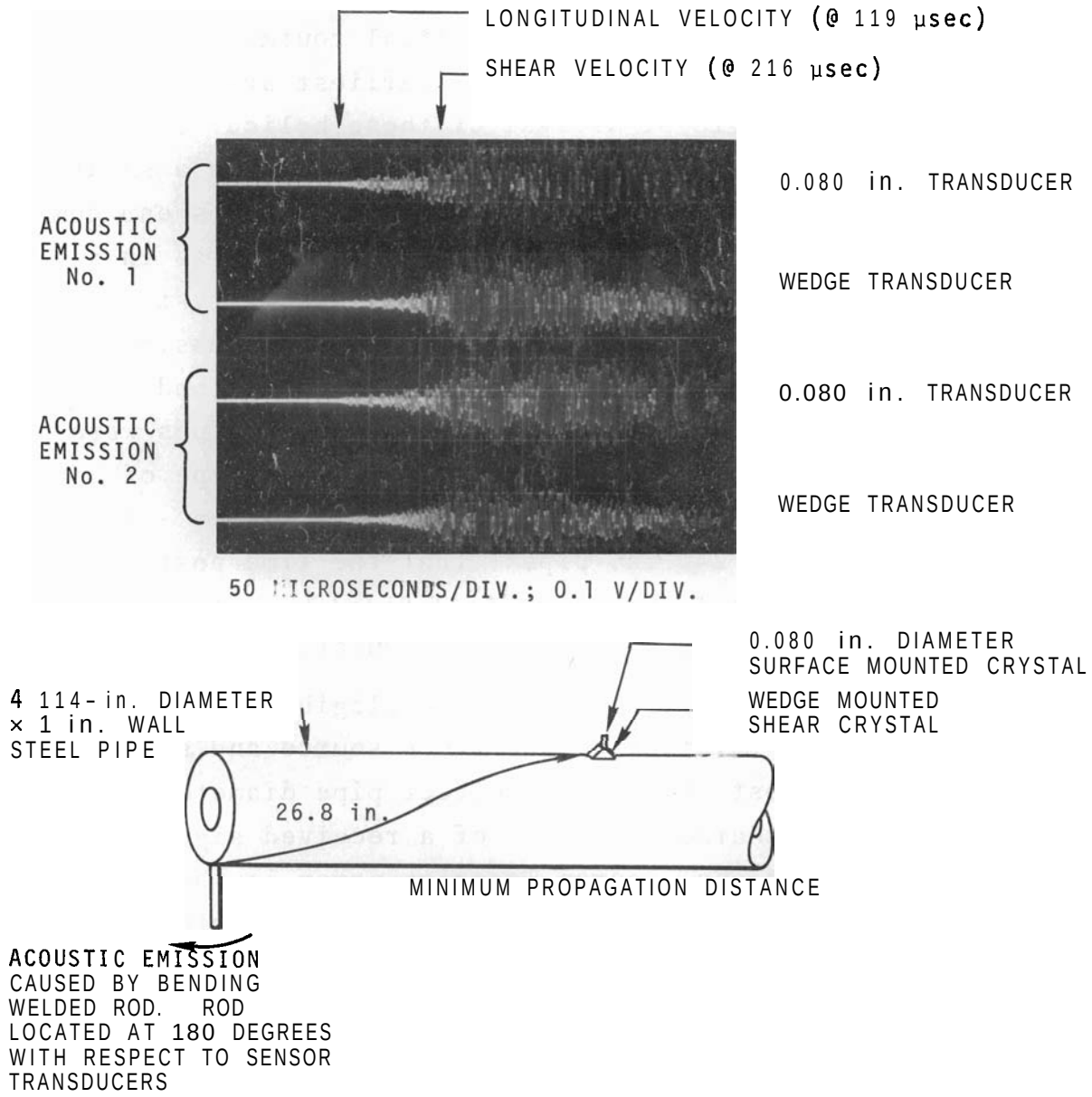

FIGURE 3.1. **Acoustic Emission Signals in 4 1/4 in. Diameter × 1 in. Wall Steel Pipe as Detected by Wedge and Surface-Mounted Transducers**

Effect of Distance on Earliest Arriving Signal Components

In contrast to the large, thick plate where earliest arriving signals frequently travelled at V_L - regardless of distance, earliest arriving signals in the pipes were found to arrive at decreasing velocities as distahce increased. Again, amplitude of the emission has a bearing on the apparent arrival times. In the 1 in. wall pipes, the most usual first - components arrival times lay in the range of 210,000 in./sec to 230,000 in./sec. The velocities range tends to move in the decreasing velocity direction as distance increases. For the 1/4-in. wall pipes, the first components arrival times lay in the range of 185,000 in./sec to 214,000 in./sec., again with a tendency for decreasing velocity as distance increases.

Examples of these velocity variations are seen in Figures 3.2 and 3.3 In Figure 3.2 are shown acoustic emissions in the 3 3/4 in. × 1 in. × 182 in. pipe as detected by the wedge transducer at 26 in. and 100 in. (top photo), and by the 0.080 in. transducer also at 26 in. and 100 in. (bottom photo). At 26 in., the earliest arriving signal components for both types of transducers travel at about V_L (230,000 to 236,000 in./sec) average for strong emissions, but at 100 in., they travel at about 218,000 in./sec average. For the weaker emissions, only the shear component was seen by the wedge transducer at either 26 in. or 100 in. ($V_S \simeq$ 123,000 to 126,000 in./sec); whereas earliest components seen by the 0.080 in. transducer appear at about 218,000 in./sec at 26 in., and at about 208,000 in./sec at 100 in. The effect of distance in the thick-walled pipe apparently depends largely on the amplitude of the emission. If the emission is strong, essentially the entire precursor may be detected at distances up to several feet and propagation velocity may be as fast as V_L; at long distance (beyond about 5 to 6 ft.) the fastest travelling parts of the precursor are not seen and earliest

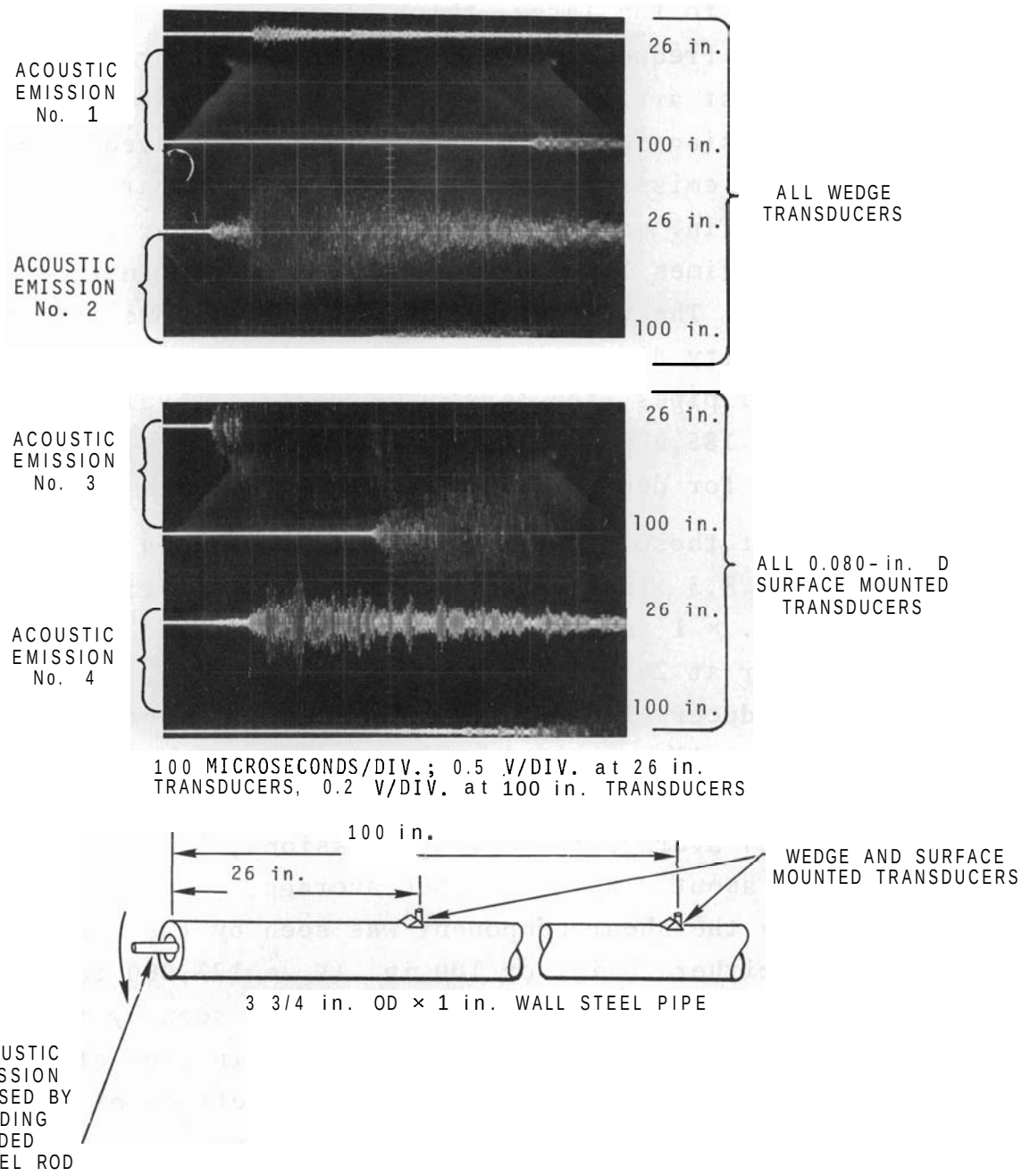

FIGURE 3.2. Acoustic Emission Signals in 3 3/4 in. Diameter × 1 in. Wall Steel Pipe as Detected by Wedge and Surface-Mounted Transducers at 26 in. and 100 in. Distance

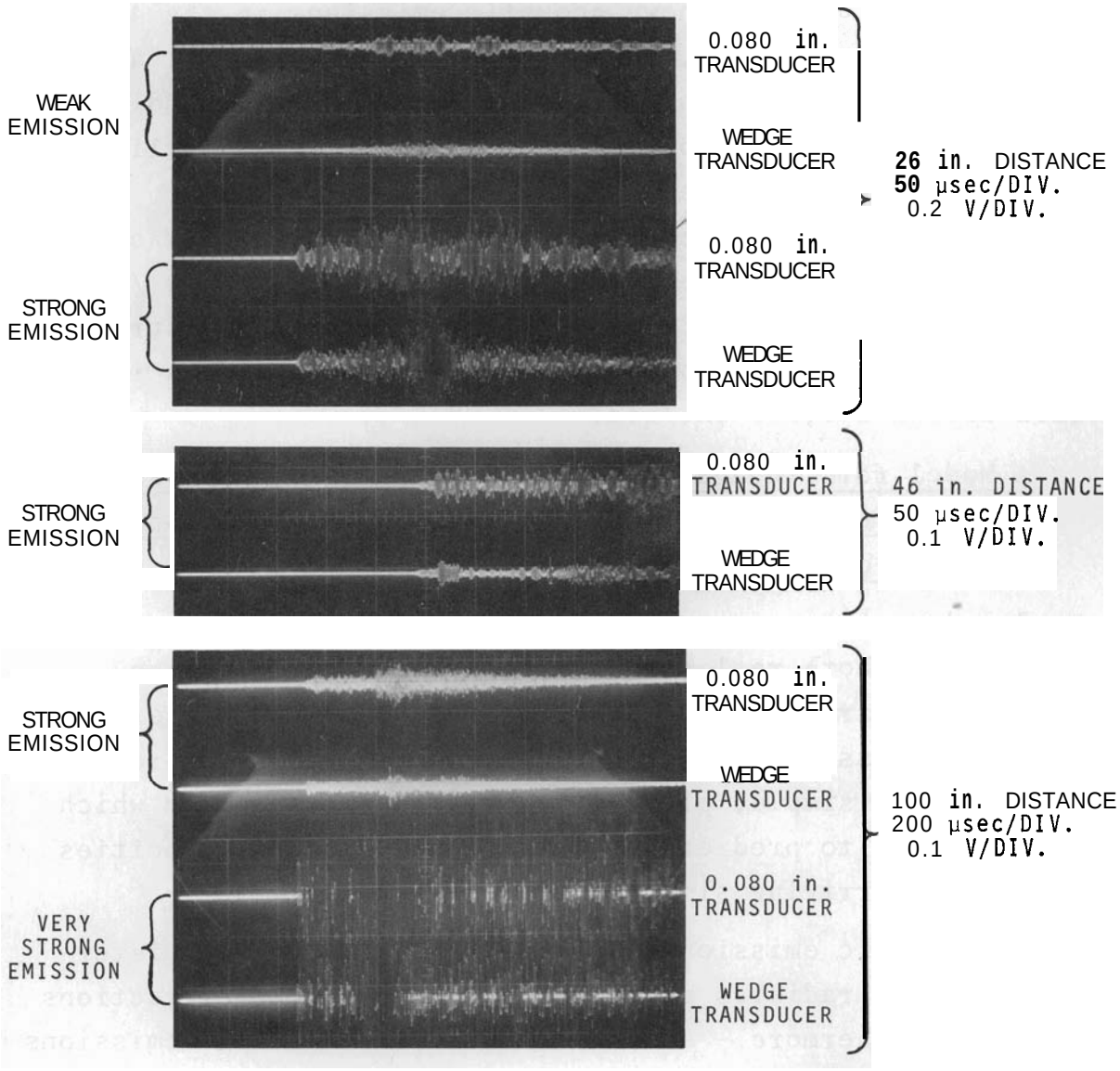

EMISSIONS CAUSED BY BENDING STEEL ROD WELDED TO PIPE

FIGURE 3.3. **Acoustic Emission Signals in 4 1/2 in. Diameter × 1/4 in. Wall Steel Pipe as Detected by Wedge and Surface-Mounted Transducers at 26 in., 46 in., and 100 in. Distance.**

arrivals at around 200,000 to 220,000 in./sec are probably zig-zag travelling longitudinal waves which have been phase reinforced at the sensor distance by other waves travelling more devious routes.

In Figure 3.3 are shown acoustic emissions in the 4 1/2 in. × 1/4 in. × 252 in. pipe, as detected by the 0.080 in. and wedge transducer at 26 in. (top photo), at 46 in. (middle photo), and at 100 in. (bottom photo). At 26 in., earliest arrivals for the strong emission travelled at about 211,000 in./sec and about 187,000 in./sec for the weak emission; at 46 in., 194,000 in./sec, and at 100 in., 193,000 in./sec for the strong emission and 208,000 in./sec for the very strong emission. For most emissions, propagation velocity is in the region around 200,000 in./sec.

A Model for Propagation of Acoustic Emission Stress Waves As Affected by Detection System Frequency and Propagation Medium Geometry

Based partly upon study of many hundreds of photographed wave forms of both real and artificial acoustic emission signals, and partly on accepted theory appearing in the literature, it is possible to suggest an acoustic emission propagation model for simple, plate-like structures; and from which it is possible to predict approximate propagation velocities for earliest arriving signal components.

An acoustic emission is assumed to be a complex disturbance; i.e., it radiates energy of all kinds in all directions and that, furthermore - sometimes there are multiple emissions taking place simultaneously or very closely spaced together in time. In general, however, the acoustic emission takes place as a short time duration burst and thus it is considered to be a pulse which originates at a point location and radiates a spherical wave front. It must be understood that bursts are never exactly reproducible; although they radiate as spherical

wave fronts, there may be more compressional energy travelling in a given direction than in some other direction for emission A; but the same may be true in different directions for emission B. The same would be true for shear energy, i.e., it may radiate in a spherical direction, but a spherical polar plot of energy would be different for each burst.

The concept of a single pulse does not preclude the existence of plate waves (Lamb waves or guided waves). The single pulse can be broken down into its continuous wave spectral components and on this basis it would be possible to predict the existence of various plate wave modes based on the plate or pipe wall thickness and the spectral content of the pulse. Naturally, the spectral distribution and energy levels for each frequency will vary from pulse to pulse, but if a narrow band detection system is used, and if plate thickness is known, then one could feasibly predict the detection of particular plate wave modes. Knowledge of which modes are apt to be present does not solve the question of just what is propagation velocity since a wide range of group velocities exist for a given mode in a given plate. Any velocity within the range may be indicated provided a detection system is sensitive to the frequencies associated with the velocities' dispersion range. For example, in a 1/4-in. wall thickness plate with a detector operating at a bandwidth of 600 kHz to 1.0 MHz, the second symmetrical mode group velocity may vary from about 96,000 in./sec to 200,000 in./sec as shown in Figure 3.4. The first symmetrical mode is probably present in emissions, but for a bandwidth of 600 kHz to 1 MHz in a 1/4-in. wall, the high velocity (low frequency) components are electrically shut out because of the high-pass filter (cut off at 600 kHz), and only the low velocity components get through - these arriving considerably after the arrival of the 600 kHz components of the second symmetrical wave. The higher

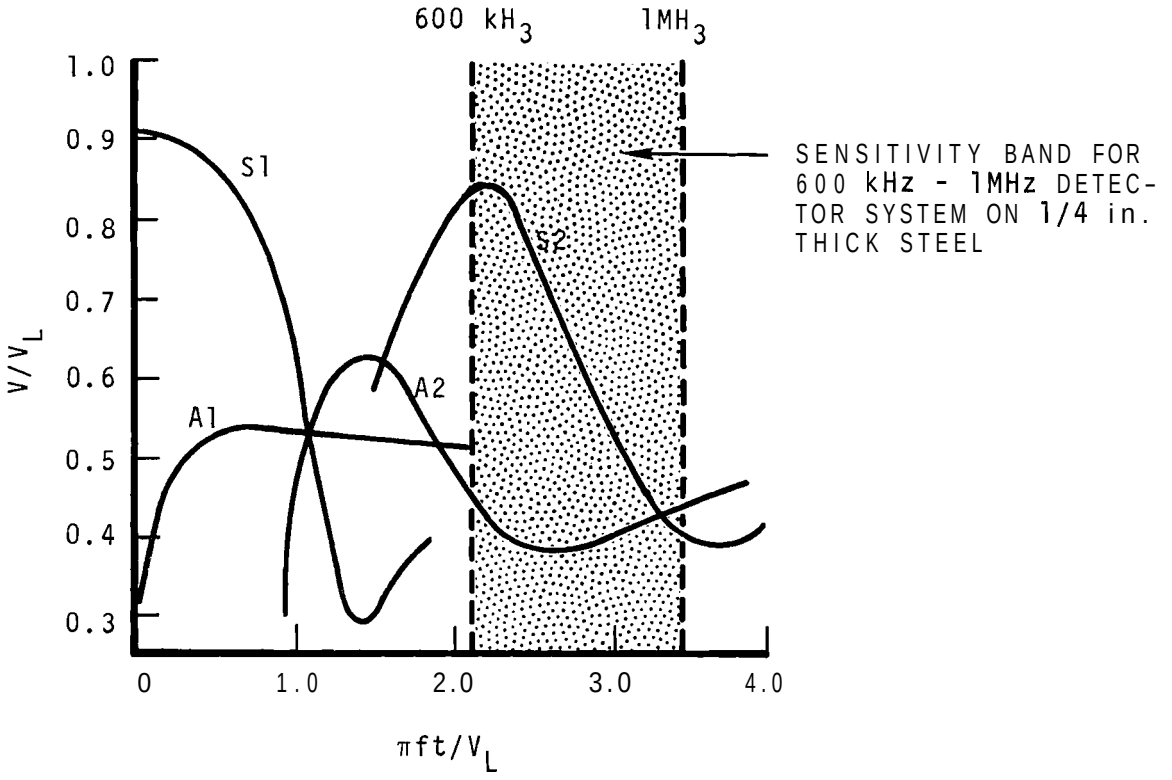

$V_L \simeq 230$ to 236×10^5 in./sec

V = GROUP VELOCITY

f = FREQUENCY

t = THICKNESS

S1 = FIRST SYMMETRICAL MODE

S2 = SECOND SYMMETRICAL MODE

A1 = FIRST ASYMMETRICAL MODE

A2 = SECOND ASYMMETRICAL MODE

FIGURE 3.4. Approximate Group Velocities Curves for "Plate" Waves in Steel

frequency components of the second symmetrical mode arrive at a lower velocity - very close to the velocity of the higher frequency components of the first symmetrical mode which also gets through the filter - so that reinforcement may occur resulting in some high amplitude beat frequencies - probably at about shear wave velocity. The first and second asymmetrical modes may also be present, but their group velocities are lower than the symmetrical modes and they would appear well back in the pulse (well after arrival of the faster components of the 2nd symmetrical mode). A study of the frequency components present in an emission, then, would show the lowest frequency of the system bandwidth appearing as the dominant frequency of the first high-amplitude arrivals (i.e., occurring after the low-amplitude precursor which travels at longitudinal wave velocity). Then, as the slower travelling components start arriving, the spectral content should increase in high frequency components. A wave form which may depict an example of the described velocity dispersion is seen in Figure 3.5. The top wave form is a wedge transducer detection of a signal at 6 in. from the source on the 8 1/2 in. × 1/4 in. × 120 in. pipe, while the lower wave form shows the same signal at 16 in. Attention is directed to fundamental frequency content of the earliest arriving components at 16 in. - appearing at about 82 to 100 μsec. Center frequency is about 600 kHz, and propagation velocity is about 195,000 in./sec for the earliest arrival. Further back in the pulse, beginning at about 150 to 160 μsec, appears a higher frequency component. Center frequency of this component is about 915 kHz, and propagation velocity is about 100,000 to 107,000 in./sec. Referring to the curves in Figure 3.4, it is seen that, for the second symmetrical mode, group velocity will be about 191,000 to 200,000 in./sec for the 600 to 650 kHz components; and group

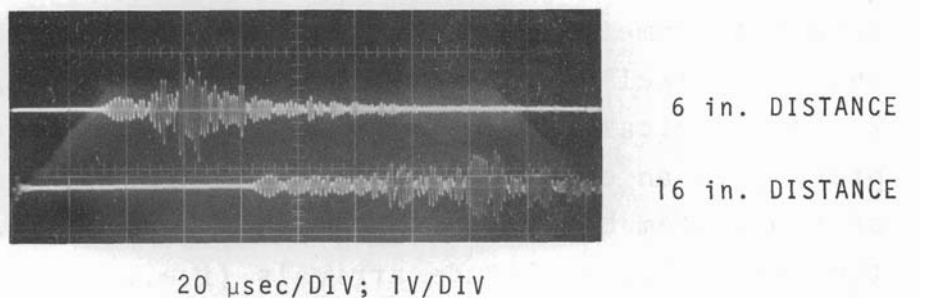

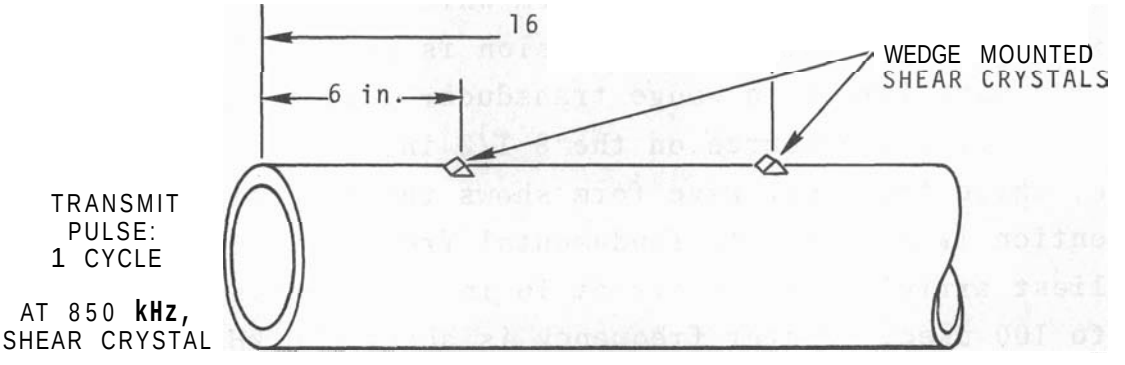

FIGURE 3.5. **Artificial Signal in 8 1/2 in. Diameter × 1/4 in. Wall Steel Pipe as Detected by Wedge Mounted Transducers at 6 in. and 16 in. Distance**

velocity will be about 110,000 to 115,000 in./sec for the ~915 kHz components. The detection of the 2nd symmetrical mode is thus indicated, the maximum velocity of which is about 200,000 in./sec at 600 kHz.

Using the same frequency bandwidth (600 kHz to 1 MHz), and in investigating thin wall material, the first detected arrival will probably be the first symmetrical mode since by going to a thin wall, the wave length - wall thickness relationship is such as to enable excitation and detection of the first symmetrical mode. Again, the fastest components will be the 600 kHz components which travel at about 207,000 in./sec (0.015 in. wall) to 213,000 in./sec (0.0625 in. wall). For a wall thickness of 1/16 in., the 1 MHz components travel at about 177,000 in./sec; whereas for a wall thickness of 0.015 in. the 1 MHz components travel at about 205,000 in./sec.

As wall thickness goes up - say to 1 in. - while frequency bandwidth remains constant (600 kHz to 1 MHz), the lower order modes (first and second symmetrical and asymmetrical) approach a constant velocity - surface wave velocity for the fundamental modes and shear wave velocity for all others. The same would be true for 4 in., 7 in., 10 in., and similar plates. With wall thickness this large, the pure wave components may be of more importance, i.e., the precursor longitudinal wave or the shear or surface waves. The plate waves that would also be present are probably low amplitude and they would arrive at about shear or surface wave velocity. If detection system bandwidth included very low frequencies (20 kHz to 100 kHz), low-frequency waves would again be found in plate waves travelling at a range of velocities - some of which would be much faster than shear velocity (e.g. ~207,000in./sec for the low frequency components of the first symmetrical mode).

It may be seen that some spectral information may be influenced by plate geometry; thus a crystal may be mounted to take advantage of a particular mode at a particular frequency whereas another similar crystal may respond to the same mode but at a slightly different frequency. Then again, the frequency - velocity relationship will affect frequency content of a selected portion of a received pulse. At a nearby location, the lows and highs may appear in the same time interval. At a distant location, the lows and highs are separated more from each other and may not appear in the same time interval. In addition, the highs are attenuated more than the lows so that analysis would have to be carried out at a location close to the source.

For now, it appears the best approach for triangulation purposes is to use the plate wave velocity for system frequency (f) x wall thickness (d) (MHz-in. $\times 10^5$) products lower than $\sim$2 or 3 where the frequency bandwidth is selected to minimize ambiguity. For fd products greater than $\sim$2 or 3, the least ambiguity would arise if the precursor could be detected enabling use of $V_L \simeq 230{,}000$ in./sec. As a rule of thumb, the maximum detection distance for the precursor $\simeq$ 10-20 $\times$ wall thickness. Thus, for a wall thickness of 4 in., groups of sensor transducers could be spaced about 40 to 80 in. apart and still have a fair chance of picking up the precursor out of the noise for most signals. Further work is needed in the area of acoustic emission signal propagation characterization to confirm the above results and translate them to beneficial application.

The effect of temperature on generation of detectable acoustic emission is of significance particularly in the case of austenitic stainless steel. Experience has shown that stainless steel tends to be less responsive in terms of acoustic emission than other materials even at room temperature. Work is in progress to determine the relative emission response of

Type 304 SS specimens which failed in tension and fatigue at room temperature, 600 °F, and 900 °F. Room temperature testing and a limited amount of work at 600 °F has shown no detectable temperature effect. Other tasks include:

Task 2 - Sensor Development
Task 3 - Signal Conditioning System
Task 4 - Data Analyzer and Readout System
Task 5 - Application Engineering.

There are no significant developments on any of these tasks.

Task 6 - Cooperative Work with Idaho Nuclear. A meeting was held with Idaho Nuclear Inc. (INC) at Idaho Falls on December 15, 1969 to review a joint work plan and a similar meeting was held at AEC Headquarters on December 17, 1969 between DRDT, INC and BNW. Work plans are being revised to conform to DRDT Program Letters

Work Planned for Next Quarter

Work for the coming quarter will be confined to improving acoustic emission detection and data interpretation for hydrostatic test application.

4. ENVIRONMENTAL STUDIES

CALCULATION OF THE POTENTIAL ENVIRONMENT RADIOLOGICAL CONSEQUENCES OF REACTOR ACCIDENTS - M. M. Hendrickson

An important part of estimating the potential environmental radiological consequences of reactor accidents is the calculation of the external whole body dose from the airborne plume of released material and from the contained fission products.

There is wide variation in methods used for calculating this dose. The resulting calculational estimates from these different methods also vary widely as evidenced by a survey conducted by Gammill and Van derHoven.(1)

The current objective of this program is the development of an improved method of making this calculation; a method that is accurate, rapid, widely accepted and readily usable.

The estimation of consequences requires the use of methods and models spanning several disciplines and preferably data from many tests. Progress to date has been to describe a method of solving the problem, derive the equations which correspond to the description and program the equations derived for high speed computer solution.

One of the major problems encountered in the past has been that of adequately representing the phenomena involved in a complete solution without using excessive time on the computer.

The main difference between the solution which is being developed and other methods is the completeness of the solution combined with rapidity. Program rapidity has been achieved by using a mathematical technique which appears to be well suited for this particular problem. The equations developed are not integrable analytically. The technique

adopted is to perform a numerical integration of the dose rate over space and time by using an 8th order polynomial fit to grid point data. The grid point data represent the dose rate per unit volume which when integrated over volume and time give the dose from the cloud. The program permits calculation of the external radiation dose received at a downwind point for any desired exposure time.

Included in the computer program is an optional analytical solution for calculating fission product inventories. The decay and formation of from 1 to 500 isotopes (based on the initial inventory) is followed accurately throughout a simulated release through a multiple barrier containment system and as the released activity travels in the plume.

Optional meteorological models are available in the program so that plume dimensions can be described in any of the ways commonly in use.

Seven members may be used in any decay chain and the decay scheme of each member may be defined by 16 energy groups.

The method of solving the problem and the computer solution technique are being documented. This method is proposed as the basic approach to be used for reactor accident calculations throughout the U.S. by reactor licensee applicants, AEC contractors, and DRL.

The next objective is to distribute a description of the proposed method to interested parties and solicit their comments. The eventual result should be a relatively uniform approach or method in cloud dose calculations.

The importance of achieving greater uniformity in cloud dose calculations becomes apparent from the survey conducted by Gammill and Van derHoven.

In the survey, large differences were found among results of cloud gamma dose calculations for the test problem they prescribed. The differences were especially large for distances close to the source. Calculations based on semi-infinite cloud assumptions in most cases (as expected) showed a higher dose compared to integration over finite cloud dimensions. Differences were unexpectedly large at distances where semi-infinite cloud and finite cloud calculations should have been close. Gammill and Van derHoven suggested several reasons for the differences.

This study has added several'more reasons for differences which were observed in the test problem and which might be observed in a more general problem. In a more general problem, the differences would have been even greater than were observed had each participant used his normal calculational approach.

An unexpected cause of difference was the choice of limits of integration for the cloud dose. The limits chosen by participants indicated widely different interpretations of the exposure times specified in the problem.

It was also found that none of the methods used and their corresponding computer programs had a comprehensive capability of accounting for the major phenomena involved in an accident. The most common omission was to disregard the behavior of aerosols in containment. In addition, most codes were designed with single barrier containment systems in mind and thus they introduce a large error in estimates of consequences for multiple barrier systems unless a compensating factor is introduced.

One general deficiency of the codes was that none attempted to estimate the error introduced by various simplifying assumptions. However, it should be noted that where

simplifying assumptions were made they were made (with a few exceptions) in the direction of added conservatism. One non-conservative assumption generally has been to truncate the radionuclide decay chains and then to select only noble gases and iodine for the cloud dose. For one sample case it was found that this resulted in a 25% underestimate of the dose.

Other sources of variation in results were (or could be in a more general problem):

- The application of the algorithms in the numerical integration. This applies to codes which integrate over cloud dimensions.
- The application of short term meteorology models (10 min to hours) to long term (1-day to 30-days and over) dose calculations.

  The method of assigning the source activity to various points in space and time for the cloud dose integration.
- The use of a single group attenuation kernel rather than multigroup.
- Use of semi-infinite cloud assumptions at distances close to the source where a_Y and σ_z are small compared to the γ relaxation length.

  Dose Correction Factor for Finite Versus Semi-Infinite Clouds

To determine the effect on cloud dose calculations of finite versus semi-infinite cloud assumptions the latter was corrected by Healy's method. In the 1968 edition of Meteorology and Atomic Energy (Section 7.5), Healy describes Gamertsfelder's methods of estimating the cloud dose, and develops a method of comparing finite and semi-infinite cloud gamma dose calculations. The reader should refer to this section (7.5) to understand the method and should understand Figure 7.14 especially.

Gamertsfelder and Healy make numerous simplifying assumptions in order to make the problem solvable. Remembering that the effect of these assumptions has not been evaluated it is nevertheless interesting to look at the ratio of finite to infinite cloud dose which Healy develops to see what the test problem results would be with cloud size correction factors applied.

Correction factors are plotted in Figure 4.1 (obtained with Healy's method) which are as nearly applicable as possible to two of the test cases, and the correction curves have been applied to the test case data. The cases studied are:

24-hour, ground level source, Type C, Figure 4.2a and 4.2b

1-hour, ground level source, Type F, Figure 4.3a and 4.3b.

The data supplied by participants is shown in Figures 4.2a and 4.3a. These data were then replotted (omitting previous curve H) after applying finite cloud correction factors to the semi-infinite cloud calculations. The corrected data appear in Figures 4.2b and 4.3b.

Cloud Size Correction Factors

It is emphasized that the cloud size correction factors in Figure 4.1 give only an approximate correction. Not only are they limited by the assumptions of a single gamma decay energy (Ey = 0.7 MeV) but by all other inherent limitations of the Healy-Gamertsfelder model.

Elevated Release, The model was not meant to be applied to an elevated release case. However, an approximate answer was obtained by correcting for a nonisotropic cloud (Type F conditions, ground level release) and then interpolating from

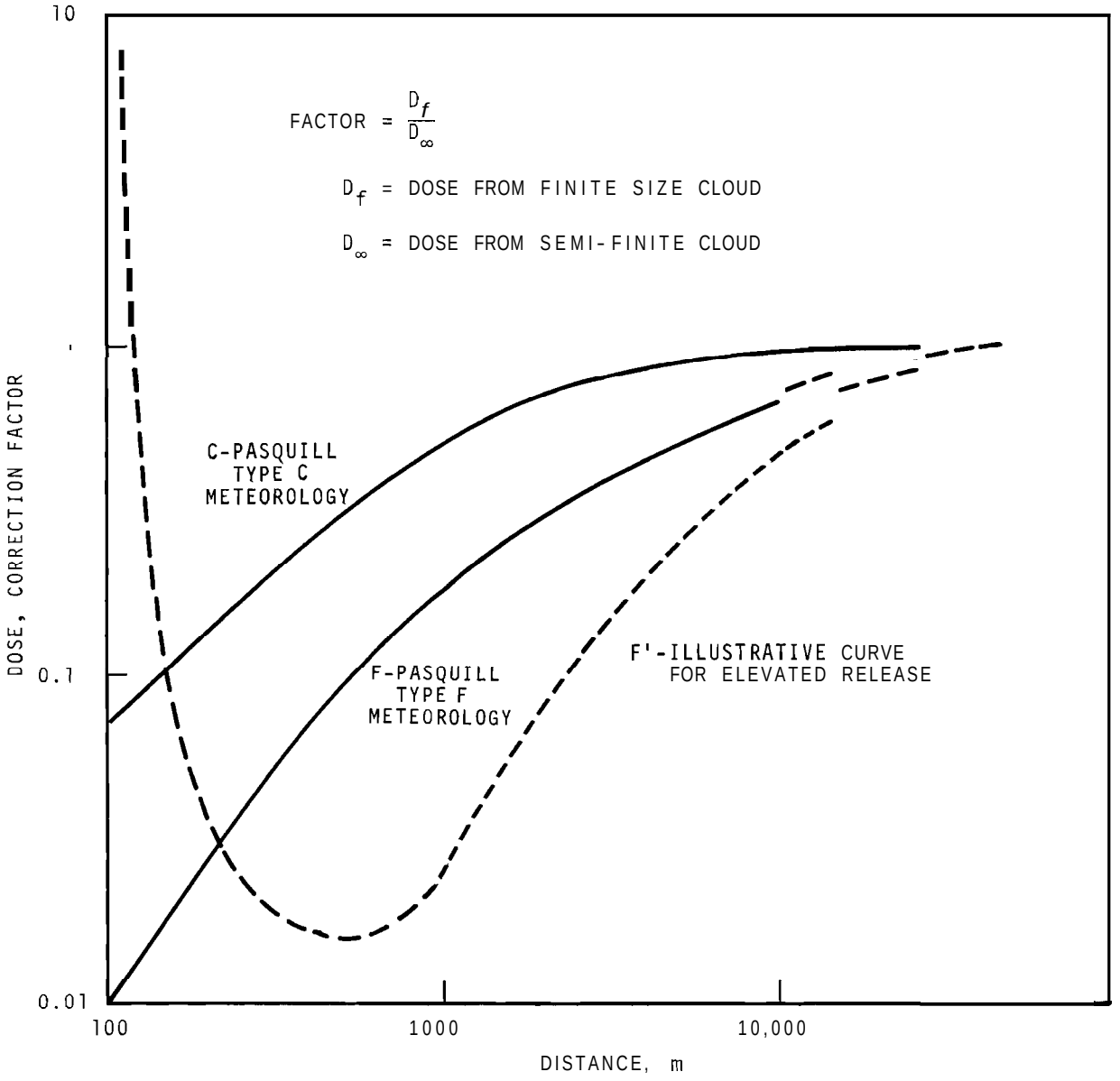

FIGURE 4.1. **Cloud Size Correction Factors (for Pasquill Type C and F Conditions) as a Function of Distance from the Release Point**

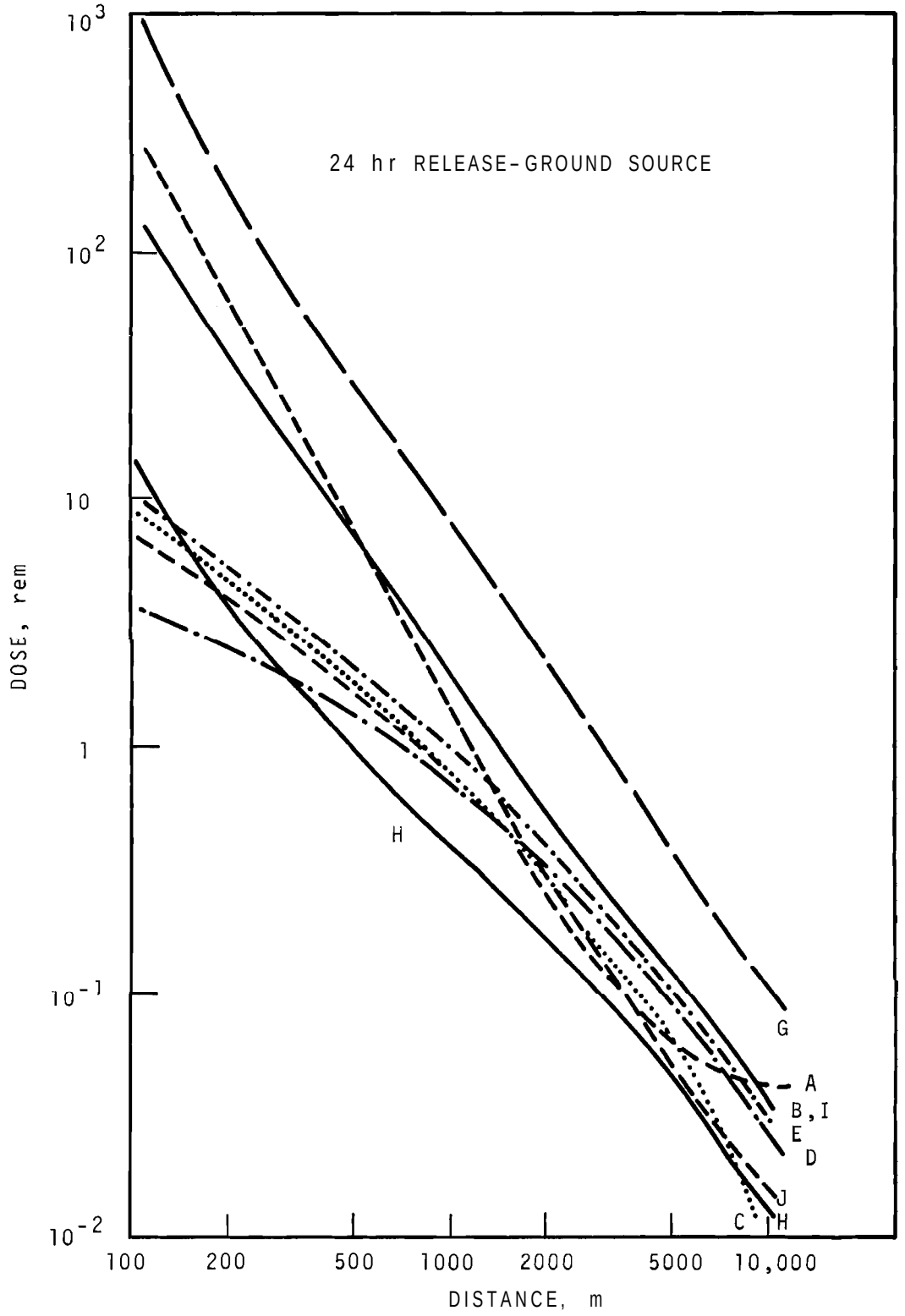

FIGURE 4.2a. **Cloud** Gamma **Dose, Type C, 4** m/sec

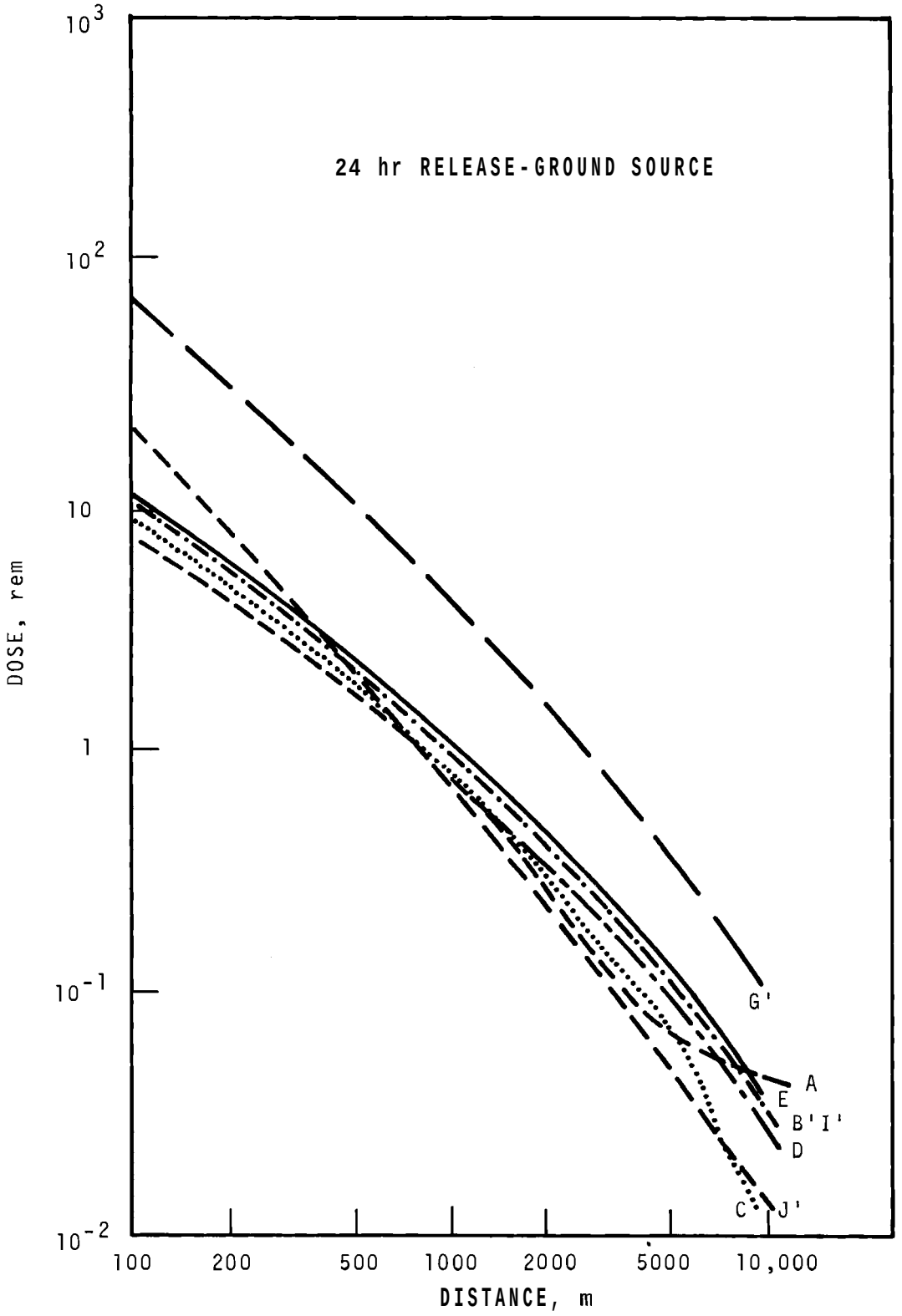

FIGURE 4.2b. Cloud Gamma Dose, Type C, 4 m/sec

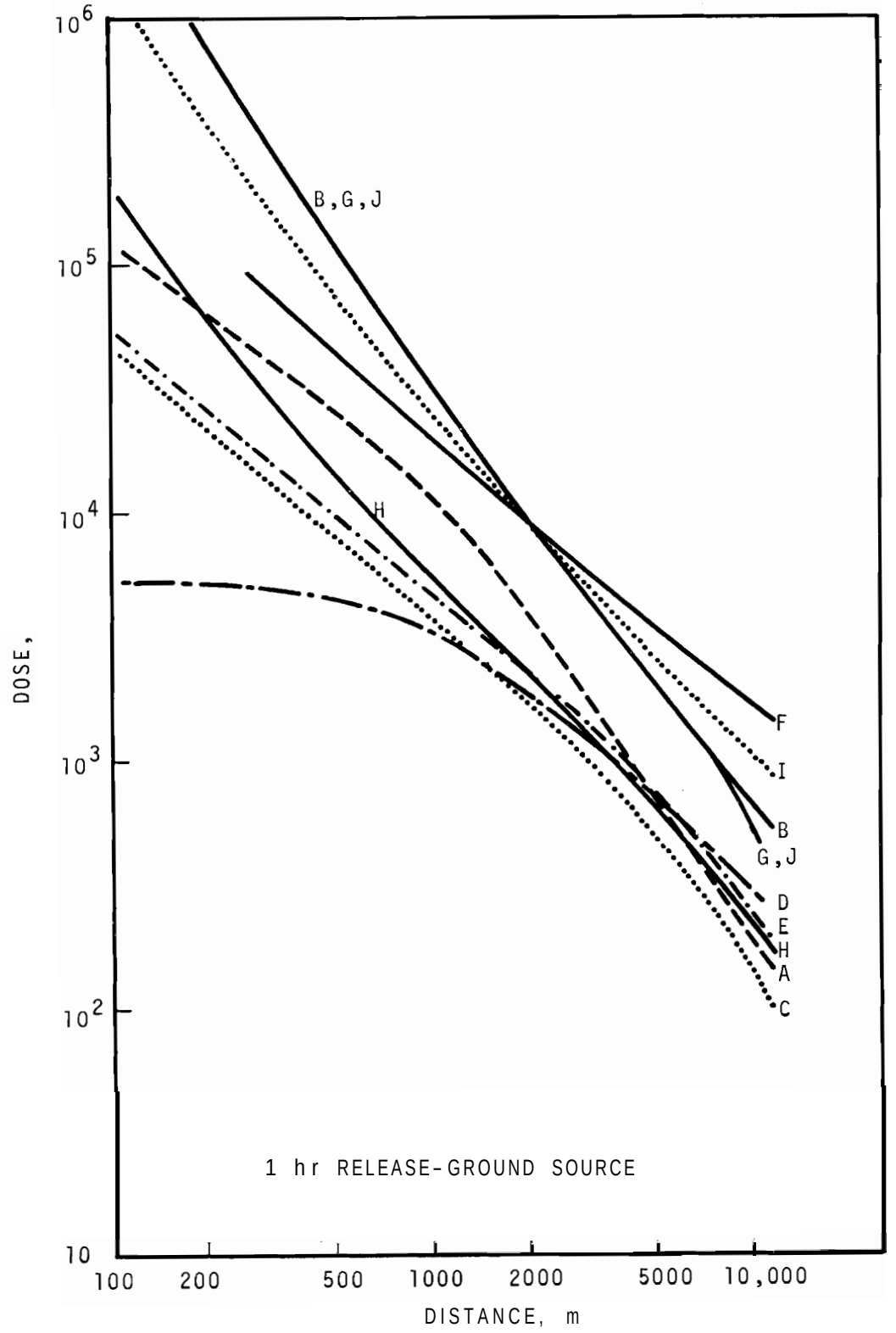

FIGURE 4.3a. Cloud Gamma Dose, Type F, 1 m/sec

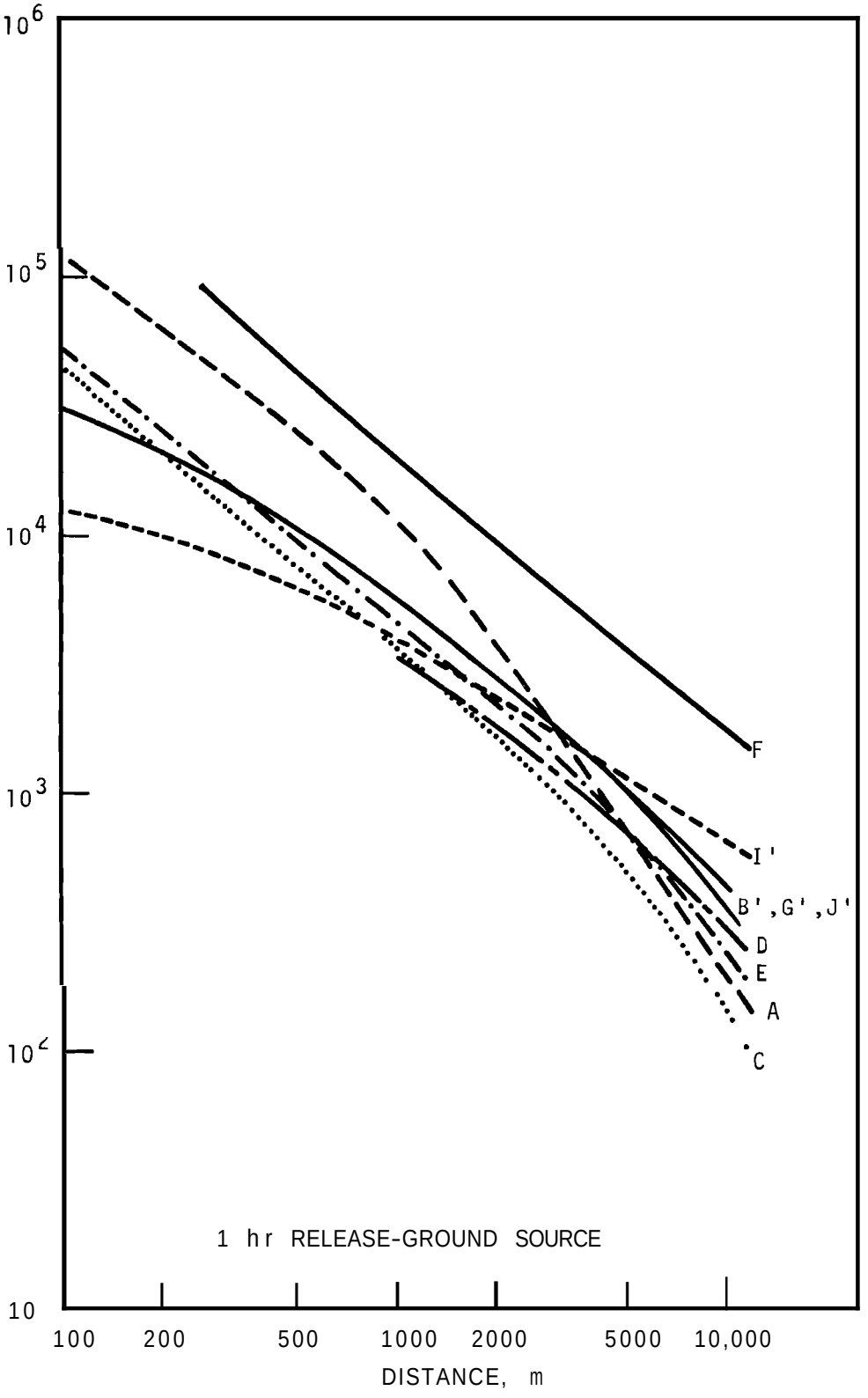

FIGURE 4.3b. Cloud Gamma Dose, Type F, 1 m/sec

Figure 7.14 to account for the 100-meter release height by moving off the cloud centerline a distance y which is equivalent to the stack height. The correcticn curve obtained is for illustrative purposes only (Figure 4.1, Curve F').

Ground Level Release. For the ground level release case the correction was much simpler. Figure 4.1 gives cloud size correction factors to apply to semi-infinite cloud gamma dose calculations. These factors when multiplied by the dose calculated by using semi-infinite cloud assumptions give approximately the dose from a finite cloud. The factor is a fraction and is plotted as a function of distance from the source from 100 to about 50,000 meters.

For Type C conditions and ground level release (Curve C, Figure 4.1) the correction factor rapidly approaches 1.0. At 1000 meters it is 0.5, at 2000 meters 0.7 and at 5000 meters 0.8. This indicates that for unstable or neutral conditions the semi-infinite cloud dose calcuiation is not (or at least should not be) greatly different from what. one calculates by more sophisticated methods at distances of several miles.

For Pasquill Type F and ground level release (Curve F) differences between the two methods are rather large until distances of several thousand meters have been reached. At 1000 meters the factor is about 0.2, at 2000 meters 0.3, at 5000 meters (about 3 miles) 0.5 and at 15,000 meters (about 9 miles) about 0.8.

For Pasquill Type F (moderately stable atmosphere) and an elevated, 100 meter, release the error in a semi-infinite cloud calculation is large until very large distances, probably 10,000 meters or more, are reached. At 10,000 meters the factor indicated by Curve F' is 0.5. The semi-infinite cloud dose calculation can have very large error close to the source, for example the correction factor is about 0.01 at

600 meters. As the source is approached a minimum is reached, then the factor begins to increase. Very close to the release point the factor may be much greater than 1. This is because near the release point the ground level air concentration is almost zero. Consequently the dose calculated using semi-infinite cloud assumptions is almost zero, and the corresponding correction factor would be a very large number. Curve F' is meant only as a qualitative demonstration of the relationships between semi-infinite and finite cloud dose calculations and should not be used to obtain correction factor values.

Corrected Doses for Type C Conditions - 24 Hour Release

Figure 4.2a gives the doses as reported by participants in the test problem for 1 case, Type C conditions, 24-hr release. Curves B, I, G and J are derived from semi-infinite cloud assumptions. The other curves are derived from use of some finite cloud integration technique. In Figure 4.2b the doses have been replotted after applying correction factors from Figure 4.1 to the semi-infinite cloud cases. The result is that all the curves are close over a considerable range except G and J the former being consistently high by almost an order of magnitude and the latter having a different slope, being initially higher and eventually lower than most others.

For 'Type C conditions (Figure 4.2a and 4.2b) the difference between finite and semi-infinite cloud calculations should be about 12% at 5000 meters and 8% at 10,000 meters if all other parameters are the same between cases (see Figure 4.1). However at 5000 meters the spread is about a factor of 3 (or 300%). This is obviously more than can be accounted for by correcting for finite versus semi-infinite calculations. Considering the inventories reported by Gammill and Van derHoven Curves A, E and J should be high at time 0 to 3 hours and B should be low. This is the case. The order of the curves (from top to bottom) for longer times should be B, E, then J.

This is also the case. It appears that initial inventories can explain part of the remaining differences in the curves.

Corrected Doses for Type F Conditions

Figure 4.3a gives the doses as reported by participants in the test problem for a second case; Type F meteorology and one hour release. Once again correction factors from Figure 4.1 have been applied and the data replotted, Figure 4.3b. Not as good agreement is obtained in this case as in the previous one. Some possible explanations follow.

The major reason for Curve A being high for the 1-hr case (Figure 4.3b) is probably the choice of integration time. The choice of limits is such that the dose should be overestimated when the exposure time exceeds the release time, which it does. Compared to the other curves this appears to be true and the overestimate may be a factor of 5 to 10. For exposure time equal to release time the dose calculation should be correct and Curve A is close to the others in Figure 4.2b, the case where release time equals exposure time. The participants supplying Curve D were uncertain as to the accuracy of calculations at distances closer than 600 meters, so this part of the curve was deleted on Figures 4.2b and 4.3b.

Looking at total inventories for the various classes of fission product, it appears that inventory differences are not high enough to account for the remaining differences between corrected dose values. However, the total fission product inventory may not reflect the differences that may accrue from differences in inventories of specific isotopes; for example, ^{88}Kr is a very important contributor to the cloud dose. A comparison of the most important noble gas inventories is being made.

Curves A, B, C, D, E, and I all cluster together differing less than 30% at 100 meters but they diverge increasingly as

distance increases (Figure 4.2b). This may be partially accounted for by the way participant B calculates their inventory with daughters fed continuously by precursors. Participant C does not include growth from precursors during travel or in containment after shutdown and thus his calculation should predict a lower dose, which it does. No satisfactory explanation for G' and J' has been developed at this time.

REGIONAL MODELING OF SURFACE WATER TEMPERATURE FROM PROJECTED POWER GROWTH - R. T. Jaske and D. E. Peterson

In the case of thermal effluent in an irrigation system, the essential purpose of the study was realized to an extent in keeping with the available data base. Good simulation of the hourly temperatures of the canal downstream of the operating thermal plant with the COLHEAT computer code was achieved using weather data from a number of remote sources. The value of the overall heat transfer coefficient U_C was determined to be somewhat higher than values obtained from lakes and relatively swift rivers. Because of the absence of either a positive or negative history of the agricultural effect of the warmed water during the irrigation season, no significant effects could be determined for this case. The simulation of the addition of a 500% increase in heat rejection to the canal system indicated a large potential heat sink capability for future expansion of the system without extensive modifications of the simulated thermal history. The following specific conclusions were derived from the study:

- The investigation of the cooling capacity of the main canal system reveals relatively large and previously untapped heat sinks of considerable value in the planning for future power systems. The computed rates of heat transfer from the canal indicate overall coefficients as high as 700 Btu/(day)(ft^2)(OF). This is considerably higher than values calculated on open lakes and ponds which range from 100 to 200 Btu/(day)(ft^2)(OF). Net values on the Columbia River are higher than those for open lakes and ponds because of the surface turbulence. The high values obtained in the instant study are about twice the values nominally used for cooling ponds and may reflect the absence of boundary layer limits ordinarily expected on large lake surfaces. The results point up the importance of additional research in the determination of surface exchange coefficients in varying surface geometrical configurations.

- The high heat transfer rates obtained from the simulation (see Figure 4.4) suggest that the use of an extensive canal system for the routine enhancement of agricultural production either by soil warming or boundary layer modification of the local weather may be considerably less appealing because of high investment costs in water distribution piping or insulation of main conduit to conserve heat. Conversely, the use of large artificial canal systems as part of pumped storage nuclear and fossil power stations suggests a means of providing a large dependable energy base away from existing river systems.

Average monthly direct cooling capacities, within a temperature envelope of 5 °F, of the Ohio River Basin are indicated in Figure 4.5 and Table 4.1. The total column includes both assimilative and dissipative capacities of the main stem

and larger tributaries (assimilative capacities only for the Tennessee and Cumberland Rivers) whereas, the maximum input columns include assimilative capacities at several locations along the main stem.

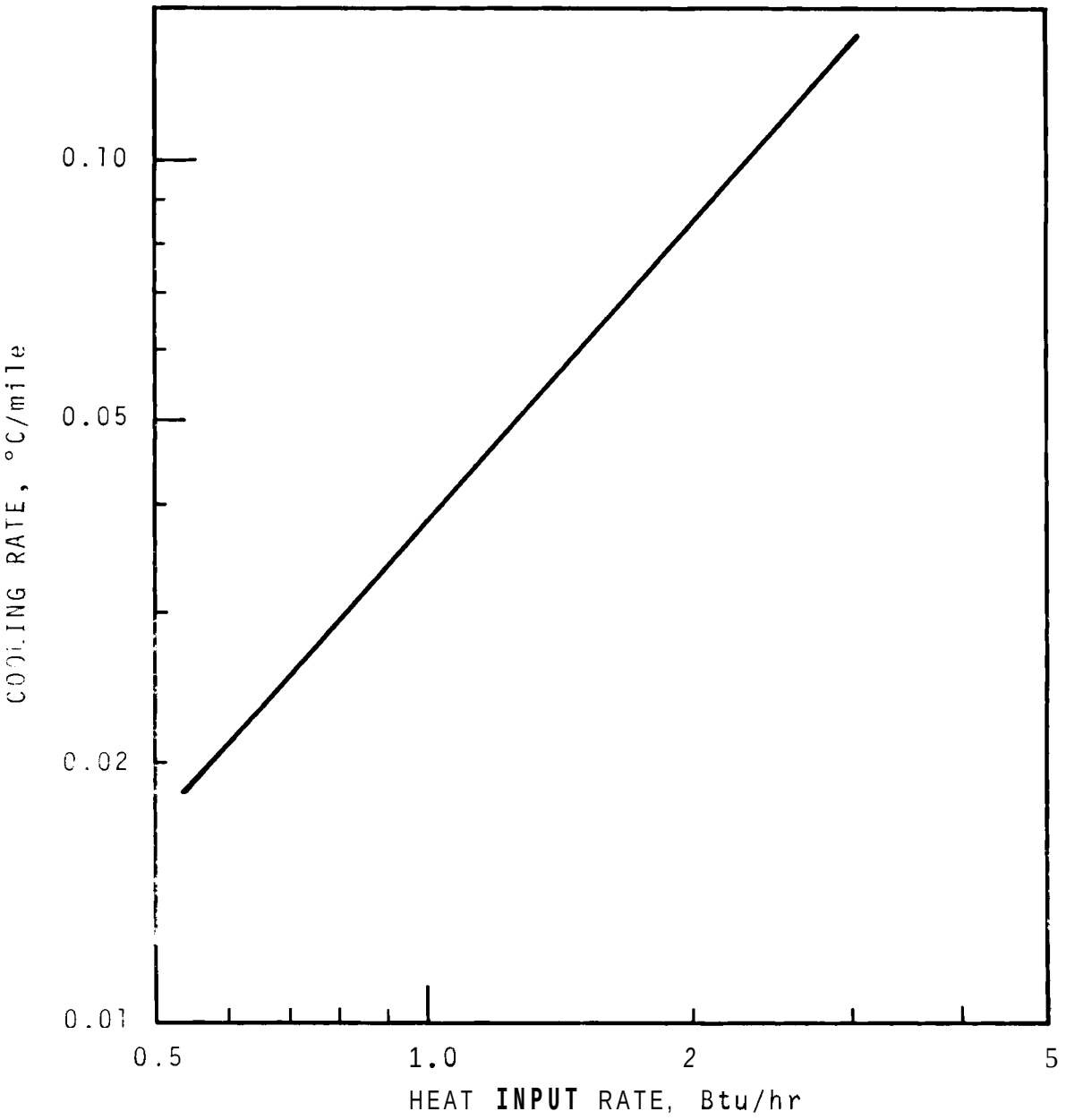

FIGURE 4.4. **Cooling Rate, °C/mile, as a Function of** Input **Heat Rate**

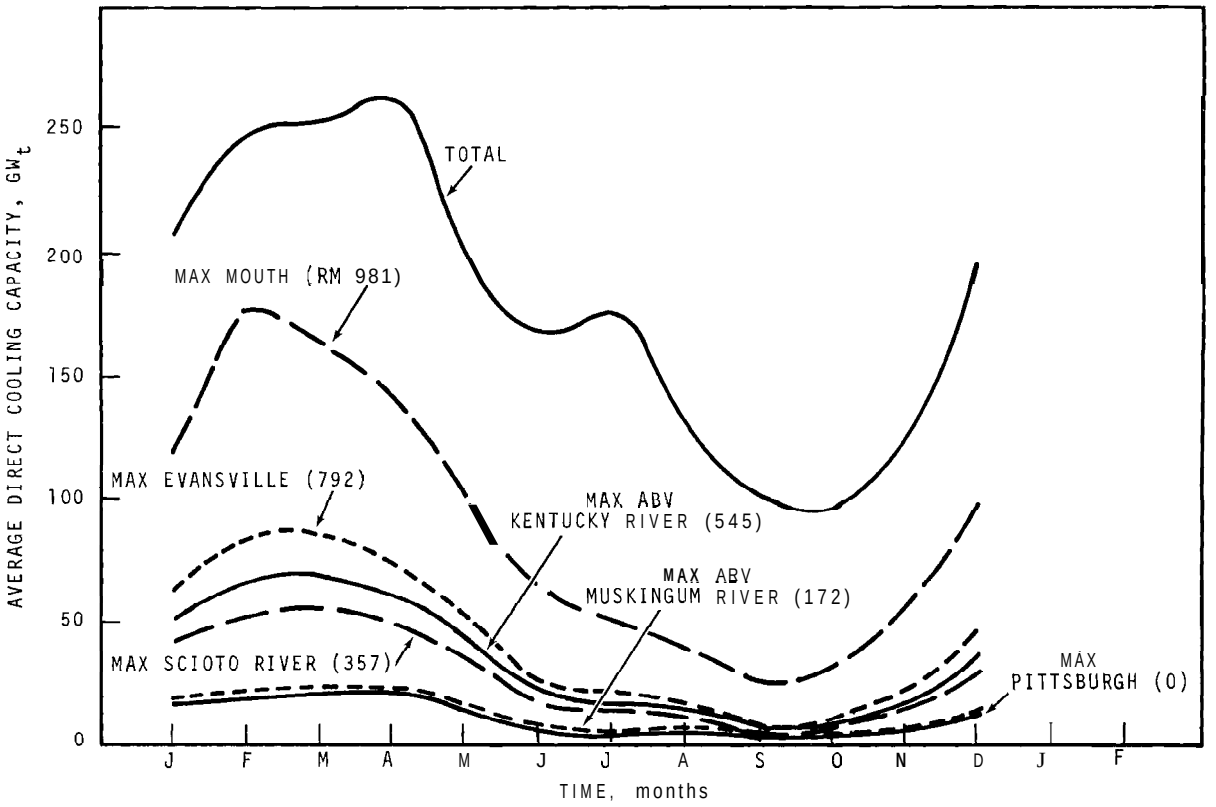

FIGURE 4.5. Average Direct Cooling Capacity of Ohio River Basin

TABLE 4.1. Ohio River Basin Average Direct Cooling Capacity (MW_t)

Month	Total	Maximum Input-RM 981	Maximum Input-RM 792	Maximum Input-RM 357	Maximum Input-RM 172	Maximum Input-RM 0
January	208,000	120,000	64,400	48,900	26,300	17,400
February	247,000	176,000	93,100	65,400	29,600	18,700
March	251,000	163,000	92,100	65,800	31,100	20,700
April	261,000	143,000	80,000	59,000	30,800	20,600
May	198,000	100,000	55,700	44,800	21,900	14,200
June	168,000	63,000	29,000	20,600	11,400	7,500
July	176,000	51,000	22,400	16,200	8,400	4,900
August	129,000	40,000	16,800	12,900	7,600	4,900
September	102,000	26,000	8,900	7,100	4,400	2,900
October	95,000	29,000	11,000	9,300	6,200	4,500
November	123,000	51,000	21,500	15,300	9,300	7,100
December	195,000	98,000	49,600	36,000	19,500	13,600

Federal Power Commission projected 1980 and 1990 steam electric capacities for the Ohio Basin are 75,000 MW_e and 130,000 MW_e respectively. Within the constraints indicated above, it can be stated that under average monthly conditions, the thermal capacity of the Ohio river system is limited in September and October because of natural flow reductions. However, during 10 months of the year, sufficient capability exists to handle most needs for thermal effluent disposal for most of the forecasted power demands through the end of the century. The power industry appears faced with the problems of adapting more flexible design options which permit the advantages of low cost direct cooling during most of the year to be supplemented by ancillary cooling during the critical months. In addition, the careful attention to scheduling of shut-downs and ancillary gas turbine systems offers additional possibilities while strengthening system reserves.

The study reveals important avenues of approach in the future management of water resources systems which will permit all interested parties to derive the maximum benefit from technology without catastrophic impairment of traditional resource values for recreation and other uses; or the arbitrary assessment of increased operational costs throughout the year because of a short seasonal problem.

The following specific statements are derived from the study:

- Under average conditions, by 1980, the flow-through cooling requirements for single-stage, direct-cooled plants which could be sited on the Allegheny River will exceed the stream capacity in late summer and early fall. With systems using two-stage cooling combinations of topping ponds or topping towers a considerable extension of the time could be achieved. A ratio exceeding 3.0 between average and minimum capability exists on the

Allegheny. This ratio indicates that if supplementary cooling were employed on a flexible basis, sufficient capacity exists to handle all cooling requirements for the foreseeable future.

- The Monongahela River is capable of additional development of a flexible basis; however, under present, once-through cooling designs, the capability is sufficient to match the 1980 requirements. Some allowance for continued use by other industry would also require factoring a specific study directed to an actual allocation.
- On the basis of data collected for the study, it appears that the Muskingum River cannot attenuate present loads and remain within a 5 °F differential during September and October. This river could be a potential test basin for the development of flexible supplementary cooling methods with seasonal adjustments.
- The Kanawha River presently receives extensive heated effluent from chemical and primary metal production facilities in addition to electrical generating plants. Additional development of the river for direct cooling on a flexible basis could be accomplished, the flows being provided that supplementary cooling for the later summer and fall periods could be installed. Under single-stage, direct cooled operation, the critical low flow capacity is less than 250 MW_t.
- Conditions on the Wabash River are similar to other streams discussed. Some additional development appears possible; however, the low flow extremes in summer and fall indicate the need for use of flexible systems or scheduled operation by 1980.
- For the Ohio River Basin as a whole, extensive additional cooling capability exists below Evansville. This is

expected to total at least 10 GW_e under average conditions during the summer and fall. With supplementary ponds or topping towers, as much as 40 to 50 GW_e could be handled within the study assumptions. The middle river, largely between Huntington and Cincinnati, which has few steam plants at present, is also a potential area for development. Again, possibilities for flexible design or operation exist. Under the maximum condition of development and with some partial supplementary cooling, the entire needs of the area could be accommodated through the foreseeable future. Without supplementary cooling, the available siting possibilities would be totally committed by 1984.

- The study has developed additional opportunity to investigate the tendency to aggregate thermal capacity in super plants of very large rating. This aggravates the general problem of heat dissipation because of the limitations on the local temperature rise imposed by State Standards under the Water Quality Restoration Act of 1966, especially in the upper reaches of the study area. The data developed for the individual sub-basins supplying the Ohio River Basin is especially useful in detailing the specific interdependence of plant size, load factor and seasonal stream capacity. These facts suggest that the optimization processes involved in plant size determination should include the entire system from water source to heat sink in the venture analysis supporting process selection. Such study should include review of such practices as high back-end loading. Though high back-end loading nominally shows advantages in leveling the sensitivity of plants to changes in condenser temperature, it does so at the cost of higher total plant heat rate with attendant increases in overall heat discharge to the

total environment. As a corollary, the study suggests the retention of lines of smaller, flexibly designed plants which could be used for regions which could incorporate direct cooling on smaller streams with appropriate electrical flexibility for low voltage regional systems.

- Finally, the study suggests the development of the concept of dynamic planning and management of stream temperature resources using the latest in computer simulation as an alternative to the use of rigid practices administered in an inflexible manner. Both the power industry and the regulatory agencies appear to have much to gain from the use of such practices in preservation of the quality of the environment and the low cost of power and other services to the ultimate consumer.

Average monthly direct cooling capacities have been calculated for the Upper Mississippi Basin from St. Cloud, Minnesota to Alton, Illinois (above the Missouri River). The range was found to be between 109,000 MW_t in April and 51,000 MW_t in November. Simulations of low flow capacities for both the Upper Mississippi and Ohio Basins were also completed during the report period. The results of these studies are scheduled to be published under the classification of "Waste Disposal and Processing" (UC-70) in March 1970.

Basic data for studies of the thermal regimes of the Missouri River Basin and the Great Lakes are being acquired. Initial screening and assemblage of the information for computer input is scheduled for late February.

SIMULATION MODELING OF ENVIRONMENTAL EFFECTS OF THERMAL GENERATION - R. T. Jaske, J. C. Sonnichsen, and D. G. Daniels

Simulation Modeling of Expected Thermal Generation in the Great Lakes - J. C. Sonnichsen

To assist in simulating the fate of thermal effluent release in the Great Lakes, a two-dimensional thermal transport model has been developed. The mathematical model employed is represented in differential form as follows:

$$\frac{\partial T}{\partial t} = - u\frac{\partial T}{\partial x} + v\frac{\partial T}{\partial y} + \frac{u}{\rho c} + 2\frac{\partial u}{\partial x}^2 + \frac{\partial u}{\partial y} + \frac{\partial v}{\partial x}^2 + 2\frac{\partial v}{\partial y}^2$$

$$+ \frac{K}{\rho c}\left(\frac{\partial^2 T}{\partial x^2} + \frac{\partial^2 T}{\partial y^2}\right) + \frac{1}{\rho c}\frac{\partial Q}{\partial y}$$

Replacing the derivatives with finite difference approximation reduces the differential equation into a difference equation of the form which can be employed using digital techniques.

At present the system developed does not treat the equation of motion. It has been assumed that the effluent released would have a negligible effect on the circulation pattern. Consequently, the fluid motion can be handled through a separate technique or from field studies and the resulting gross motion supplied as an input parameter to the system discussed previously. Programming of this model is now underway and tests with current data from the Great Lakes are being tested on pilot versions.

Internal Transport Relations of COLHEAT Using Reactor Effluent as a Tracer - R. T. Jaske and D. G. Daniels

A concept of mixing within river sections called the partial mixing concept has been developed for the COLHEAT digital simulation. It controls mixing between troughs within each river section by exchanging fractions of total trough

volume. By adjusting the proportions of water mixed, this concept can be used to obtain a better description of mixing in a particular stream.

The basic model divides the river transversely along velocity isopleths. In the case illustrated, a three-region model configuration was used to test the concept. In working cases of a simulation involving careful estimates of transverse distribution and highly accurate times of arrival, a single dye test or similar tracer test can be used to define the mixing coefficients among and between the sections. Additional work aimed at a basic theory is also under way.

Dye data obtained at Hanford under other or supported programs was used to attempt simulation. In the dye test, 11.7 pounds of rhodamine-B was injected into the effluent line of the 1904-B reactor. The concentration of the rhodamine-B plume was monitored as it passed the Automatic Columbia River Monitoring Station (ACRMS) some 40 miles downstream. The only data available in this test was obtained 100 feet off the west bank of the Columbia River at the ACRMS.

The studies have attempted to simulate the data obtained in the dye study described above. Using a three-trough cross section model of the Columbia River rhodamine-B concentrations were printed out every hour for each of the three troughs and after adjusting the mixing coefficient good simulation of the data was obtained. Shown below are computed concentration data obtained by Corley, (FY-1965-66 Programs) compared with computer estimates (see Figures 4.6 and 4.7).

References

1. *Nuclear Safety, Nov.-Dec. 1969, Vol. X, Number 6. pp. 513-521. DPI, Division of Technical Information, USAEC.*

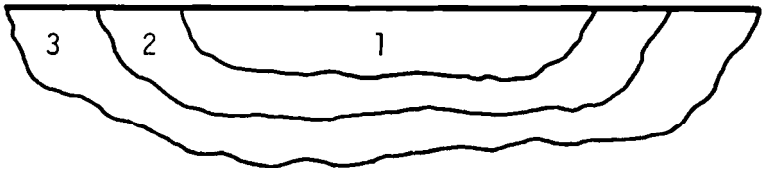

RELATIVE TROUGH VELOCITIES	RELATIVE TROUGH CROSS SECTIONAL AREA
$\upsilon_1 = 3$	$B_1 = 0.5$
$\upsilon_2 = 2$	$B_2 = 0.25$
$\upsilon_3 = 1$	$B_3 = 0.25$

FIGURE 4.6. Representative Stream Cross Sections Used in Simulation

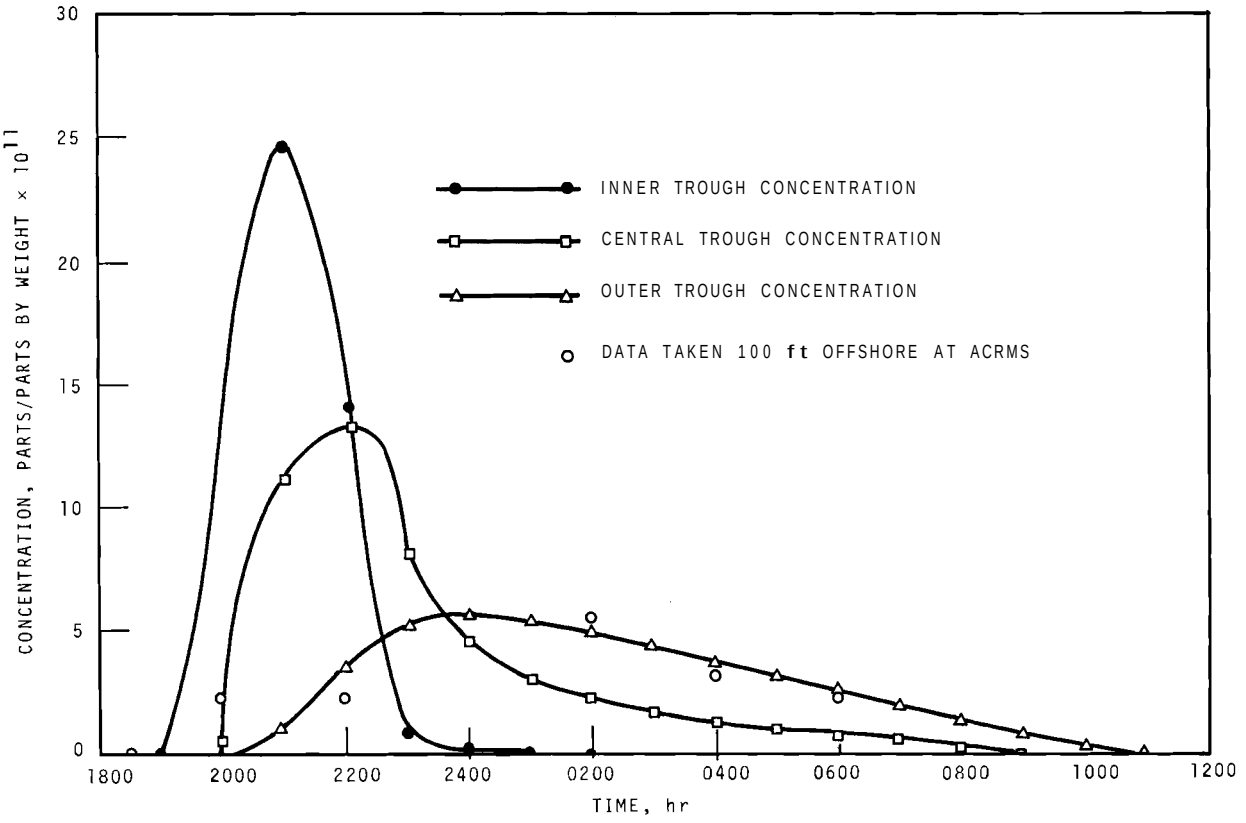

FIGURE 4.7. Concentration Curves Calculated by COLHEAT Digital Simulation Compared with Data Taken at ACRMS on April 8-9, 1965

5. FIXATION OF RADIOACTIVE RESIDUES

OVERALL STATUS OF WSEP RADIOACTIVE DEMONSTRATIONS

K. J. Schneider

Table 5.1 shows the overall status of the radioactive demonstrations in WSEP as of January 31, 1970. A total of 27 demonstrations have been completed: 6 in the pot calcination process, 11 in the phosphate glass solidification process, and 10 with the spray solidification process. Approximately 41 MCi of mixed radionuclides representing waste from about 256,000 MWd of electrical power have been converted to solids. This amount of waste represents 84 days of all the nuclear power capacity in the United States as of September 1, 1969. The total online processing time for solidification of these wastes was 62 days.

TABLE 5.1. Overall Status of WSEP Radioactive Demonstrations

	Solidification Methods			
	Pot	Spray	Phosphate Glass	Total
Runs Completed	6	10	11	27
Megacuries Solidified	4.0	17.5	19	41
Equivalent Tonnes[a] Processed	11.3	14.6	12.4	38
MWd_e **Represented by Waste[b]**	75,000	98,000	83,000	256,000
Tonne/Day Rate[a]	0.6 to 1.0	0.5 to 0.9	0.3 to 0.7	--
Maximum kW in One Pot	5.1	12.7	12.0	152[e]
Maximum W/ℓ in Pot	85	205	315[c][d]	--
Maximum Centerline Temperature in Pot, °C	940	930	780	--
Liters Solid/Tonne[a]	40 to 50	30 to 65	50 to 100	--

a. Tonne is a metric tonne (1000 kg, or 2205 lb) of original fuel.
b. Assuming 33% thermal efficiency and 20,000 MWd/tonne.
c. This value is for 6-in. diameter pots, whereas the comparable values for the pot and spray solidifiers are for 8-in. diameter pots.
d. For 8-in. diameter pots, the maximum is 195 W/ℓ.
e. Totals to date from all processes.

PHOSPHATE GLASS SOLIDIFICATION

RADIOACTIVE DEMOFJSTRATIONS - J. L. McElroy and J. N. Hartley

Phosphate Glass Solidification Run PG-11

The final phosphate glass run, PG-11, was completed during the quarter. During the eleven phosphate glass runs, a total of 19.3 MCi of radioactivity was interfused into 630 liters of solidified product. The last 12.3 MCi occurred in just the last five runs and was contained in 255 liters of product. The phosphate glass equipment has been internally flushed and stripped of external service piping so that it can be removed to allow installation of the pot calcination equipment. The equipment will be disassembled and inspected after the WSEP runs are complete.

In PG-11, a total of 813 liters of simulated LMFBR waste at 1900 liters/tonne was fed to the denitrator-evaporator in 47.5 hr. Approximately 713 liters of the feed were reduced in the melter to give 60 liters of phosphate glass product. This was equivalent to solidifying waste resulting from 0.4 tonnes of LMFBR core fuel (100,000 MWd/tonne at 200 MW/tonne) with an equivalent aging time of 1.5 years. The approximately 3,250,000 Ci of fission product activity (including 33,000 Ci of radioruthenium) interfused in the glass product produced an internal heat generation rate of 11,800 W in the 8-in. diameter, stainless steel receiver pot. This is the maximum amount of radioactive decay heat that has been contained in a receiver of phosphate glass product. The bulk density of the glass was 2.87 kg/liter. A summary of the data for Run PG-11 is given in Table 5.2.

TABLE 5.2. **Summary** Data for WSEP Phosphate Glass Run PG-11

Operational Data	
Time of Run	12/1/69 to 12/4/69
Operating Mode	A
Feed Type	LMFBR
Feed Concentration, liters/tonne	1900
Receiver Pot Diameter, in.	8
Receiver Pot Material	304L SS
Total Feed to Denitrator-Evaporator, liters	813
Total Feed to Melter, liters	713
Total Feed Time, hr	47.5
Average Feed Rate, liters/hr	17.1
Equivalent Waste to Solidifier, tonne	0.43
Equivalent Waste to Receiver Pot, tonne	0.38
Volume Reduction, feed volume product volume	11.9
Volume Reduction if Feed were at 378 liters/tonne	2.36
Filled Pot Data	
Total Curies in Feed to Receiver Pot	3,250,000
Total Curies of Ru in Feed to Solidifier	33,000
Product in Pot, liters	60
Product in Pot, liters/tonne	142
Heat Generation Rate in Pot, W	11,800 (10,700) (a)
Product Heat Rate Density, W/liter	196
Equivalent Aging Time, years	1.5(b)
$\mathcal{C}_L$ Temperature in an Air-Cooled Furnace, °C	837
$\mathcal{C}_L$ Temperature in Air, °C	827
$\mathcal{C}_L$ Temperature in Water, °C	622
Effective Thermal Conductivity of Product in an Air-Cooled Furnace, W/(m^2)(°C/m)	1.14
Effective Thermal Conductivity of Product in Air, W/(m^2)(°C/m)	1.06
Effective Thermal Conductivity of Product in Water W/(m^2)(°C/m)	0.86

a. *Lower value is based on initial pot calorimetry results.*
b. *Based on fast reactor core fuel only: 100,00 MWd/tonne at 200 MW/tonne.*

Run PG-11 was the first phosphate glass run with LMFBR waste. However, the waste as processed was not greatly different from the PW-4m waste that was demonstrated in Runs PG-8 through PG-10.* Differences were a somewhat modified fission product spectrum and the addition of selenium, tellurium, antimony, and tin, since these elements become more significant

* *BNWL-1263, 69-3.*

in the higher burnup fast reactor fuels. The feed composition for Run PG-11 is given in Table 5.3. Operation with the LMFBR waste was satisfactory from a processing standpoint and was essentially the same as with PW-4m in earlier runs. A commercial silicone antifoam was continuously added to the denitrator to prevent foaming, and dip tube plugging was prevented by venting the dip tubes on a regular basis. Both of these subjects have been discussed previously.*

A major objective of Run PG-11 was to demonstrate an alternative method of transferring feed from the denitrator to the melter using a screw-type feeder. The screw feeder had been developed and successfully tested in a pilot plant run at Brookhaven National Laboratory. It was designed so that it could be readily adapted to the WSEP denitrator-evaporator. Basically, the screw feeder is an auger within a tight-fitting pipe that runs from the bottom of the denitrator to a point above the denitrator where concentrate overflows through a line to the melter. Although the screw feeder showed promising results during the first 7 hr of feeding, it subsequently failed and could not be made to operate again. During the 7 hr that it was used, the denitrator concentrate entered the melter at a stable rate and produced temperature patterns in the melter that were considerably more stable than was possible with the airlift. After approximately 6 hr of feeding, attempts were made to increase the feed rate to the melter by increasing the speed of the screw. However, increasing the air pressure to the air motor had very little effect. Although the motor and screw were capable of speeds in excess of 800 rpm and had been to 650 rpm early in the run, it would not exceed approximately 550 rpm, and the motor was

---

* *BNWL-1263, 69-3.*

TABLE 5.3. **LMFBR Feed Composition for Phosphate Glass Run PG-11**

Component	Concentration, M[a]
H^+	---
Fe^{+3}	0.16
Cr^{+3}	0.046
Ni^{+2}	0.023
Al^{+3}	---
Na^+	0.10
PO_4^{-3}	0.06
NO_3^-	~4.75
SO_4^{-2}	---
MoO_4^{-2} + Tc as MoO_4^{-2}	0.30
Sr^{+2}	0.04
Ba^{+2}	0.068
Rb^+ + Cs^+ (added K^+)	0.229
$(Y + RE)^{+3}$ + La as $(Y + RE)^{+3}$	0.528
ZrO^{+2} + Nb as ZrO^{+2}	0.222
Ru^{+4}	0.0061
Ru^{+4} (added Fe^{+3})	0.22
Rh^{+2} (added Co^{+2})	0.06
Pd^{+2} (added Ni^{+2})	0.16
Ag^{+2} (added Cu^{+2})	0.019
Cd^{+2} (added Cu^{+2})	0.010
TeO_4^{-3} (added SO_4^{-3})	0.039
SeO_4^{-3}	0.005
Sn^{+4} + In^{+3} as Sn^{+4}	0.011
Sb^{+3}	0.003
Additive to Feed	
Na^+	2.90
Fe^{+3}(b)	0.14
Al^{+3}(b)	0.70
PO_4^{-3}	10.60
$\Sigma M^+/P$	1.03

a. *Molarities are at 378 liters/tonne.*

b. *Nominal Fe additive is 0.84M, however excess Al in the waste from the processing plant is used as a suistitute for Fe.*

dragging badly at the time it stopped rotating. Following the run the screw feeder unit was removed from the denitrator and the air motor was disconnected from the screw. Although the screw would rotate freely, the air motor could not be turned. The cause of the failure of the motor is not known although radiation may have been a contributor. The run was successfully completed without delay by using the airlift unit which had been kept in a standby condition.

Another problem encountered during the run was that the melt falling from the melter overflow weir into the 600 °C receiver pot struck the pot thermowells near the top of the pot and formed stalagmites in the top of the pot. The melt draining from the melter through the freeze-drain valve also occasionally struck near the top of the pot. Consequently, the majority of the run was performed by batch draining the melter and deflecting the melt stream from the freezedrain valve to the center of the receiver using a flat piece of stainless steel. This was the first phosphate glass run where most of the melt entered the pot via a batch filling technique, and the method appears to be satisfactory. The cause of the melt falling off-center from both of the melter tubes is not definitely known. However, it appears that the entire melter furnace and melter became tipped sideways by approximately 2 degrees sometime between Runs PG-10 and PG-11. This was the first time since Run PG-3* that a problem has been encountered with melt satisfactorily filling the receiver pot. The primary reason for filling problems during Run PG-3 was that the receiver temperature was only 300 °C and the entering melt from the weir would not slump and instead stalagmites were formed.

---

* *BNWL-771, 67-4.*

With the high internal heat generation rate of 11,800 W the maximum centerline temperature of the phosphate glass with the receiver in the air-cooled furnace was only 843 °C. This is typical of the way the phosphate glass behaves, since the core becomes slightly molten at temperatures as low as 600 °C, and the result in an increase in the effective thermal conductivity of the product. The effective thermal conductivity in the air-cooled furnace for this run was 1.14 $W/(m^2)(°C/m)$. For runs where the core was not molten, the effective thermal conductivity averaged approximately 1.0 $W/(m^2)(°C/m)$. With the pot removed from the furnace and placed in water storage, the pot centerline temperature decreased to 622 °C, and for this case with the product more nearly completely solidified, the effective thermal conductivity was 0.86 $W/(m^2)(°C/m)$.

During Run PG-11 a Mode A operation as illustrated in Figure 5.1 was used. The radionuclide distribution for Run PG-11 is summarized in Table 5.4. Data are included for Runs PG-9 and PG-10 which were discussed in the previous quarterly report. During Run PG-11, a total of 0.5% of the radioruthenium and 0.001% of the nonvolatiles (represented by CePr-144) that were fed to the denitrator were volatilized and entrained from the denitrator and accumulated in the auxiliary evaporator. An equivalent of 6.6% of the radioruthenium and 0.04% of the nonvolatile~in the feed to the denitrator were volatilized and entrained from the melter and accumulated in the melter condensate receiver as shown in Figure 5.2.

The auxiliary evaporator operated on about 5M nitric acid with an overhead acidity ranging from about 0.1 to 0.5M nitric acid. The cumulative decontamination factor (DF) for radioruthenium across the auxiliary evaporator was 48. Instantaneous DF's were typically about 10^3. Comparable cumulative DF for nonvolatiles was 1.9×10^4 while instantaneous DF's

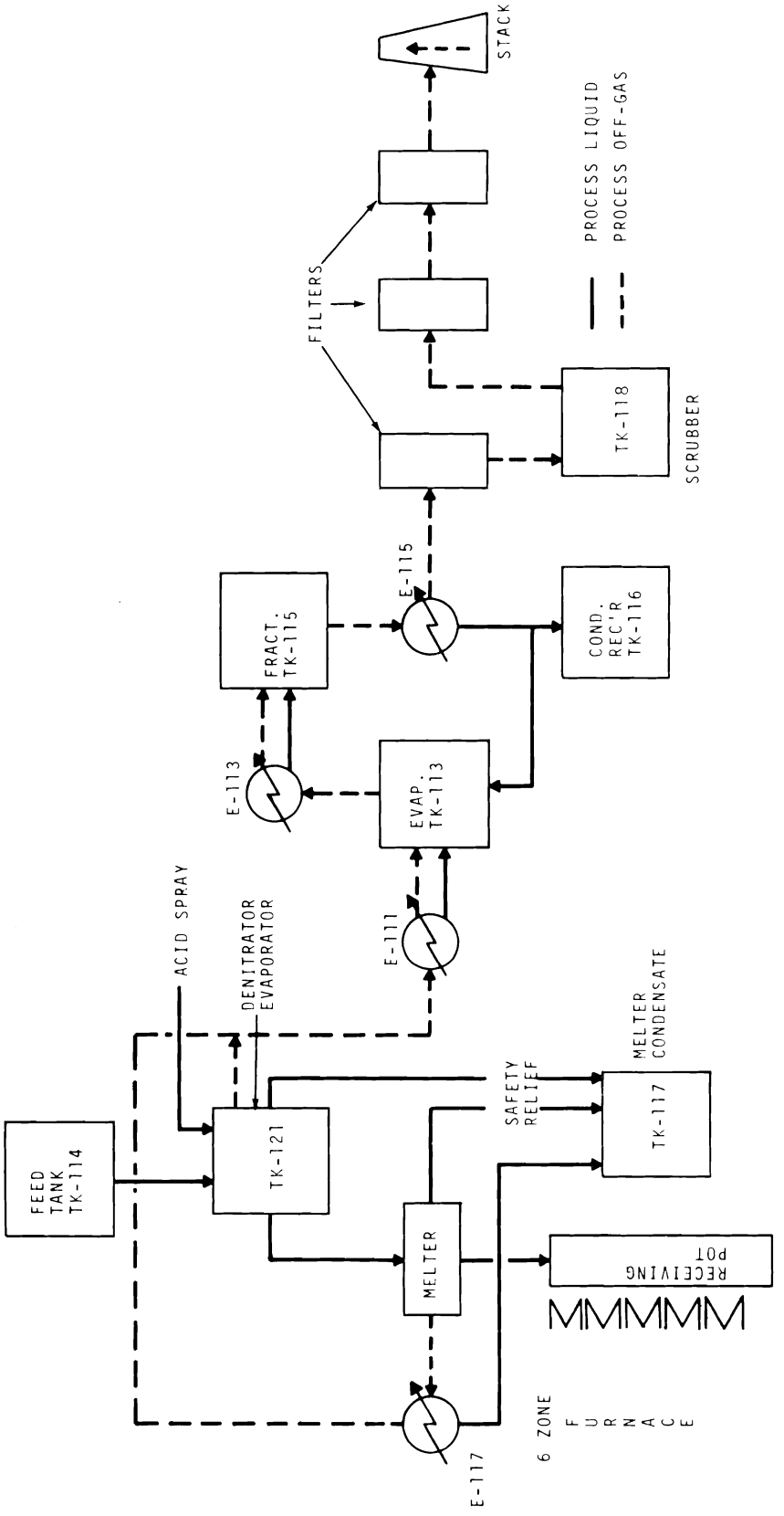

FIGURE 5.1 Mode A Arrangement for PG-11

TABLE 5.4. Radionuclide Distribution in WSEP Auxiliaries for Runs PG-9, PG-10, and PG-11 (Mode A Operation)

	Fraction of Equivalent Feed Radioactivity					
	PG-9		PG-10		PG-11	
	Ru-106	CePr-144	Ru-106[a]	CePr-144	Ru-106	CePr-144
Melter Condensate (TK-117)	4.7×10^{-2}	5.4×10^{-4}	NA	3.1×10^{-4}	6.6×10^{-2}	4.1×10^{-4}
Evaporator Bottoms (TK-113)	8.8×10^{-3}	6.3×10^{-4}	NA	3.6×10^{-4}	4.8×10^{-3}[b]	1.3×10^{-5}[b]
Fractionator Bottoms (TK-115)	7.6×10^{-5}	NA	NA	4.9×10^{-7}	5.2×10^{-4}	1.3×10^{-6}
Fractionator Distillate (TK-116)	6.5×10^{-7}	NA	NA	3.2×10^{-9}	2.2×10^{-7}	2.6×10^{-9}
Scrubber Bottoms (TK-118)	7.1×10^{-9}	NDG	NA	NDG	6.3×10^{-7}	NDG
Offgas from Scrubber	1.8×10^{-9}	$1.4 \quad 10^{-10}$	NA	3.7×10^{-11}	2×10^{-10}	$<2 \times 10^{-13}$
Offgas to Stack	$<3 \times 10^{-10}$	1.2×10^{-13}	NA	5.2×10^{-14}	$<9 \times 10^{-10}$	$<2.3 \times 10^{-13}$
Ratio (Fract. Dist.) Activity to 10CFR20	1600	3[illegible]00	NA	2150	2200	1500
Ratio (Final Offgas) Activity to 10CFR20	140	14	140	14	150	10
Ratio (Offgas to Stack) Activity to 10CFR20	$<4 \times 10^{-4}$	1.4×10^{-4}	$<4 \times 10^{-4}$	1.4×10^{-4}	$<4 \times 10^{-4}$	$<7.7 \times 10^{-4}$

NA - Not Available NDG - No detectable gain in radoactivity

a. *There was no radioactive ruthenium in feed to solidifier*

b. *Based on denitrator condenser condensate stream samples*

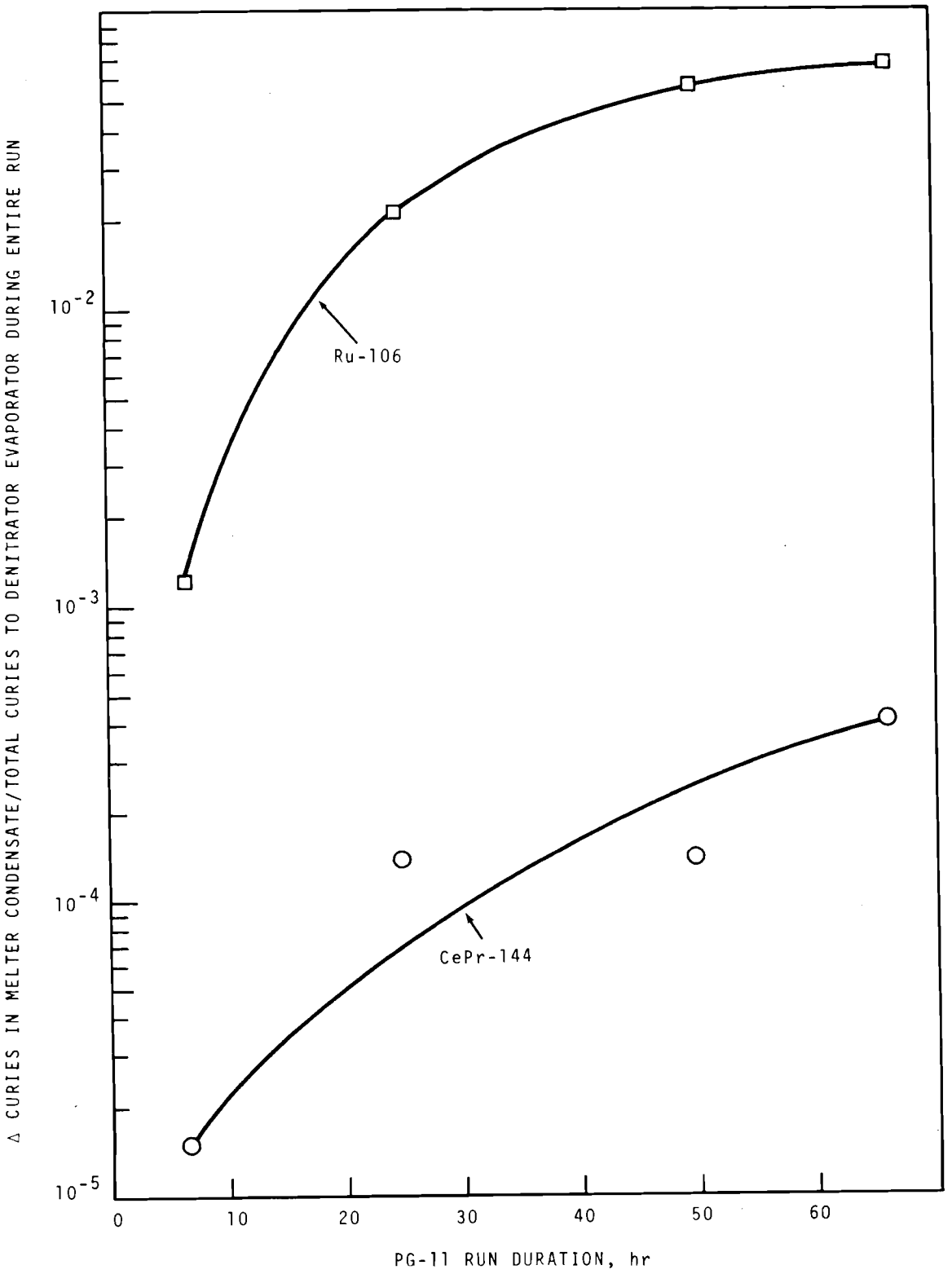

FIGURE 5.2. Radionuclide Accumulation in Melter Condensate

were typically about 10^5. The fraction of equivalent feed radioactivity that accumulated in the acid fractionator was 5.2×10^{-4} for radioruthenium and 1.3×10^{-6} for nonvolatiles.

Most of the radionuclides that escaped the acid fractionator were caught in the fractionator distillate. About 80% of the distillate was recycled to the evaporator as strip water while about 20% was accumulated in the distillate receiver. During Run PG-11 the fraction of equivalent feed radioactivity that accumulated in the fractionator distillate receiver was 2.2×10^{-7} for radioruthenium and 2.6×10^{-9} for nonvolatiles. The concentration of radionuclides in the accumulated fractionator distillate was above 10CFR20 release limits by factors of 2200 for radioruthenium and 1500 for CePr-144.

Data obtained from gas samples taken during Run PG-11 are summarized in Table 5.5. The denitrator condenser off-gas contained an average of 2.2×10^{-2} $\mu Ci/cm^3$ Ru-106 and 3.7×10^{-4} $\mu Ci/cm^3$ CePr-144. The radionuclides leaving with the evaporator condenser off-gas remained about the same whether feed was on to the solidifier or off and averaged about 2.1×10^{-5} $\mu Ci/cm^3$ of Ru-106 and 1.6×10^{-4} $\mu Ci/cm^3$ of CePr-144.

The radionuclides which are not absorbed in the fractionator distillate and leave in the fractionator condenser off-gas averaged about 9.6×10^{-7} $\mu Ci/cm^3$ of Ru-106 and 1.7×10^{-5} $\mu Ci/cm^3$ of CePr-144.

The fractionator condenser off-gas is filtered by a high efficiency filter before entering the scrubber. The only radionuclide detected in the process off-gas leaving the filter was 1.9×10^{-8} $\mu Ci/cm^3$ of CePr-144. This value

TABLE 5.5. Radionuclides in the Process Off-Gas

Run No.	Process Condenser (E-111) Offgas, μCi/cm³(a)			Evaporator Condenser (E-113) Offgas, μCi/cm³(a)			Fractionator Condenser (E-115) Offgas, μCi/cm³(a)		
	Ru-106	Cs-137	CePr-144	Ru-106	Cs-137	CePr-144	Ru-106	Cs-137	CePr-144
9	2.9×10^{-3}	3.2×10^{-5}	1.0×10^{-4}	6.0×10^{-6}	2.5×10^{-6}	2.1×10^{-5}	9×10^{-8}	6.7×10^{-8}	1.4×10^{-5}
10	1.5×10^{-4}(b)	8.9×10^{-5}	1.5×10^{-3}	4.9×10^{-6}	3.3×10^{-7}	1.6×10^{-5}	9.3×10^{-8}	8.3×10^{-8}	3.8×10^{-5}
11	2.2×10^{-2}	1.0×10^{-4}	3.7×10^{-4}	2.1×10^{-5}	8.2×10^{-7}	1.6×10^{-4}	9.6×10^{-7}	1.1×10^{-7}	1.7×10^{-5}

	Offgas to Scrubber From Filter, μCi/cm³			Final Process Offgas From Scrubber, μCi/cm³(a)		
	Ru-106	Cs-137	CePr-144	Ru-106	Cs-137	CePr-144
9	2.2×10^{-8}	3.4×10^{-8}	2.2×10^{-7}	2.7×10^{-8}	1×10^{-8}	5.5×10^{-9}
10	5.6×10^{-8}	3.7×10^{-8}	4.6×10^{-8}	2.4×10^{-8}	8.2×10^{-9}	5.7×10^{-9}
11	---	---	1.9×10^{-8}	3×10^{-8}	5×10^{-8}	3.9×10^{-9}

a. Average values for entire run

b. No ruthenium in feed to solidifi

indicated a particulate DF across the filter of about 4×10^3 for CePr-144 indicating a filtering efficiency of 99.98%. With this small amount of nonvolatiles entering the scrubber there was no detectable gain of nonvolatiles in the scrubber. However, the fraction of equivalent radio-ruthenium fed to the solidifier which accumulated in the scrubber was 6.3×10^{-7}.

The final process off-gas exiting the scrubber contained an average of about 3×10^{-8} $\mu Ci/cm^3$ Ru-106 and 3.9×10^{-11} $\mu Ci/cm^3$ CePr-144. These values were greater than 10CFR20 release limits by factors of 150 and 10, respectively and agreed with previous runs. Before the final process off-gases are released to the environment, they are combined, with the building ventilation and filtered before finally entering the stack for release to the atmosphere. At this point radionuclide concentrations are well below 10CFR20 release limits.

SPRAY SOLIDIFICATION

LABORATORY STUDIES

Corrosion Studies - R. F. Maness

Specimens of 77Cr-23Al_2O_3 (deposited by flame saraying) were exposed in alumina crucibles to PW-4m melt at 1000 and at 1050 °C for 100 hr and at 1100 °C for 50 hr. Corrosion rates, as determined by weight loss, were 0.14, 0.42, and 1.1 in./year, respectively. A similar test specimen exposed to PW-2 melt at 1100 °C for 50 hr corroded at a rate of 0.42 in./year.

ENGINEERING STUDIES

Fast Reactor Waste Solidification Tests J. D. Moore

Two nonradioactive test runs with the developmental spray solidifier were made using simulated fast reactor waste as solidifier feed. The fast reactor waste, tested previously in DSC-36, contains fission products characteristic of fuel irradiated at 200 MW/tonne with an exposure of 100,000 MWd/tonne. This waste will be tested in the WSEP radioactive demonstration.

DSC-37 was run to determine the extent of volatilization of fission product selenium, tellurium, antimony, and tin from the waste (see Table 5.6 for detailed composition). In addition, it was desired to confirm the unexpectedly low (<2%) ruthenium volatilization in the same waste which was observed in DSC-36. It was suspected that the old $Ru(NO_3)_3$ stock solution used in feed makeup had converted to nonvolatile RuO_2, since a large volume of solid material had precipitated in the stock solution. The run was conducted in two parts with feed containing ruthenium from a new stock solution used in the first half and feed containing ruthenium from the old stock (as in DSC-36) used in the second half. Ten times the nominal waste concentrations of selenium and antimony (considered to be potentially the most volatile of the fission products next to ruthenium) were spiked in the feed to increase the accuracy of the analyses for volatilization of these elements.

Ruthenium release was higher in both halves of the run than was observed in DSC-36. Eleven percent was released in the first half, and 17% was released in the second half.

TABLE 5.6. Feed Compositions for Developmental Spray Solidifier Runs
Basis: 378 liters/tonne

Run No. / Waste Type	DSC-37 FR	DSC-38 PW-1	DSC-39 FR
Chemicals			
Fe^{+3}	0.372M[a]	0.9556[b]	0.0[c]
Cr^{+3}	0.046	0.012	0.046
Ni^{+2}	0.183	0.0222	0.183
Na^{+}	0.822[d]	0.178[e]	0.682[d]
Al		0.001	0.40[f]
PO_4^{-3}	0.06	0.003	0.06
SiO_3^{-2}		0.010	
NO_3^{-}	4.42	3.6	4.694
H^{+}	0.18	0.022	0.18
OH	0.1		0.0
Fission Products			
MoO_4^{-2}	0.30	0.079	0.30
Sr^{+2}	0.040	0.0155	0.040
Ba^{+2}	0.068	0.0195	0.068
Rb + Cs (used K^{+})	0.229	0.042	0.229
(Y + RE)	0.528	0.12	3.634[g]
ZrO^{+2}	0.222	0.065	0.222
Ru^{+4}	0.008[h]	0.0064[i]	0.008[h]
Rh (used Co^{+2})	0.060	0.0074	0.060
Ag^{+}	0.019	0.0008	0.11
Cd^{+2}	0.010	0.0008	0.010
Te^{+4}	0.034	0.0064 (used SO_4^{-2})	0.034
Pd (used Ni^{+2}, included above)	0.16	0.017	0.16
Tc (used MoO_4^{-2}, included above)	0.06	0.014	0.06
Sn^{+4}	0.011		0.011
Sb^{+3}	0.03[j]		0.018[j]
SeO_4^{-2}	0.05[k]		0.05[k]

TABLE 5.6. (continued)

Run No. Waste Type	DSC-37 FR	DSC-38 PW-1	DSC-39 FR
Additives			
HNO_3		2.55	
$Fe(NO_3)_3$	2.17		2.142
NaOH	2.8	0.65	2.8
$NaPO_3$		0.35	
H_3PO_4	5.66	1.34	5.82

a. *Nominal ER Fe concentration is 0.16M. Excess is Ru substitute,*
b. *Nominal PW-I Fe concentration is 0.93M. Excess is Ru substitute.*
c. *Nominal Fe concentration is 0.16M. Al is substituted for Fe.*
d. *Nominal FR Na concentration is 0.1M. Excess Na is from using $Na_2MoO_4 \cdot 2H_2O$ for Mo addition, Na_2SnO_3 for Sn additton, and Na_2SeO_4 for Se addition.*
e. *Nominal PW-1 Na concentration is 0.138M. Excess Na is from using $Na_2MoO_4 \cdot 2H_2O$ for Mo addition.*
f. *No Al normally exists in FR waste. Al is used here for Fe and Ru substitute.*
g. *Nominal RE concentration is 0.528M. Excess is added to compensate for possible excess necessary to achieve desired feed heat content in WSEP radioactive demonstrations.*
h. *Nominal FR Ru concentration is 0.22M.*
i. *Nominal PW-1 Ru concentration is 0.032M.*
j. *Nominal FR Sb concentration is 0.003M. Excess was added to better determine Sb volatilization.*
k. *Nominal FR Se concentration is 0.005M. Excess was added to better determine Se volatilization.*

The results of this run agree more closely with the results of most previous runs with high acid, phosphate-containing feeds. The reason for low volatilization in DSC-36 has not been determined.

Selenium volatilization in the first and second halves of the run were 20 and 29%, respectively. Antimony, tin, and tellurium were less than 1% volatile.

As in DSC-36, the calciner and melter ran smoothly. The melter furnace temperature was lowered to 1150 °C compared to 1200 °C in DSC-36. The lower temperature decreased the amount of foaming in the melter but did not decrease the ease with which melt was drained from the melter freeze valve. The onerating conditions and results of DSC-37, 38, and 39 are summarized in Table 5.7.

In Run DSC-39, the effects on melt viscosity of aluminum and rare earth additions to the fast reactor waste were studied. Although not present in the nominal fast reactor waste composition, aluminum is present in the 1WW used for radioactive waste makeup in the WSEP. In addition, an estimated 20% excess concentration of rare earths may be added as radiocerium solution in order to get the desired radioactive heat generation rate in the WSEP spray solidifier feed.

In DSC-39, aluminum (0.4M) was substituted for equimolar iron, and a 20% excess of rare earths was added to the fast reactor waste. Sodium and phosphoric acid were added to give a M^+/P of 2.5 (see Table 5.6). At a concentration of 992 liters/tonne, the feed flow to the spray solidifier was stable.

TABLE 5.7. Summary of Developmental Spray Solidifier Runs

Run No.	DSC-37		DSC-38	DSC-39
	Part 1	Part 2		
Feed Type	FR		PW-1	FR
Feed Concentration, liters/tonne	976	992	458	992
Additives	Fe,Na,PO_4		Na,PO_4, PO_3	Na,Fe,PO_4,Al
Feed Total Acidity, M H^+ at 378 liters/tonne	12.6	11.0	6.5	12.3
Feed Consumed, liters	103.8	95.5	106.2	54.8
Average Feed Rate, liters/hr	14.8	15.9	16.1	15.2
Calciner Furnace Temperature, °C	700		700	700
Calciner Vacuum, in. of water	2-8		8	8
Melter Furnace Temperature, °C	1150		1150	1150
Atomizing Gas	Air		Air	Air
Atomizing Gas Flow, scfm	6.5	6.4	6.4	6.6
Filter Blowback Pressure, psig	30		30-50	30
Filter Pressure Drop, End of Run, in. of water	4.5		6.5	5.5
Melt Storage Pot Temperature, °C	800		800	unheated
Product Collected, kg	65		24.5	20.5
Product Density, g/cm^3	3.5		3.3	3.3
Product Concentration, liter/tonne	92		32	112
Ruthenium Volatilized, % of total feed ruthenium	11	17	34	23

The calcine melted easily with slight foaming with the melter furnace temperature at 1150 °C. Melt dripped. from the weir in foamy drops for the last 2 hr of the 3.6 hr run. At the end of the run, melt was emptied through the freeze valve at a discharge rate of 40 to 50 liters/hr. The melt appeared to be slightly more viscous than the aluminum and rare earth-deficient melts tested in DSC-36 and 37, but was still considerably less viscous than the PW-4m melt successfully tested in the WSEP spray solidifier. A waste of this composition should offer no operating prcblems in the WSEP spray sclidifier.

Fission product release from the solidifier was comparable to that observed in DSC-37. Ruthenium was 23% volatile, and antimony, tin, and tellurium were less than 2% volatile. Selenium release at 40% was somewhat greater than the 20 to 29% observed in DSC-37.

Ruthenium Adsorption Tests - J. D. Moore

The effectiveness of ruthenium removal from the spray solidifier off-gas by adsorption on ferric oxide was tested in DSC-38 and 39. The ruthenium adsorber consisted of a bed of 6-10 mesh silica gel thinly coated with ferric oxide packed in a 4-in. pipe. The total bed volume was 11 liters but the void space volume was not measured. The adsorber was connected to the spray solidifier off-gas line between the calciner filters and the condenser and about 4% (1.5 ft^3/min) of the total off-gas flow was routed through the adsorber. The adsorber was heated to maintain the internal hed temperature between 300 to 425 °C. The liquid collected from condensing the adsorber effluent gas was collected and compared for ruthenium concentration with normal off-gas condensate from the solidifier.

During the first hour that the adsorber was used, 94% of the ruthenium was removed from the off-gas stream. After 4 hr, however, adsorption had decreased to 64%. In 10 hr, including 4 hr in DSC-39, the ruthenium removal had decreased to 35%. About 0.9 g of ruthenium had accumulated in the adsorber over this period.

Based on these results, this method of ruthenium removal from the solidifier off-gas would not be adequate. It may prove to be useful, however, in removing ruthenium from the effluent gas from the WSEP waste evaporator in which the ruthenium evolution rate is less than 1% of that from the spray solidifier.

WSEP AUXILIARY STUDIES

INTEGRATION OF A WASTE SOLIDIFICATION SYSTEM WITH A FUEL REPROCESSING PLANT

Recycle of WSEP Recovered Acid and Water - J. N. Hartley and G. L. Richardson

In the integration of a waste solidification system with a fuel reprocessing plant, it is desirable that secondary waste streams from solidification are acceptable for reuse within the fuel reprocessing plant or for final release to the environment. A conceptual flowsheet has been prepared* that employs essentially complete recycle of the secondary waste streams (recovered nitric acid and water) to the head-end (dissolution and first sclvent extraction cycle of the fuel reprocessing plant) as makeup water and acid. In this flowsheet (see Figure 5.3) 80% of the recovered acid is used as dissolver acid

* *BNWL-1186.*

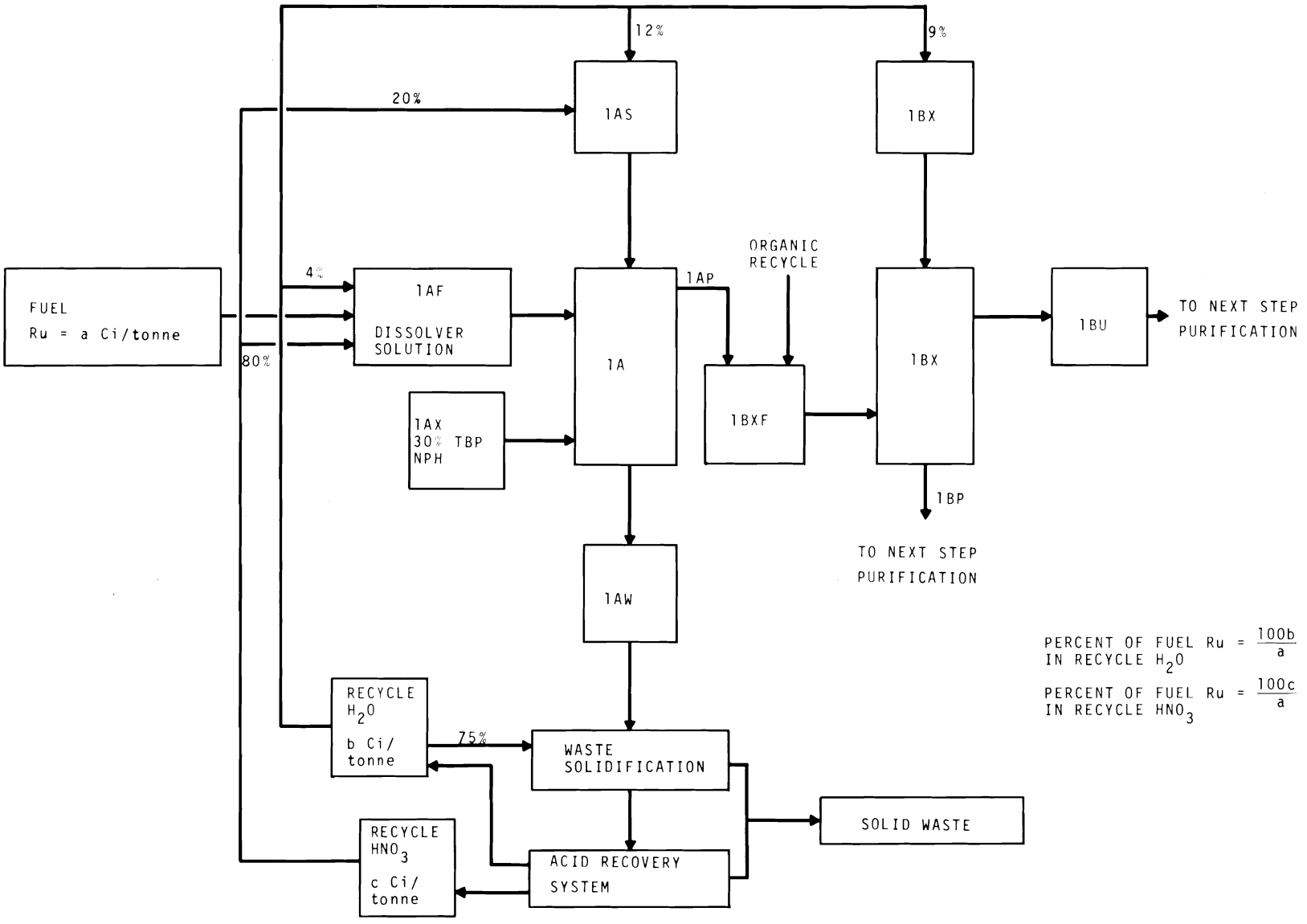

FIGURE 5.3. Integration of Waste Solidification with Conventional Purex Fuel Reprocessing Plant

and to adjust the 1AF stream (Purex 1A Column feed stream) composition, and 20% is used in the 1AS stream (1A Column scrub). Likewise, about 75% of the recovered water is used as nitric acid stripwater for high level waste concentrator, 4% is used to prepare the 1AF stream, 12% is used in the 1AS stream, and the remaining 9% is used to prepare the 1BX stream (1BX Column plutonium strip).

The main contaminant in the recovered acid and water is radioruthenium. In order to reuse the recovered acid and water, the effect of recyling the radioruthenium must be determined. The calculated effect of various levels of radioruthenium contamination in recycled solidification effluent streams on the first solvent extraction cycle decontamination performance is illustrated in Figure 5.4. This shows that the plutonium decontamination factor (DF) from the 1AF to the 1BP is seriously lowered by a ruthenium content in the recycled acid as low as 0.01% of that in high level waste (HLW) resulting from the reprocessing of a power reactor fuel with an exposure of 45,000 MWd/tonne at 30 MW/tonne. (The 0.01% is equivalent to a ruthenium DF from the HLW to the recovered acid of 10^4.) The uranium product stream can tolerate about 10-fold more ruthenium in the recycled streams before its DF suffers correspondingly. To show the effect of actual WSEP effluents, the range and average fractions of fuel ruthenium in the recovered acid and water are also shown on Figure 5.4.

The effect of ruthenium in the recycled water at the ruthenium levels expected is relatively minor. This is illustrated by the family of curves for various ratios of total ruthenium content in the recovered nitric acid to that in the recovered water, (N/W) (in effect, the corresponding ratio of DF's obtained during their recovery from HLW).

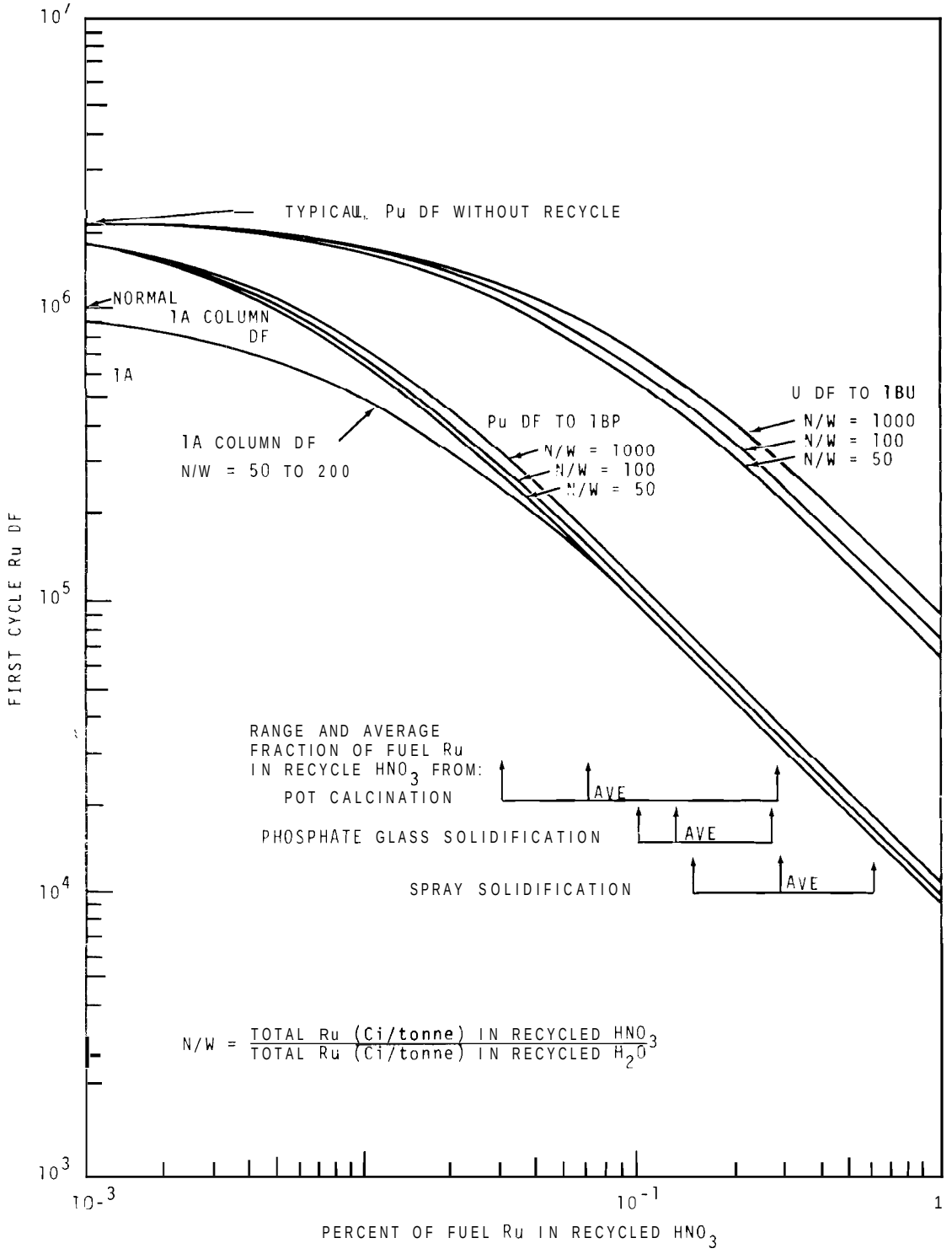

FIGURE 5.4. **Effect of Ruthenium in Recycled Acid and Water on First Solvent Extraction Cycle Decontamination Factor**

The data were calculated on the following basis:

1) All recycled ruthenium in the solvent extraction feed was assumed to behave normally and to yield ruthenium DF's of 1×10^6 in the 1A column and 2×10^6 for both the uranium and plutonium first cycle products.

   The ruthenium entering from the recycle streams via the 1AS and 1BX streams was assumed to distribute normally to the solvent products stream leaving the 1A and 1BX columns, respectively. That is, the ruthenium in the solvent product stream was essentially in equilibrium with the ruthenium concentration in the 1AS and 1BX. Distribution ratios ($\underline{F}_a^o$) of 0.008 and 0.02 were chosen for the 1AS and 1BX, respectively.

3) About 90% of the recycled ruthenium extracted from the 1AS was assumed to strip with the plutonium product in the 1BX column. That is, about 10% of the extracted ruthenium was assumed to be a difficult-to-strip species.

The effect of recycled ruthenium on the DF's is highly dependent on the distribution ratios of the ruthenium from the 1AS stream to the 1AP (solvent product) stream. Ruthenium exists in nitric acid solutions as a variety of nitrosyl, nitro, and nitrato complexes. Each of these has a characteristic distribution ratio between aqueous and solvent phases. Usually the average distribution ratio is quite low (0.001 to 0.01), but as the solvent extract is scrubbed, the less extractable species are removed thereby leaving the most highly extractable species in the solvent. (It is not uncommon to find ruthenium distribution ratios greater than 1 between well scrubbed solvent product and a dilute HNO_3 scrub solution.) The spectrum of ruthenium species nresent in an

aqueous phase is dependent on the prior treatment and the aging time between treatment and use. It is important that laboratory studies be made to determine the actual ruthenium distribution ratios for NSEP recycled acid and water effluent streams.

FISSION PRODUCT VOLATILITY STUDIES

Volatility of LMFBR Waste Fission Products - M. R. Schwab

The LMFBR waste shown in Table 5.3 contains significant quantities of antimony, selenium, tellurium, and tin, each of which is potentially volatile and could present off-gas decontamination problems similar to the problems with ruthenium. As shown in Table 5.8, the total decontamination factor (DF) (feed to aqueous effluent) required for the radionuclides of antimony, selenium, tellurium, and tin are generally much less that the DF's required for cerium, cesium, and ruthenium in the LMFBR waste. However, the magnitudes of the total DF's required for these "new" volatile radionuclides become significant if these radionuclides were to behave like ruthenium during the solidification of the LMFBR waste. Consequently, a study was made to determine the relative volatility of these four radionuclides during the solidification of the LMFBR waste in the WSEP program. The study was directed towards the analysis of the primary solidifier condensates from the spray solidifier and the phosphate glass solidifier. Condensate samples were obtained from each of the two nonradioactive phosphate glass solidification runs (EM-13 and EM-14) performed at the Brookhaven National Laboratory and from two nonradioactive spray solidification runs (DSC-36 and DSC-37) performed at the Pacific Northwest Laboratory. Each condensate sample was analyzed by atomic absorption techniques for antimony, molybdenum, ruthenium, selenium, strontium, tellurium,

TABLE 5.8. Maximum DF's Required for Selected Radionuclides in LMFBR Wastes Processed in WSEP

Radionuclide	Half Life	Radioactivity[a] in Waste at 378 liter/tonne, Ci/liter	10CFR20[b] Limit, Ci/liter	Maximum DF[c] Required at 378 liter/tonne (H_2O)
^{79}Se	6.5^{4}y[d]	3.9^{-3}	3^{-7}[e]	1.3^{4}
^{90}Sr	28y	2.9^{-1}	3^{-10}	
^{103}Ru	40d	1.1^{3}	8^{-8}	1.3^{10}
^{106}Ru	1.0y	8.4^{3}	1^{-8}	8.5^{11}
^{123m}Sn	129d	1.6^{2}	2^{-8} [f]	8.0^{10}
^{126}Sn	2^{5}y	1.1^{2}	2^{-8} [f]	5.3^{5}
^{125}Sb	2.7y	1.8^{2}	1^{-7}	1.8^{9}
^{125m}Te	58d	39	1^{-7}	3.9^{8}
^{127m}Te	105d	84	5^{-8}	1.7^{9}
^{129m}Te	33d	30	2^{-8}	1.5^{9}
^{134}Cs	2.1y	5.3^{2}	9^{-7}	5.7^{8}
^{137}Cs	30y	8.8^{2}	2^{-8}	4.4^{10}
^{144}Ce	285d	8.1^{3}	1^{-8}	8.1^{11}

a. Fission products at 180 days cooling (See BNWL-889).

b. Code of Federal Regulations: Title 10, Part 20, Appendix B, Table 2, Column 2.

c. Based on total feed to aqueous effluent.

d. $6.5^{4} = 6.5 \times 10^{4}$.

e. Based on limits for ^{75}Se; no data available for ^{79}Se.

f. Based on limits for ^{125}Sn; no data available for ^{123m}Sn or ^{126m}Sn

and tin. Based on the analysis of these condensate samples, the nominal range expected for the fraction of each of these chemicals in the LMFBR waste which will accumulate in a solidifier condensate is presented in Table 5.9. The data in Table 5.9 are limited to a range due to the limits of detection for the nonvolatile chemicals (i.e., those which behaved similar to cerium and strontium) and due to the observed variations in the concentrations for the volatile radionuclides. While the fission product molybdenum is not radioactive, its fractional distribution in the condensates is included as a convenience since the atomic absorption method is particularly sensitive for molybdenum. An atomic absorption technique for cerium was not available, but strontium was readily detectable and was used, therefore, to compare the LMFBR condensate data with the typical WSEP data obtained from radioactive demonstrations with the PW-1 and PW-2 waste flowsheets.

Based on the data in Table 5.9, it was concluded that the fission products of tin and antimony are not volatile during waste solidification. Based on the data of Table 5.9, the only radionuclides in the LMFBR waste which are expected to be significantly volatile are ruthenium, tellurium, and selenium. However, since the total DF (feed to aqueous effluent) required for selenium is only about 10^4, the decontamination requirements for the solidification of LMFBR wastes will probably leave tellurium and ruthenium as the fission products which will be of primary concern during waste solidification.

TABLE 5.9. Nominal Ranges for Fraction of Principle LMFBR Radionuclides Expected in WSEP Solidifier Condensates[a]

Radionuclide	Phosphate Glass Solidifier[b] Denitrator-Evaporator Condensate	Phosphate Glass Solidifier[b] Melter Condensate	Spray Solidifier Solidifier Condensate
Mo	1^{-5} to 1^{-4}[e]	1^{-3} to 1^{-2}	1^{-4} to 1^{-3}
Sb	1^{-4} to 1^{-3}	1^{-3} to 1^{-2}	1^{-4} to 1^{-3}
Sn	1^{-4} to 1^{-3}	1^{-3} to 1^{-2}	1^{-4} to 1^{-3}
Sr	1^{-5} to 1^{-4}	2^{-4} to 2^{-3}	1^{-4} to 1^{-3}
Te	1^{-4} to 1^{-3}	1^{-2} to 1^{-1}	1^{-3} to 5^{-3}
Se	5^{-4} to 5^{-3}	5^{-1} to 1.0	1^{-1} to 5^{-1}
Ru	NA[f]	NA	1^{-1} to 5^{-1}
Ce	1^{-4} to 1^{-3}	1^{-3} to 5^{-3}	5^{-4} to 1^{-3}
Sr	1^{-4} to 1^{-3}	1^{-3} to 5^{-3}	5^{-4} to 1^{-3}
Ru	1^{-3} to 1^{-2}	5^{-2} to 1^{-1}	4^{-1} to 8^{-1}

(d) Nominal values observed for the first six radioactive waste solidification demonstrations for each of these solidifiers. No condensates samples were available from a pot calcination demonstration of an LMFBR flowsheet.

a. See Table 3 for LMFBR waste composition.

b. Based on analyses of nonradioactive condensates from runs EM-13 and EM-14 performed at the Brookhaven National Laboratories.

c. Based on analyses of nonradioactive condensates from runs DSC-36 and DSC-37 performed at the Pacific Northwest Laboratories.

e. $1^{-4} = 1 \times 10^{-4}$.

f. Not available. Iron was substituted for ruthanium in the simulated LMFBR waste.

EVALUATION OF SOLIDIFIED WASTE PRODUCTS

PRODUCT MEASUREMENTS, TESTING, AND STORAGE

Solids Storage Engineering Test Facility (SSETF) - R. J. Thompson

Table 5.10 shows the solidified waste containers that have been transferred to SSETF for environmental testing. WSEP Runs SS-4 and PG-6 are stored in water while PC-6 and SS-8 are stored in air. The maximum waste container centerline and wall temperature and the maximum environmental test pod temperature are reported in Table 5.10. There is some indication from the temperature profile data that SS-8 solidified waste has undergone some fission product migration or phase separation. However, the evidence for this migration or separation is not fully conclusive at this time.

Environmental testing and facility operation have been smooth. No unexpected product characteristics have been found nor insurmountable operational problems encountered. No waste container pressurization has occurred which indicates that the products under test have been chemically stable for the storage periods.

Engineering Data Analysis - R. J. Thompson

A regression analysis of available spray solidifier product effective thermal conductivity (k_{eff}) data shows that there is no correlation (at very high confidence) between k_{eff} and the average product temperature. That is, a mean or average value of k_{eff} of approximately 1.2 $W/(m^2)(°C/m)$ may be used over the temperature range investigated (100 to 600 °C).

TABLE 5.10. SSETF Environmental Test Summary

Run No. Pot No. Cubicle No.	Date Testing Started	Pod Environment	Maximum Temperature, °C[a] Pod	Pot Wall	CL	General Remarks
SS-4 40 A-21-3	9/11/69	Water	91	94	166	No container pressurization has occurred No operational or test problems have been encountered.
PG-6 39 A-21-1	10/1/69	Water	93	99	181	Same as SS-4
PC-6 30 A-21-4	11/17/69	Air	502	--	595	Same as SS-4
SS-8 43 A-21-2	1/5/70	Air	521	548	636	Some unusual temperature distributions within the product indicate the possibility of fission product migration and/or phase separation. Conclusive evidence is not available.

a. Temperature data recorded 1/14/70

Figure 5.5 shows the effective thermal conductivity of spray solidifier product as a function of average product temperature for the data analyzed. The three very high values of k_{eff} for WSEP Run SS-6 were disregarded in the regression analysis because of the significantly different thermal history of SS-6.*

Disregarding these high k_{eff} values in the regression analysis should not be interpreted as discarding the SS-6 data. Quite the contrary, significant impact on product characteristics could result, and the container will continue to be observed. The results presented here represent analyses of data beyond those presented in BNWL-1186.

A regression analysis of the effective thermal conductivity (k_{eff}) for phosphate glass solidified waste as a function of average product temperature has been completed for WSEP Runs PG-1 through 11. As opposed to the spray solidifier product analysis, the phosphate glass product k_{eff} does correlate with average product temperature at better than 99.9% certainty.

Figure 5.6 shows the phosphate glass data studied and the regression curve fit. The three products from feed types PW-1, PW-2, and PW-4m were compared by statistical techniques to determine if they should be treated independently. However, it was not possible to determine if the variation in measurements among products is real or due to measurement fluctuations. Therefore, the data presently indicate that k_{eff} for phosphate glass product should be treated independently of solidifier feed type according to Equation (1).

$$k_{eff} = 0.719 + 6.630 \times 10^{-4}\ t \qquad (1)$$

---

* *BNWL-1186, 69-2.*

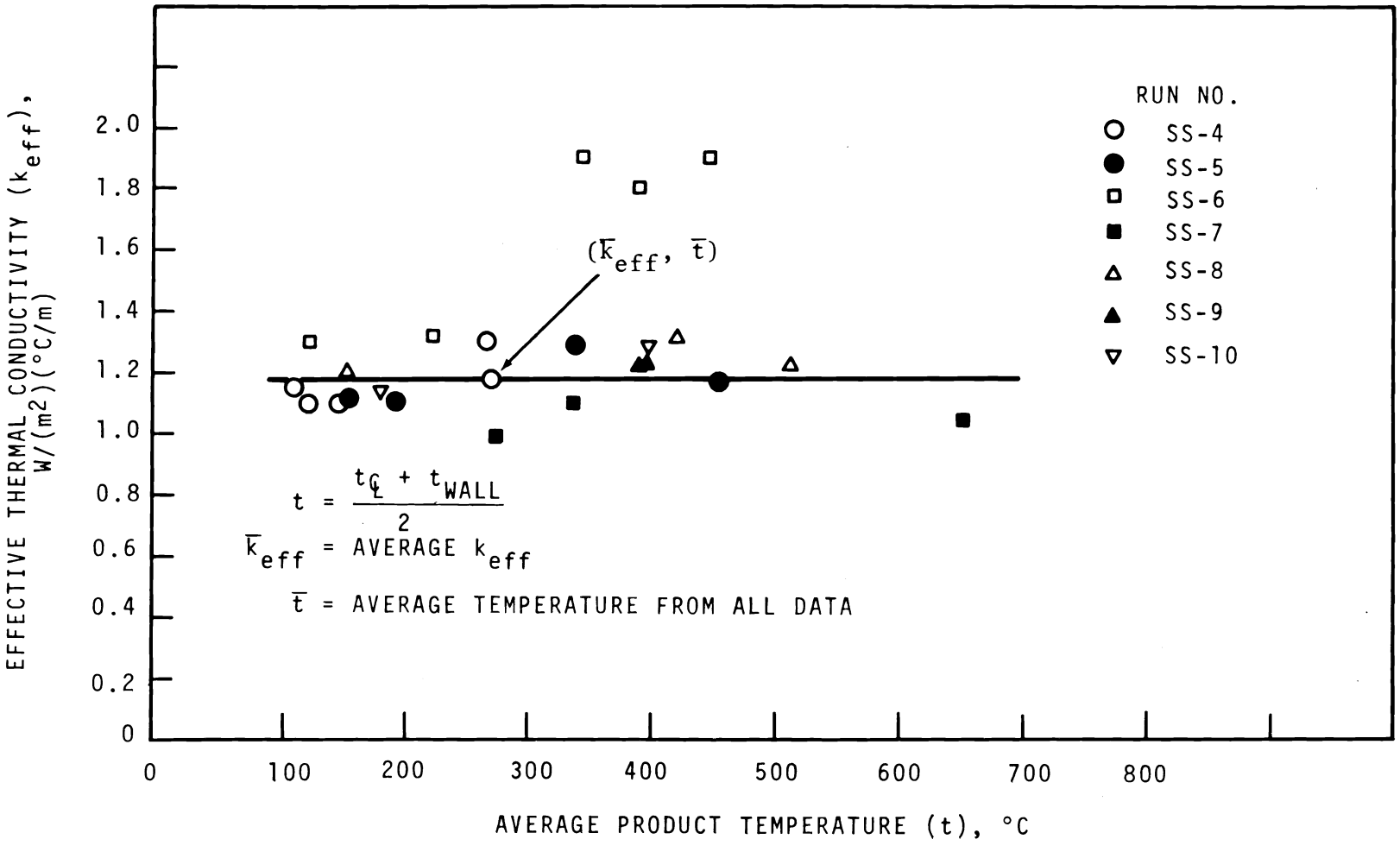

FIGURE 5.5. Effective Thermal Conductivity of Spray Solidifier Waste

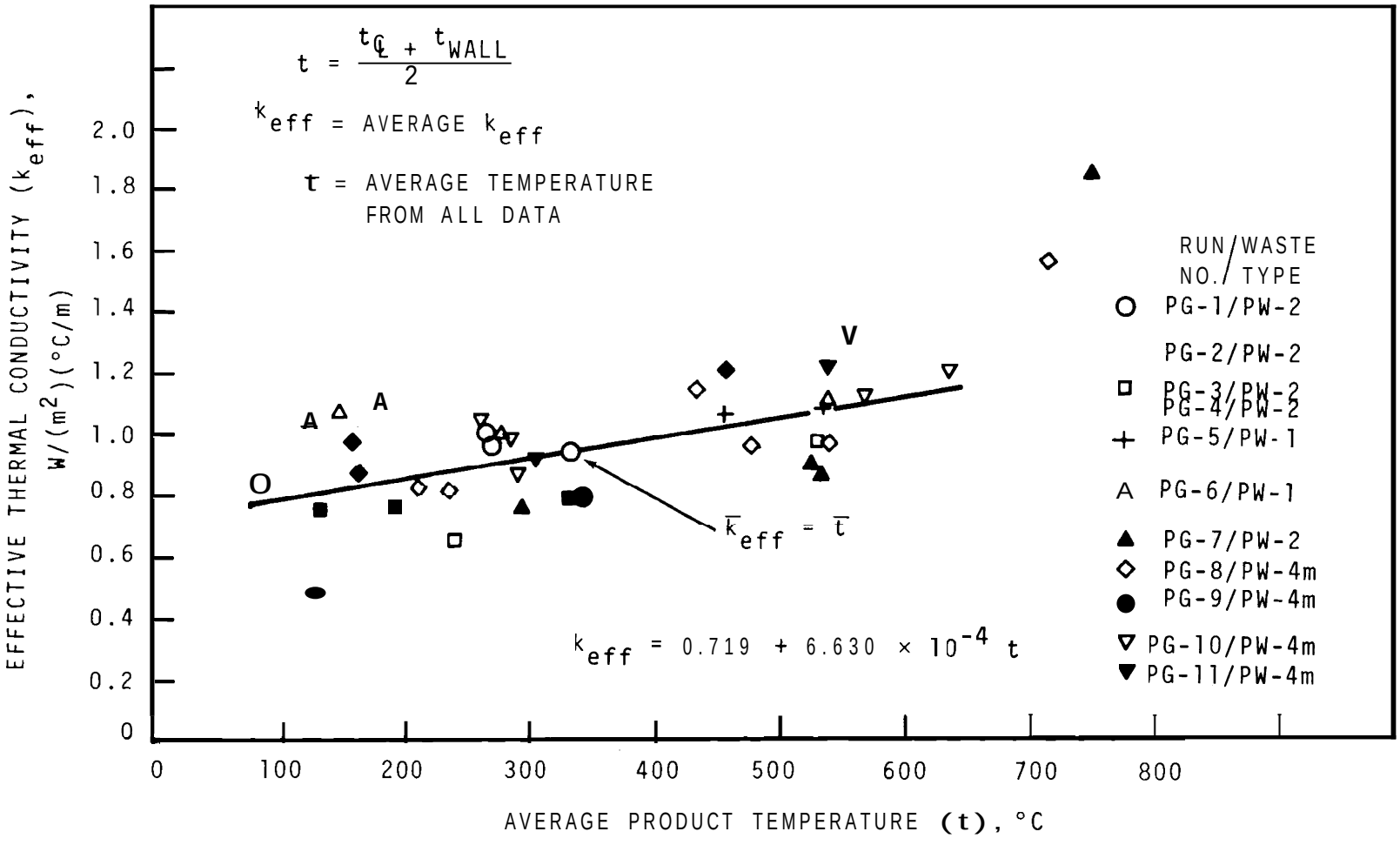

FIGURE 5.6. Effective Thermal Conductivity of Phosphate Glass Solidified Waste

As data collection continues, it may be possible to further refine and differeniate among the types of phosphate glass products.

Figure 5.6 shows two data points that were not included in the regression analysis, but like the unusual SS-6 k_{eff} data, the data may have significant impact on the phosphate glass product characteristics. The two data points which are at high average product temperature (720 °C and 750 °C) were not included in the regression analysis because most of the product is above the remelt temperature (the remelt temperature is taken to be 650 °C based on laboratory data) and not typical of the other data used in the analysis.

However, this does not mean that the data should be discarded and, in fact, does point'out a potentially important feature of phosphate glass solidified waste in that the k_{eff} significantly increases when the product temperature reaches or exceeds the remelt temperature.

6. HEAVY SECTION STEEL TECHNOLOGY PROGRAM

IRRADIATION EFFECT ON THE FRACTURE OF HEAVY SECTION PRESSURE VESSEL STEELS - C. W. Hunter, J. A. Williams, C. L. Hellerich

Specimen Irradiations

Specimen irradiations, including 1-in. thick compact tension (1T CT) and tensile specimens, were conducted during Cycles 101 through 104 in the M-3 loop facility of the ETR reactor. The M-3 facility is capable of producing specimens irradiated to 1 to 2 × 10^{19} n/cm^2 (E > 1 MeV) at approximately 540 °F in one reactor cycle. The irradiation capsule was designed so that removal and replacement and positioning of specimens could be accomplished during reactor outages. The capsule is also adaptable for use in irradiating other types of specimens. The total irradiations completed to date include 12 CT specimens of base material at approximately 1.5 to 2.5 × 10^{19} n/cm^2, 12 CT specimens of weld and HAZ to a fluence of approximately 1.5 to 2.5 × 10^{19}, and 4 CT specimens of base material at 7 to 8 x 10^{19}. A total of 64 tensile specimens have been irradiated to levels from 1.5 to 8 × 10^{19} n/cm^2.

At the completion of Cycle 104 the G-7 loop facility was removed from the ETR. This was of major significance to operation of the M-3 facility, since, through the use of heat exchangers, the in-reactor G-7 hot water loop supplied the necessary heat input for maintaining temperature in the M-3 facility. Prior to removal of the G-7 tube plans were initiated to install an electrical heating system in the M-3 loop facility for maintaining test temperature. With the electrical heating system temperatures other than the current operating temperatures (500 to 510 °F) will be obtainable. To date, all designs have been completed, components ordered and installation is scheduled for Cycle 107 of the ETR during April.

The temperature distribution along the M-3 capsule for Cycle 101 has been previously described.' In Cycle 102 and beyond, the inlet water temperature was increased 5 to 10 °F. Considering this change as well as the axial temperature distribution along the capsule, the tensile specimen temperature range has been 500 to 510 °F and CT specimen range has been 530 to 545 °F, with most of the specimens in the upper portion of the respective ranges.

The M-3 capsule cycle flux monitors for Cycles 101 through 104 have been analyzed and are plotted in Figure 6.1. The flux monitors are Fe, Ti and Al-Co. Additional values will be obtained and the fluence values refined as the analysis of flux monitors located in CT specimen holes is completed. The cycle flux monitors occupied the same position during Cycles 101 through 103, near the front of the capsule with respect to reactor center. During Cycle 104 the monitor was exchanged with a tensile specimen tube near the rear of the capsule, approximately 1 1/2 in. radial distance from the position of the previous cycles. Comparisons of flux data obtained by this method do not yield an interpretation of the radial flux gradient as was initially expected. Peak flux of Cycles 101 through 103 shown in Figure 6.1 varied a maximum of about minus 20% from the highest value. Based on other reactor data it was estimated that a decrease of as much as 30% may be expected between the monitor position of Cycle 104 and Cycles 101 through 103, which would have placed the flux values during Cycle 104 at least as low as the lowest values obtained during the previous cycles. The flux values obtained in the 104 position were, however, higher than those previously obtained.

The experimental gamma heat survey of candidate positions for irradiating a large specimen capsule in the ETR has been completed. The survey was prompted by the uncertainity of

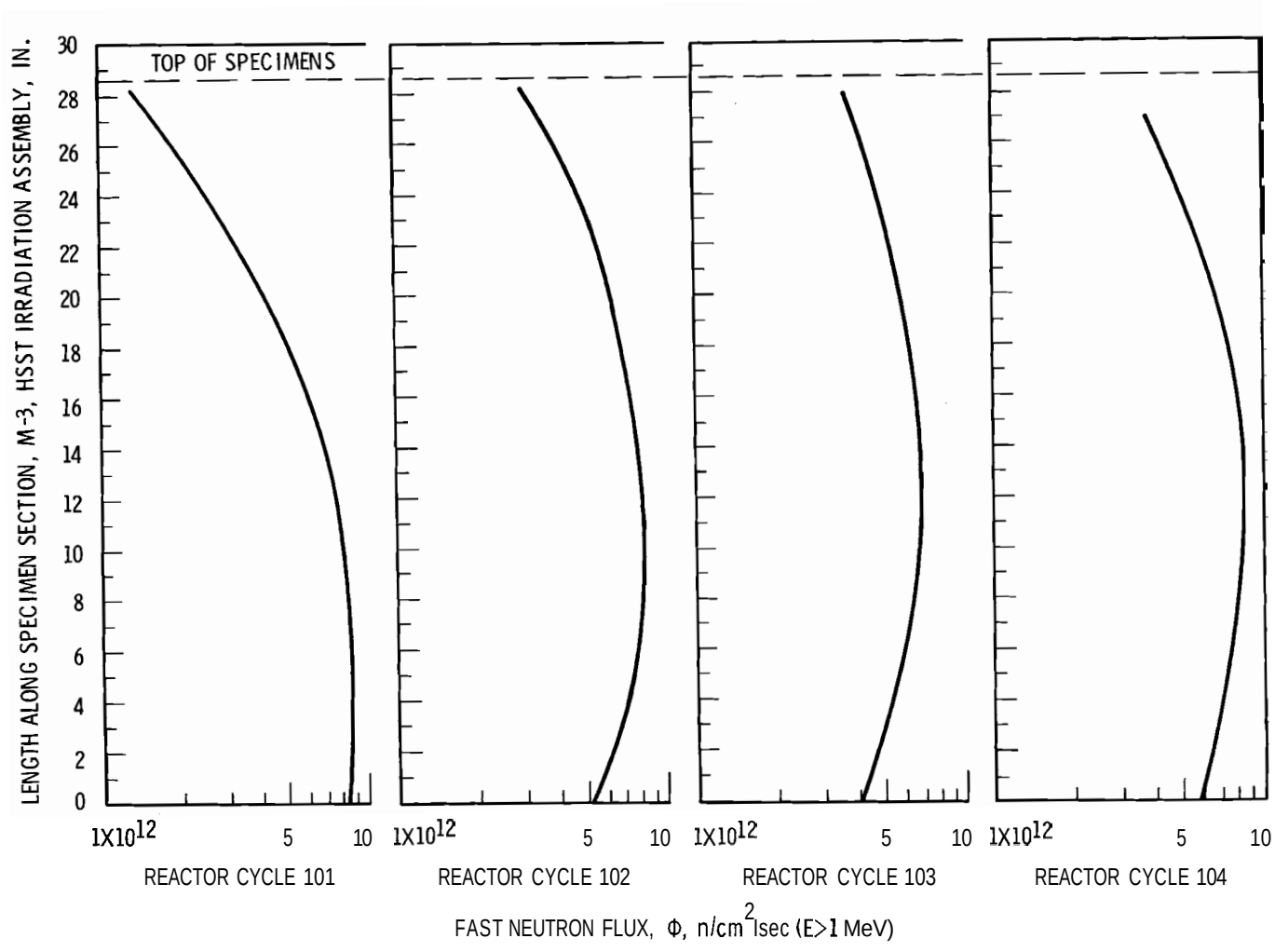

Neg 700453-6

FIGURE 6.1. **Fast Flux Distribution Over the Length of the ETR, M-3 Loop, HSTT Specimen Irradiation Assembly for Reactor Cycles 101 Through 104**

gamma heat data, a factor of major importance in the capsule design. For the farthest position from the core available the gamma heat rate would be 0.9 W/g at the front surface and 0.3 W/g at the back surface of a 4-in. thick specimen. Based upon earlier heat transfer calculations[2] this gamma heat rate would result in a temperature differential of approximately 100 °F in the specimen: In order to maintain 550 °F at the specimen center with this high gamma heat rate, a gas gap of only 0.002 in. would be required. These results and evaluations demonstrated that a lower value of gamma heat, such as that in the ATR, would be preferable. In the ATR, reflector positions are available with gamma heat rates of 0.3 to 0.1 W/g front to rear respectively through a 4-in. specimen as shown in Figure 6.2. Under these conditions the temperature differential through the specimen will be about 30 °F.

Estimates of the flux in the candidate positions of the ATR have been made and flux measurements are in progress. The highest estimate of fast flux is 2×10^{12} n/cm^2/sec (E > 1 MeV) based on theoretical attenuation from a known position. An estimate based on the ratio of fast flux to gamma heat also yields 2×10^{12} n/cm^2/sec at the center of the 4T capsule position. Based on these flux values, two reactor cycles with rotation of specimens between cycles would yield a specimen exposure of 1.2×10^{19} n/cm^2. Ten cycles with rotation after five cycles will yield a fluence of 6×10^{19} n/cm^2. The proposed ATR - 4T irradiation capsule is shown in Figure 6.3. With this arrangement of two capsules with two specimens each the following irradiations could be produced:

(1) 2-base plate, WR orientation, 6×10^{19} n/cm^2.
(2) 4-base plate, WR orientation, 1.2×10^{19} n/cm^2.
(3) 4-base plate, RW orientation, 1.2×10^{19} n/cm^2.
(4) 2-weld metal, 1.2×10^{19} n/cm^2.

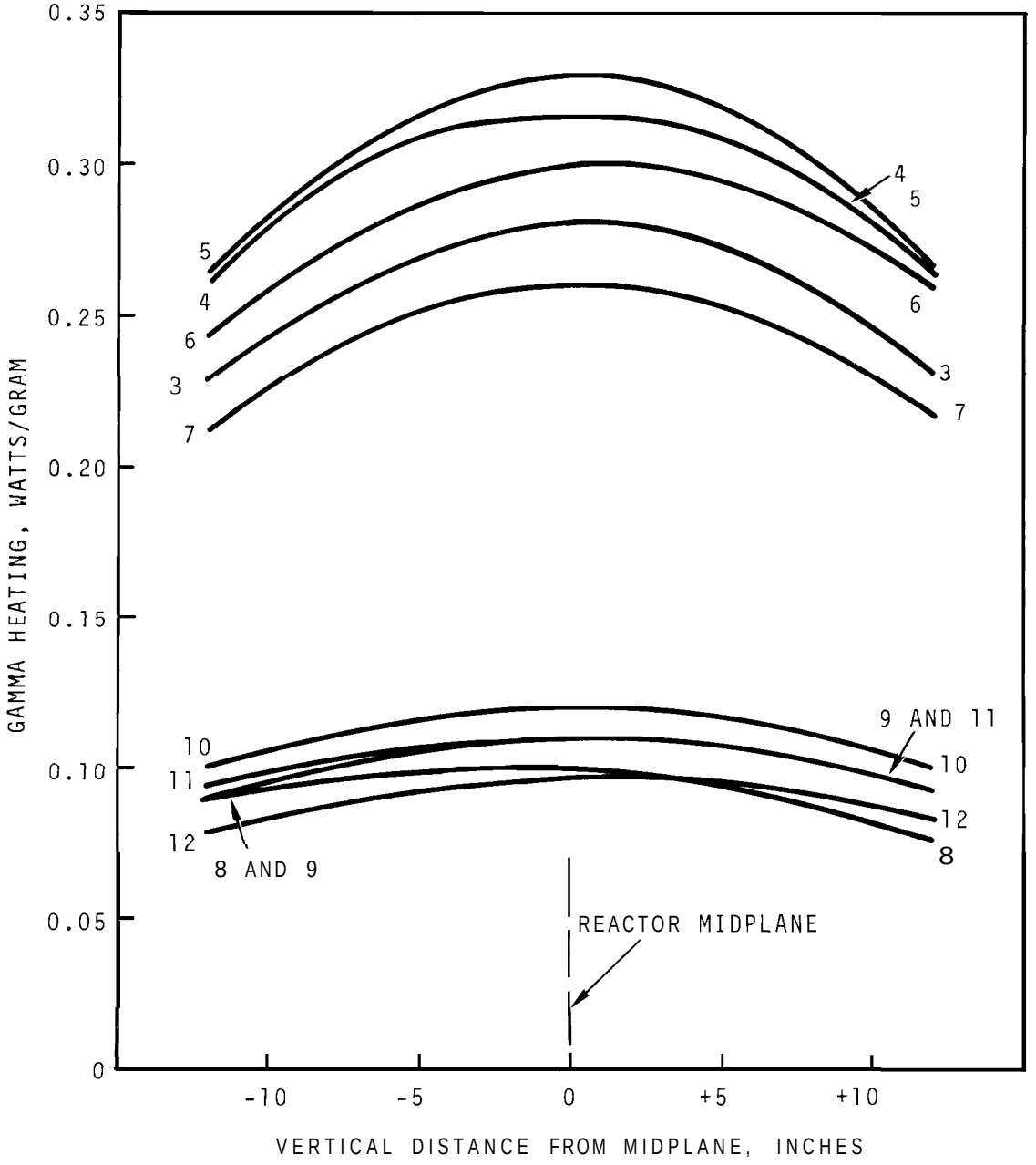

Neg 700453-3

FIGURE 6.2. **Gamma Heat Distribution for Positions to be Occupied by the ATR-4T Irradiation Facility. Curves numbered 3,4,5,6 and 7 are at the front plane, and curves numbered 8,9,10,11 and 12 are at the back plane of the fracture specimens shown in Figure 6.3.**

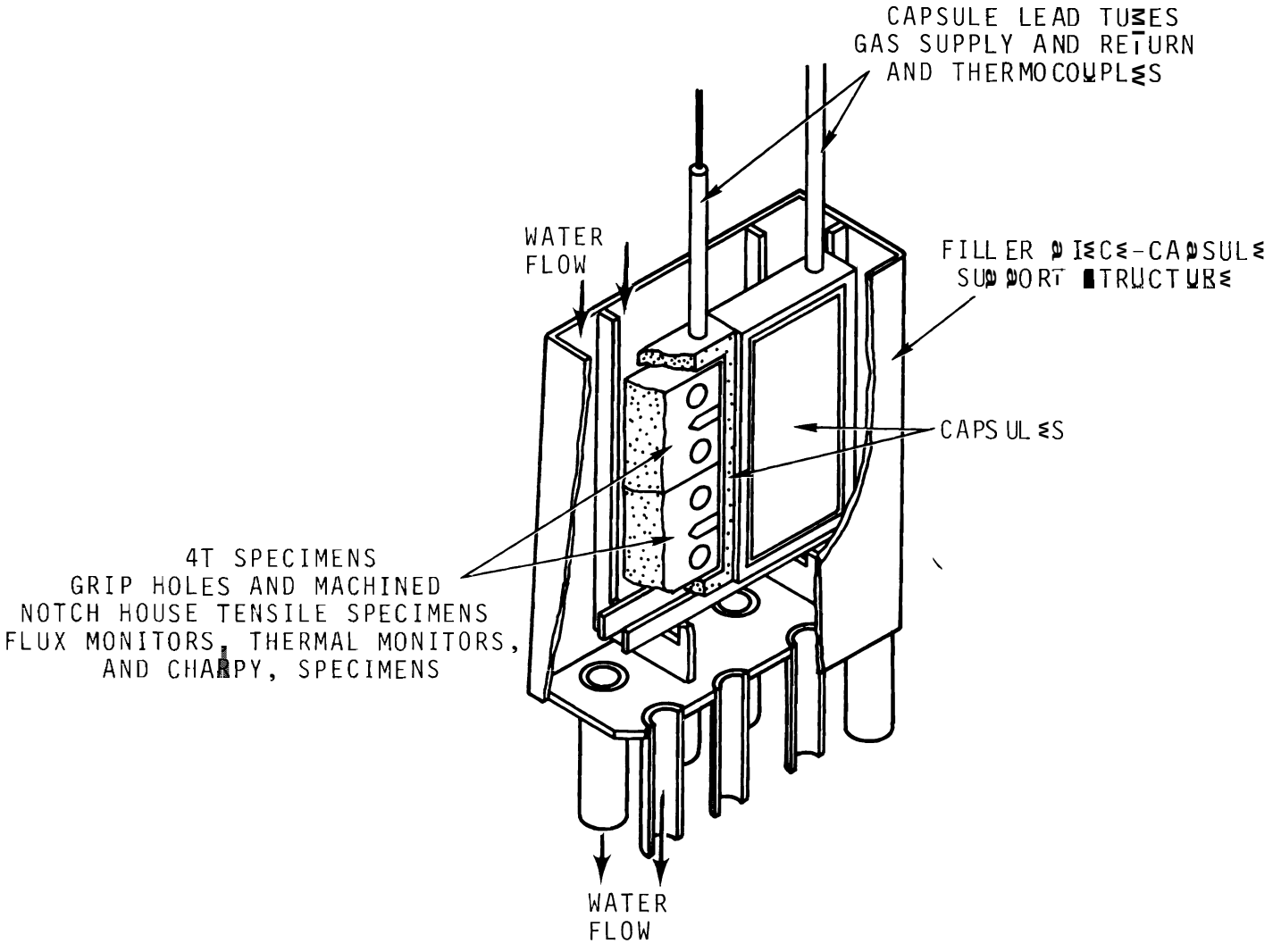

Neg 700953-2

FIGURE 6.3. Schematic View of ATR-4T Irradiation Facility

Irradiations 2, 3 and 4 would run concurrently with irradiation 1. The lowest estimate of fast flux, obtained from the ratio of fast to thermal flux, is approximately 9×10^{11} n/cm^2/sec. Irradiations at this level would require twice as many cycles to attain similar goal exposures discussed above.

The ATR-4T irradiation facility of Figure 6.3 will replace 10 reflector position filler pieces. The capsule support structure will be approximately 9.5 in. × 22.5 in. × 57 in. long. Two capsules will be irradiated concurrently with each capsule containing two 4T fracture specimens and the specimen grip holes and notches will be filled with tensile specimens, charpy specimens, flux monitors and thermal monitors. The capsules will be instrumented with thermocouples. Temperature control will be obtained by regulation of gas mixture supplied to the capsule.

Base Material Studies of Annealing and Fluence Effects

A cursory examination of the recovery of irradiation damage of ASTM A533-B tensile properties was conducted. The objective of this study was to determine the temperature range in which significant recovery occurred and the extent of recovery which could be expected. As previously reported herein, the irradiation temperature of tensile specimens in the M-3 loop is between 500 and 510 °F while maximum temperatures at the center of the 1T CT specimens was between 530 and 545 °F. It was therefore desirable to determine if tensile properties at the irradiated temperature were similar to those which would be obtained at the higher temperature.

Tensile specimens irradiated to a higher fluence, ∿4.3 × 10^{19} n/cm^2 (>1 MeV), were also tested and compared to the specimens which were irradiated at approximately 2 × 10^{19} n/cm^2. These will be supplemented with future tests to determine the effect of fluences to 8 × 10^{19} n/cm^2 on tensile and fracture properties.

The results of these studies are presented in Table 6.1 and Figures 6.4, 6.5 and 6.6. Tensile specimens irradiated to 1.7 to 2.4 × 10^{19} n/cm^2 at a temperature between 500 and 510 °F were annealed at 540, 600, 650 and 725 °F for 130 hours. The tensile specimens annealed at 725 °F had been previously annealed at 650 °F for 130 hours. The specimens were tested in a range from room temperature to 500 °F. As shown in Figure 6.4 approximately 70% of the change in room temperature yield strength induced by irradiation was recovered after annealing at 650 °F. Increasing the annealing temperature to 725 °F did not yield any significant additional recovery over the 650 °F anneal. No significant recovery of irradiated properties was obtained below 550 °F. The results of Figure 6.4 are typical of both the yield strength and the ultimate strength over the temperature range to 500 °F, as demonstrated by Figures 6.5 and 6.6.

If indeed the change in yield strength is a measure of the change in fracture properties, then one could expect significant recovery of fracture properties at annealing temperatures as low as 600 °F. Similarly, it may be expected that appreciably less degradation in toughness will occur during irradiation at 600 °F. The fact that as much residual damage exists after annealing at 725 °F as at 650 °F suggests that much higher temperatures would be required to recover all the irradiation damage, if such an event is possible at all in the range of practical interest. Studies at NRL[3] reveal that Charpy-V notch ductility of 6-in., A302-B steel was observed to exhibit approximately 70% recovery after annealing at 800 °F for 168 hours. Varying degrees of recovery of notch ductility for a number of materials and conditions are reported elsewhere.[4,5]

The lack of any observed recovery of tensile properties at 540 °F lends confidence to the results of the 500 to 510 °F tensile irradiations being closely representative of tensile properties which might be obtained when irradiating at 540 °F.

TABLE 6.1. Tensile Properties of Irradiated A533, Grade B Class I Steel From HSST Plate 02, Longitudinal Specimens

Specimen Identification	Test Temperature °F	Test Temperature °C	Plate Position[a]	Fluence $\times 10^{19}$ n/cm^2 (E > 1 MeV)	Yield Strength 0.2% Offset $\times 10^3$ psi	Ultimate Strength $\times 10^3$ psi	Annealing Temperature[b] °F
02GA 156	90	32	5/19	2.26	93.9	110.6	540
02GA 157	500	260	5/19	2.40	82.3	104.4	540
02GA 232	90	32	9/19	1.8	80.2	98.7	600
02GA 233	250	121	9/19	1.9	76.0	94.1	600
02GA 234	500	260	9/19	1.97	70.7	94.9	600
02GA 238	83	28	9/19	1.8	73.8	92.8	650
02GA 239	250	121	9/19	1.9	69.4	88.2	650
02GA 240	500	260	9/19	1.97	66.2	90.7	650
02GA 186	84	29	7/19	2.26	75.7	97.1	725[c]
02GA 187	500	260	7/19	2.40	67.5	92.4	725[c]
02GA 193	-100	-73	7/19	4.31	118.1	130.2	---
02GA 164	89	31	6/19	4.41	103.4	118.1	---
02GA 168	250	121	6/19	4.31	96.4	112.7	---
02GA 191	500	260	7/19	4.41	86.3	107.2	---

a. Fraction of thickness at specimen center line.

b. Annealing time, 130 hours.

c. Re-annealed after annealing 130 hours at 650 °F.

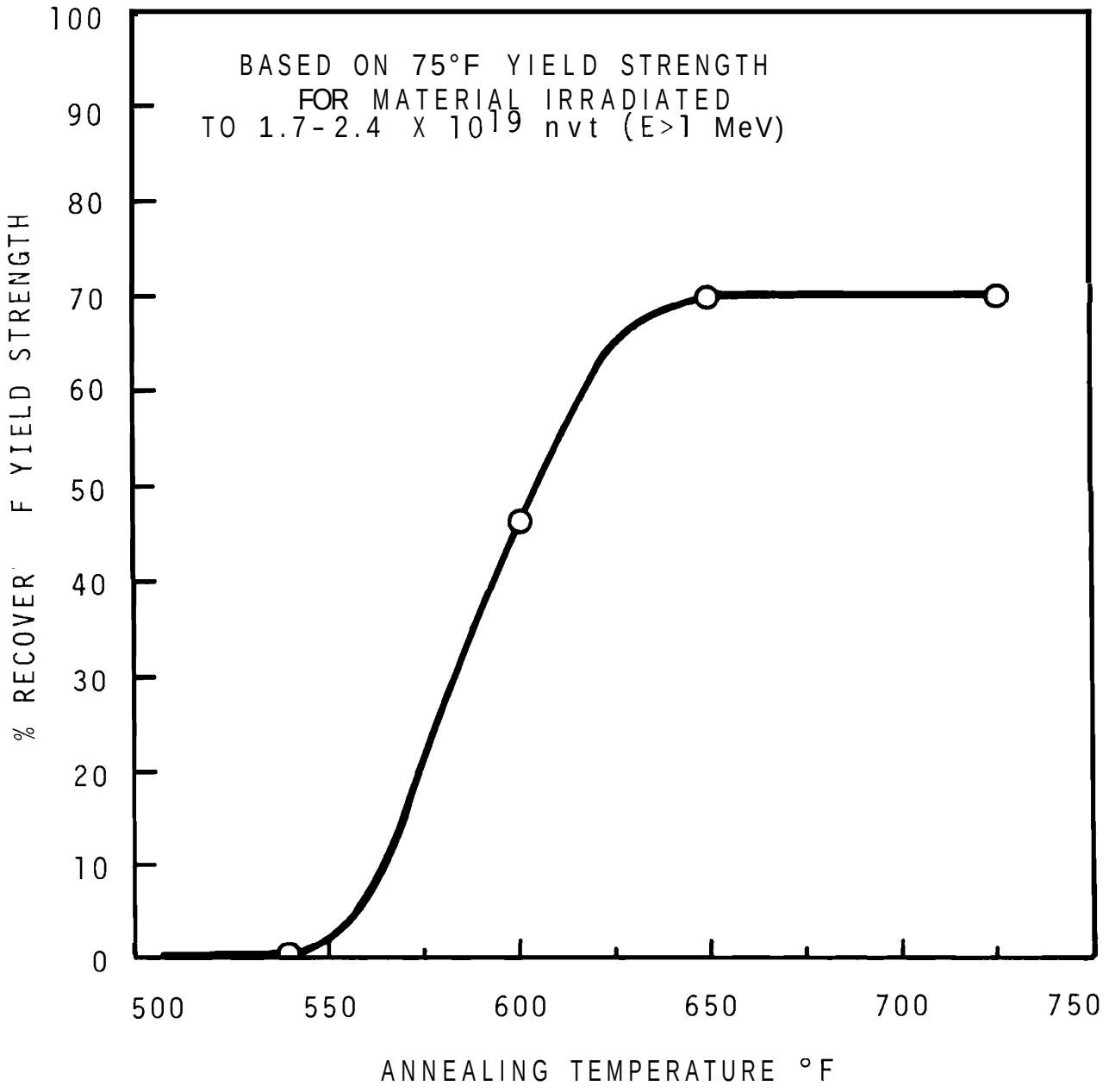

Neg 700453-1

FIGURE 6.4. **Recovery of Room Temperature Yield Strength During Postirradiation Annealing for 130 Hours. ASTM A533-B Base Material from HSST Program Plate 02**

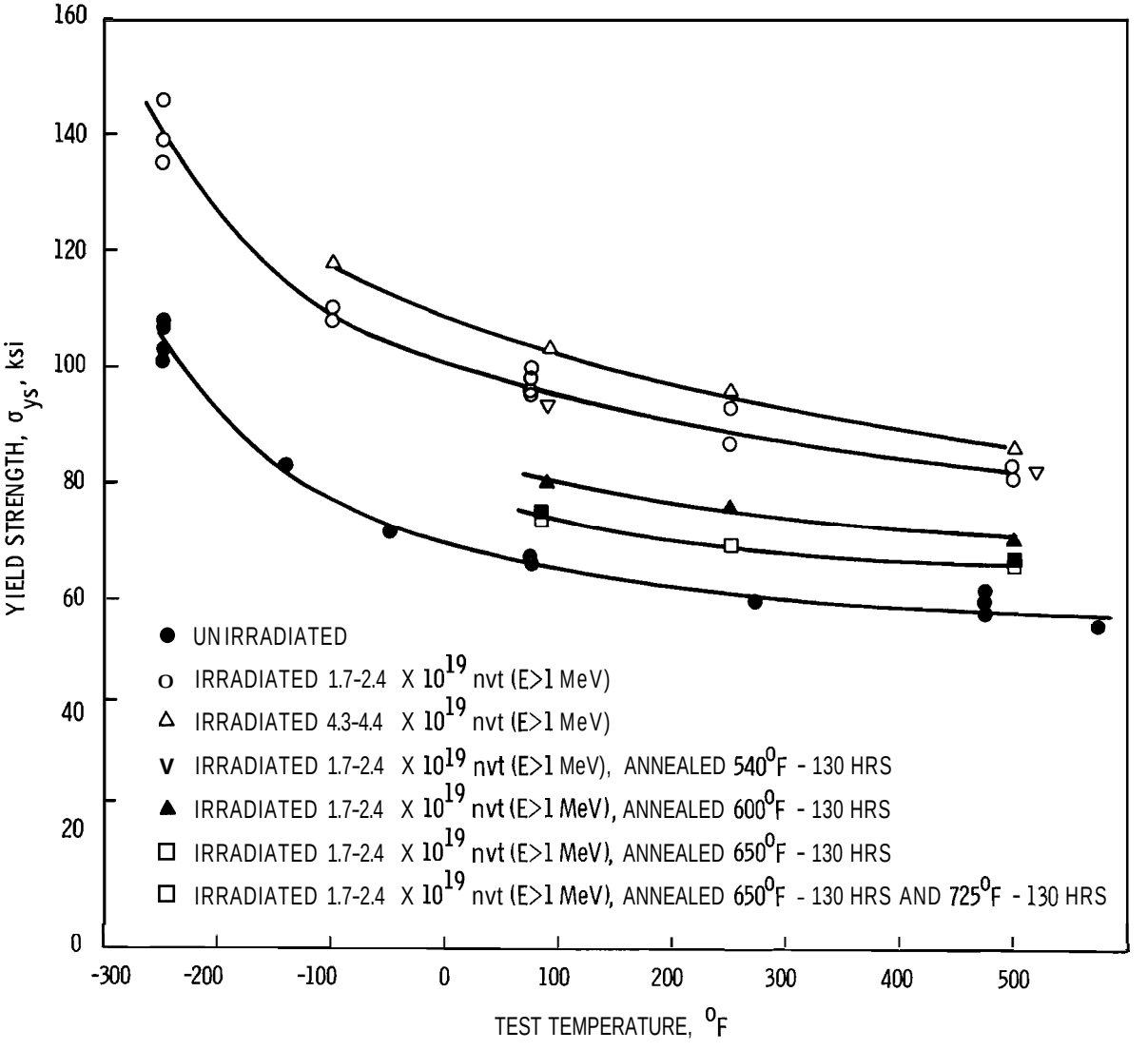

Neg 700453-7

FIGURE 6.5. Yield Strength of ASIM A533-B HSST Program Plate 02 at Two Fluence Levels and After Postirradiation Anneal

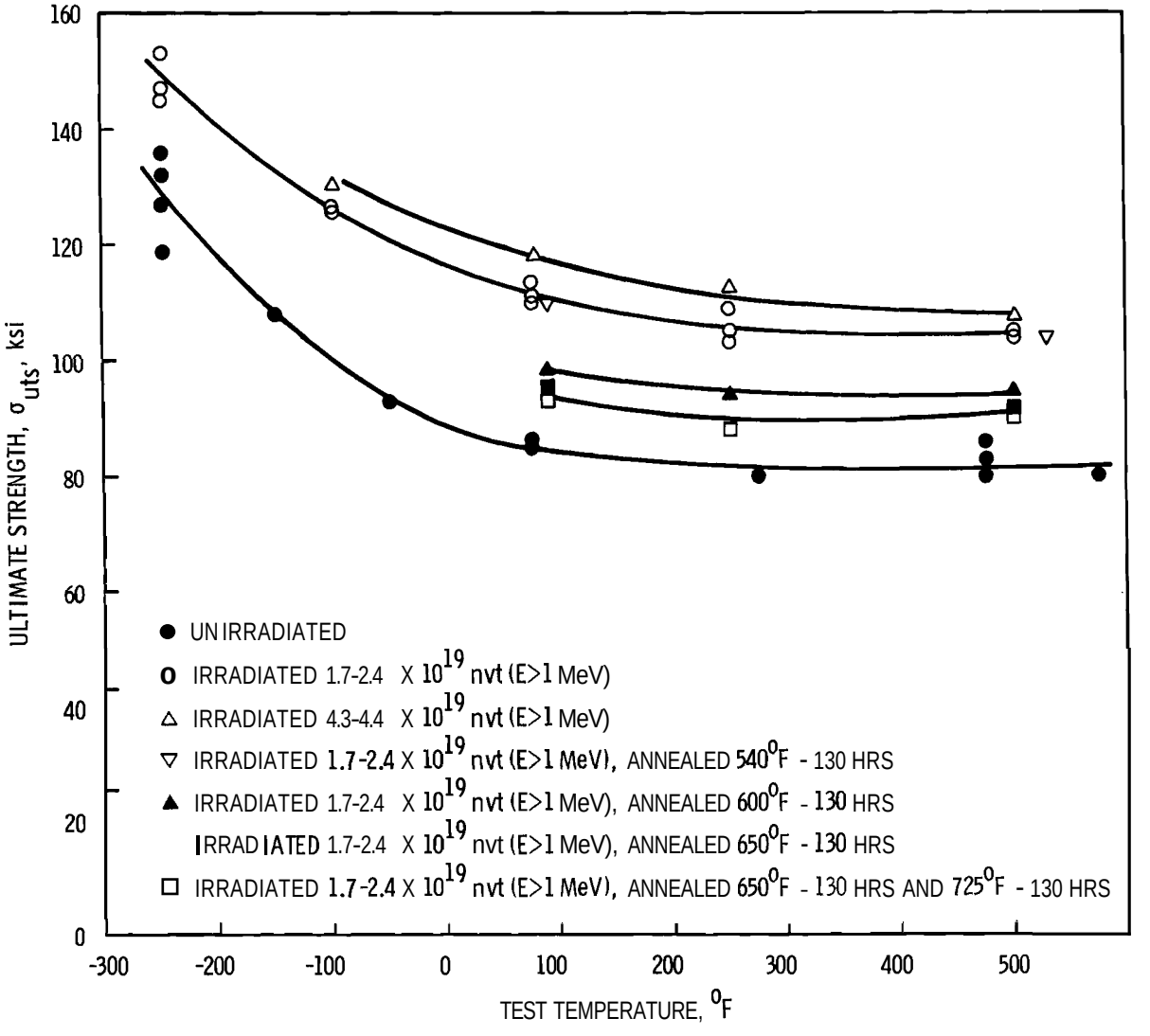

FIGURE 6.6. **Ultimate Tensile Strength of ASTM A533-B HSST Program Plate 02 at Two Fluence Levels and After Postirradiation Anneal**

If any significant difference were to be expected at the 540 °F irradiation temperature, then one would also expect a significant change as a result of postirradiation heat treatment at the 540 °F temperature.

The tensile specimens irradiated to a fluence of 4.3 to 4.4 × 10^{19} n/cm^2 were tested from -100 °F to 500 °F. Approximately a 6 to 7% increase in room temperature ultimate and yield strength was observed over the 1.7 to 2.4 × 10^{19} n/cm^2 irradiation properties.

Fatigue Crack Preparation in CT Specimens

In linear elastic fracture toughness determination, the critical stress intensity (K_{Ic}) is that for fracture initiation from a sharp fatigue crack. Hence, the preparation of a fatigue crack in the fracture specimens is a necessary preliminary to actual toughness determinations. Consideration of the loading conditions during such fatigue crack preparation provides an opportunity to extract some information on fatigue crack behavior. To be sure, these loading conditions were not intended to provide pure propagation data, such as the crack growth rate per cycle (da/dN) versus cyclic stress intensity (AK) relationship developed by Paris.[6] Nevertheless, this information does offer some examples of and insight into the practical situations of crack initiation, stalling, and re-initiation, (incubation) as well as propagation.

The specimens were IT CT specimens; the materials were the same 12-in. thick A533-B HSST program plate and subarc weldment utilized throughout this investigation. The base material specimens were RW orientation from quarter through center positions. The fracture planes of the weldment specimens were parallel to the weld and located at positions A, B, and C throughout the weldment; as previously described.[1,2] A is the center of the weld metal, B is the weld dilution region

(on the weld side of the fusion line), and C is the austenitic grain growth region in the HAZ (on the base metal side of the fusion line). All load cycling was from zero to tension to provide the intended AK and was performed at 1800 cycles/min in air at room temperature.

The fatigue cracks were initiated from a machined notch of 0.002 to 0.005-in. radius and subsequently grown a total of 0.200-in. in several steps at different levels of AK. Three different patterns of stress intensity were employed; the various steps in each of these three patterns are listed in Table 6.2. The crack lengths for each step in Table 6.2 are the distance from the point of load application to the crack tip in the specimens. All three patterns were utilized in the fatiguing of the base material specimens. Only Pattern III was employed with the weldment specimens. With Patterns I and II, the AK was substantially reduced in Step 2 after crack initiation in Step 1; typically this reduction greatly reduced the propagation rate and in some instances stalled it. In the specimens of stalled propagation the higher AK of Step 3, Pattern II was employed to re-initiate propagation; after re-initiation, Steps 4 and 5 of Pattern II were similar to Steps 2 and 3 of Pattern I. In essence then, Patterns I and II were the same except that Pattern II incorporated a step to re-initiate the stalled cracks which sometimes occurred during Step 2. Stalling was not prevalent in Pattern III because the AK decrease from Step 1 to 2 was not so large.

The corresponding values of effective crack growth rate and AK. for each step are plotted in Figure 6.7 for the base material specimens and in Figure 6.8 for the weldment specimens. It must be emphasized that these values of crack extension rate per fatigue cycle include periods when the crack was initiating, stalled, and re-initiating as well as pure propagation. The typical relationship between AK and pure crack propagation is indicated in Figures 6.7 and 6.8.

TABLE 6.2. Basic Stress Intensity and Propagation Patterns Employed in the Fatigue Crack Preparation of 1T CT Specimens of A533-B Plate and Weld

	PATTERN I	*PATTERN II*	*PATTERN III*
STEP 1 (from machined notch)	26 ksi$\sqrt{in.}$ 0.78 to 0.80 in.	26 ksi$\sqrt{in.}$ 0.78 to 0.80 in.	26 ksi$\sqrt{in.}$ 0.78 to 0.80 in.
STEP 2	17.5 to 20 0.80 to 0.89 in.	17.5 crack propagation stalled at 0.80 in.	21 to 24 0.80 to 0.90 in.
STEP 3	16.5 to 19 0.89 to 0.98 in.	21 to 22 crack propagation restarted to 0.84 in.	17 to 19 0.90 to 0.97 in.
STEP 4		18 to 20 0.84 to 0.89 in.	13 0.97 to 0.99 in.
STEP 5		16.5 to 19 0.89 to 0.98 in.	

The extent by which the data in Figures 6.7 and 6.8 fall below the band for typical propagation is a measure of the amount of hindrance provided by initiation stalling, re-initiation and pure propagation. The crack initiation in Step 1 from a machined notch is hindered a reasonable amount. The large ΔK decrease between Steps 1 and 2 (26 to 17.5 ksi$\sqrt{in.}$) in Patterns I and II always hindered extension. The ΔK decrease from Step 1 to 2 in Pattern III (26 to 21 ksi$\sqrt{in.}$) effected far less hindrance. Step 3 in Patterns I and III and Step 5 in Pattern II were not appreciably hindered. With the base material specimens Step 4 of Pattern III was not hindered, even though it involved a ΔK decrease from 19 to 13 ksi$\sqrt{in.}$ Apparently, both a ΔK decrease and a fairly high prior value of ΔK are requisites for re-initiation hindrance.

The behavior of the weldment specimens during Step 4 (13 ksi$\sqrt{in.}$) is quite varied. The specimens near the fusion line (areas B and C) exhibited cracking rates approaching

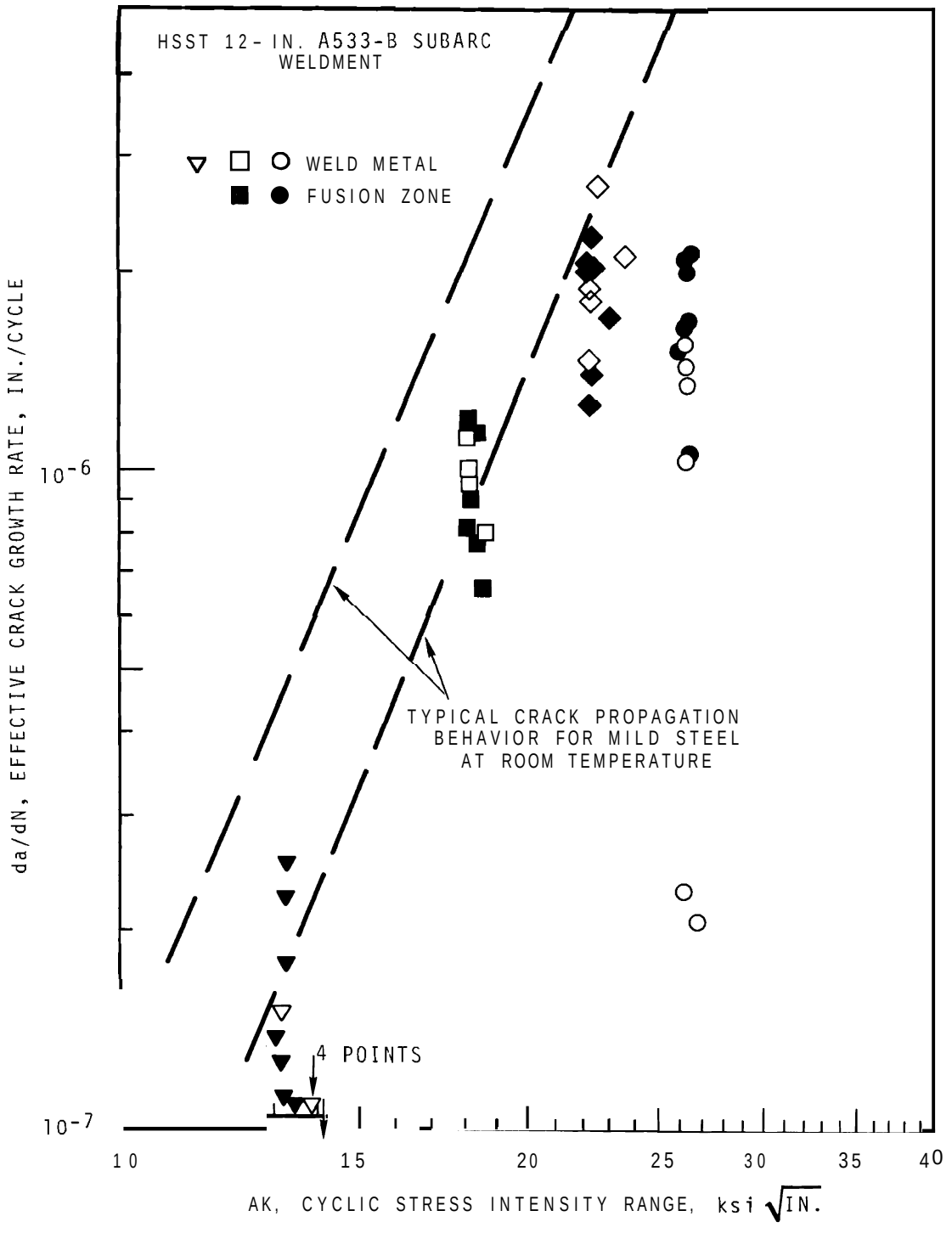

FIGURE 6.7. **Effective Fatigue Crack Extension Behavior in 1T CT Specimens Subjected to Different Patterns of Cyclic Stress Intensity. ASTM A533-B Base Material from HSST Program Plate 02**

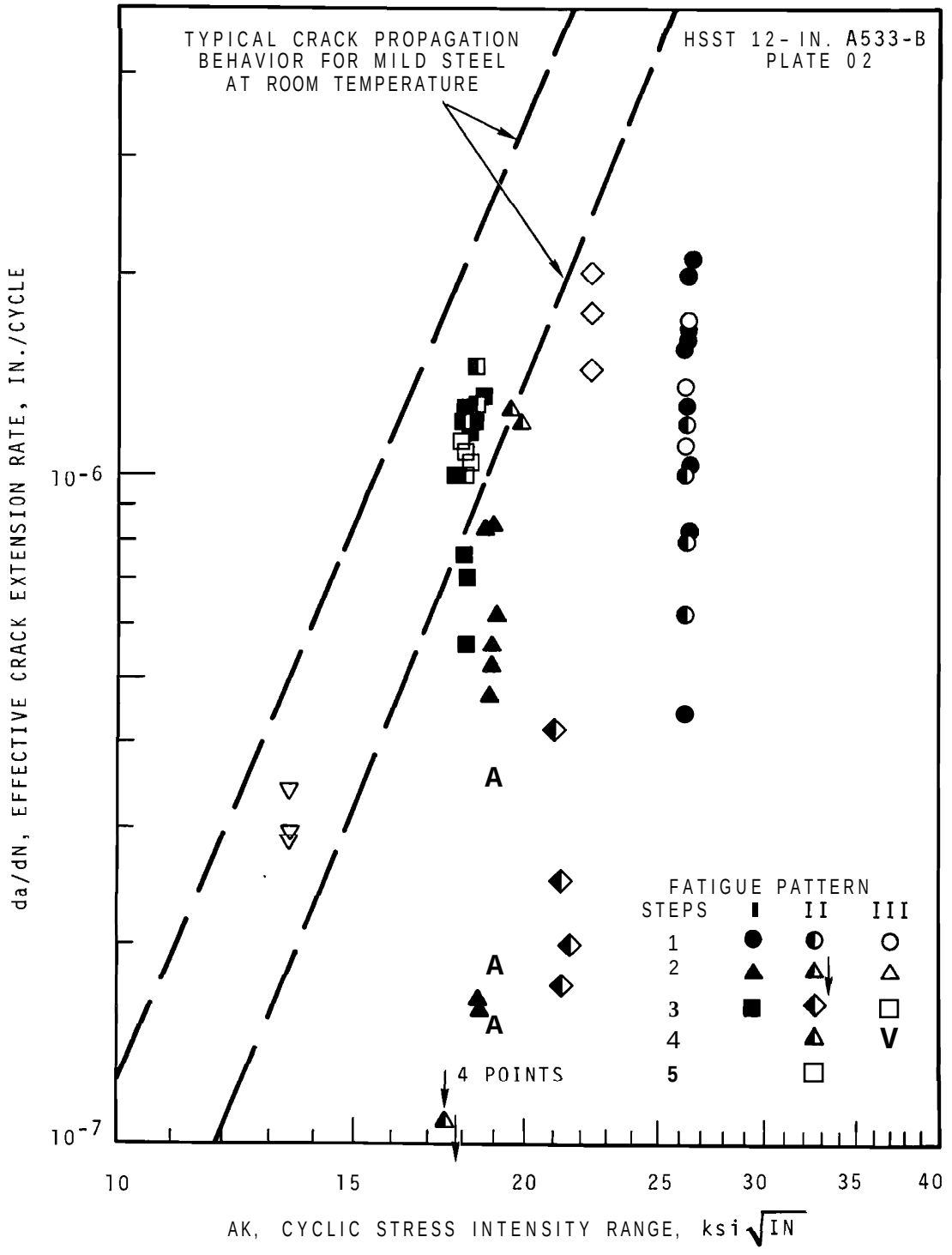

FIGURE 6.8. **Effective Fatigue Crack Extension Behavior in 1T CT Specimens in Weld Metal and Near the Fusion Line. ASTM A533-B Submerged Arc Weldment from HSST Program Weldment 51A**

typical propagation behavior. However, the cracking in the center of the weld metal (area A) was markedly hindered. A possible explanation for the hindered cracking in the weld metal may be the presence of rounded micro-inclusions which blunt the fine crack tip.

The direction which a crack wanders in the fusion region is also of potential significance. Table 6.3 lists the positions of the original machined notch and final crack tip in specimens near the fusion line (areas B and C). The distance, in mils, into either area B or C for both sides of the cracks are indicated. Based on these results, neither B nor C areas offer a preferential path for fatigue cracks.

TABLE 6.3. Position of the Machined Notch and Fatigue Crack on the Two Sides of the CT Specimens with Respect to the Fusion Line

	Distance From Fusion Line, Mills			
	Machined Notch		Fatigue Crack Root	
Specimen Number	B Weld Dilution Region	C Region of γ Grain Growth	B Weld Dilution Region	C Region of γ Grain Growth
51A 5021	5, 10		5, 9	
51A 5022	1	20		3, 30
51A 5023	10, 20		11, 42	
51A 5024	1	10	0	18
51A 5025	1	1	4, 15	
51A 5040	15, 40		0, 50	

References

1. Nuclear Safety QPR, Feb., March, April, 1969, BNWL-1084, pp. 6.1-6.7, June 1969.

2. Nuclear Safety QPR, May, June, July 1969, BNWL-1187, pp. 6.1-6.20, September 2969.

3. L. E. Steele, C. Z. Serpan, Jr., J. R. Hawthorne, Uldis Potapovs, and R. A. Gray, Jr., "Irradiation Effects on Reactor Structural Materials, QPR August 1 - October 31, 1968," NRL Memorandum Report 1937, November 15, 1968.

4. L. E. SteeZe, J. R. Hawthorne, H. E. Watson, C. Z. Serpan, Jr., and R. A. Gray, Jr., "Irradiation Effects on Reactor Structural Materials, QPR August I - October 31, 1969," NRL Memorandum Report 2058, November 15, 1969.

5. L. E. Steele, J. R. Hawthorne, C. Z. Serpan, Jr., Uldis Potapovs, H. E. Watson and R. A. Gray, Jr., "Irradiation Effects on Reactor Structural Materials, QPR November 1, 1968 - January 31, 1969," NRL Memorandum Report 1962, February 15, 1969.

6. H. H. Johnson and P. C. Paris, "Subcritical Flaw Growth," Engineering Fracture Mechanics, Vol. 1, No. 1, pp. 3-45, 1968.

DISTRIBUTION

No. of Copies

OFFSITE

1 AEC Chicago Operations Office
- D. M. Gardiner

1 AEC Chicago Patent Group
- G. H. Lee

2 AEC Division of Naval Reactors
- R. S. Brodsky

24 AEC Division of Reactor Development and Technology
- Assistant Director, Project Management
- Chief, Water Projects Branch
- Chief, Gas Cooled Projects Branch (2)
- Chief, Liquid Metal Projects Branch
- Assistant Director, Reactor Technology
- Assistant Director, Plant Engineering
- Assistant Director, Reactor Engineering
- Assistant Director, Nuclear Safety (5)
- Chief, Research and Development Branch
  - H. L. Hamester
  - R. R. Newton (5)
- Environmental and Sanitary Engineering Branch
  - I. C. Roberts
- Assistant Director, Engineering Standards
- Assistant Director, Program Analysis
- Assistant Director, Army Reactors

15 AEC Division of Reactor Standards
- M. Bolotsky
- G. Burley
- E. G. Case (10)
- A. B. Holt
- R. Waterfield
- R. Impara

267 AEC Division of Technical Information Extension

5 AEC Library, Washington

Advisory Committee on Reactor Safeguards
- F. R. Fraley

Division of Compliance
- L. Kornblith, Jr.
- J. W. Flora, Region IV

No. of Copies

Division of Operational Safety
H. Gilbert

Division of Production
G. B. Pleat

1 AEG - Telefunken
E-213
6 Frankfort/Main 70
AEG - Hochhaus Süd
Germany

Dieter Ewers

1 Aerojet-General
Idaho Falls, Idaho

W. E. Nyer

1 Aerojet-General
Sacramento, California

F. L. Climent

1 American Electric Power Co.
2 Broadway
New York, N.Y. 10004

Stephen J. Milioti

10 Argonne National Laboratory

C. E. Dickerman
S. Fistedis
R. O. Ivins
P. Lottes
H. O. Monson
D. Okrent
R. C. Vogel
P. G. Shewmon

LMFBR Program Office

A. Amorosi
L. Baker

2 Atomics International

H. Morewitz

Liquid Metals Engr. Center
R. W. Dickinson

No. of Copies

1 Auburn University
School of Engineering and Engineering Experiment Station

G. H. Nix

4 Babcock & Wilcox Co.
Virginia

S. Delicate
D. A. Nitti
R. Wascher

Washington

L. R. Weissert

6 Battelle Memorial Institute

A. R. Duffy
D. L. Morrison/D. L. Ritzman (1)
S. Paprocki (2)
D. N. Sunderman (2)

1 Battelle Memorial Institute
Frankfurt, Germany

G. Leistner/K. J. Kober

2 Bechtel Corporation

R. F. Griffin
W. P. Neuendorf

1 Bettis Atomic Power Laboratory
P. O. Box 79
West Mifflin, Pa. 15122

Dr. J. A. Redfield

2 Brookhaven National Laboratory

A. W. Castleman
J. M. Hendrie

1 Canoga Park Area Office

R. L. Morgan

No. of Copies

1 Chalk River Nuclear Laboratories
Chalk River. Ontario. Canada
Station 3
G. Hake

1 Combustion Engineering
M. F. Valerino

1 Consolidated Edison Company
J. J. Grob

1 du Pont Company, Aiken (AEC)
A. H. Peters

1 du Pont Company, Wilmington (AEC)
F. P. Allen for
Lombard Squires

1 H. Etherington
84 Lighthouse Drive
Jupiter, Florida 33458

1 W. L. Faith
2540 Huntington Drive
San Marino, California 91108

3 General Atomic Division (AEC)
A. J. Goodjohn (2)
R. H. Ball (1)

1 General Electric Company
621 S. W. Alder Street
Portland, Oregon 97223
J. E. Grund

3 General Electric Company, San Jose (AEC)
S. Vandenberg
G. E. Wade
E. Zebroski

1 General Electric Company, Cincinnati (AEC)
J. F. White

No. of Copies

4 General Electric Company, San Jose (Trumbull)

P. Bray
M. Siegler
W. A. Sutherland
D. A. Rockwell

1 Harvard Air Cleaning Laboratory

2 Idaho Nuclear Corporation

J. A. Buckham
C. M. Slansky

2 Idaho Operations Office (AEC)

D. Williams

2 IIT Research Institute

E. V. Gallagher
T. A. Zaker

1 Institut fur Mess- und Regelungstechnik
Laboratorium fur Reactorregelung und Anlagensicherung
Technische Hochschule Munche
8046 Garching Reactorstation
Munich, Germany

Prof. K. L. Garlid

1 Institut fur Reactorsicherheit
5 Koln, Lukasstrasse
Germany

Heinz G. Seipel

2 Los Alamos Scientific Laboratory

J. H. Russel
W. R. Stratton

1 H. G. Mangelsdorf
78 Knollwood Road
Short Hills, New Jersey 07078

1 MPR Associates, Inc.

T. Rockwell III

No. of Copies

1 National Bureau of Standards
C. Muehlhause

1 Naval Ordnance Laboratory
J. Proctor

1 North American Carbon, Inc.
P. O. Box 19737
Columbus, Ohio 43219
J. Louis Kovach

1 North Carolina State University
M. N. Ozisik

1 Nuclear Fuels Service
R. P. Wischow

14 Oak Ridge National Laboratory
R. E. Adams
R. Blanco
J. Buchanan
W. B. Cottrell (4)
D. Ferguson
C. E. Miller
G. W. Parker
L. F. Parsley
P. Rittenhouse
D. B. Trauger (2)

4 Oak Ridge Operations Office (AEC)
D. Cope (2)
E. Delaney
W. L. Smalley

1 A. A. O'Kelly
2421 West Rowland Avenue
Littleton, Colorado 80120

1 Ontario Water Resources Commission
Water Quality Surveys Branch
Division of Sanitary Engineering
135 St. Clair Avenue West
Toronto 7, Ontario, Canada
W. A. Steggles

No. of Copies	
1	Oregon State University James G. Knudsen
1	Pacific Gas and Electric Company W. Nutting
1	The Pennsylvania State University College of Engineering 101 Hammond Building University Park, Pennsylvania N. J. Palladino
14	Phillips Petroleum Company G. O. Bright G. F. Brockett S. Forbes (2) C. Haire G. B. Matheny W. E. Nyer (2) F. Schroeder (3) N. K. Sowards T. R. Wilson (2)
2	San Francisco Operations Office Atomic Energy Commission Lt. Col. J. B. Radcliffe C. V. Backlund
1	Sargent & Lundy Engineers 140 South Dearborn Street Chicago, Illinois 60603 O. A. Hrynewych
1	Southern Nuclear Engineering, Inc. P. O. Box 10 Dunedin, Florida G. Brown
1	Stone and Webster Engineering Corp., Boston L. P. Deackoff

No. of Copies

2 TRW Incorporated
TRW Systems Group
D. B. Langmuir
S. M. Zivi

1 United Engineers & Constructors, Inc.
1401 Arch Street
Philadelphia, Pa. 19105
A. T. Molin

1 United Kingdom Atomic Energy Authority
Authority Health and Safety Branch
Risley, Warrington, Lancs
England
A. R. Edwards

2 University of California, Berkeley
Institute of Engineering Research
H. A. Johnson
V. E. Schrock

1 University of Houston
Cullen Boulevard
Houston, Texas 77004
C. W. Zabel, Dir. of Research

1 University of Illinois
Department of Civil Engineering
3129 Civil Engineering Building
Urbana, Illinois 61801
C. P. Siess

1 University of Minnesota
Department of Chemical Engineering
Minneapolis, Minnesota 55455
H. S. Isbin

1 University of Tennessee
606 Dougherty Hall
Knoxville, Tennessee 37916
S. H. Hanauer

No. of Copies

1 University of Washington

Wells Moulton

1 USAEC Scientific Representative
c/o Atomic Energy of Canada, Ltd.
Chalk River, Ontario, Canada

H. J. Reynolds

6 Westinghouse Electric Corporation (AEC)
(APD)

E. Beckjord
D. Fletcher
H. Graves
F. M. Heck
R. A. Wiesemann

(HTD)

A. Lohmeier

1 Yankee Atomic Electric Co.
441 Stuart St.
Boston, Mass.

John DeVincentis

ONSITE-HANFORD

1 AEC Chicago Patent Group

R. K. Sharp (Richland)

2 RDT Asst. Dir. for Pacific Northwest Programs

3 AEC Richland Operations Office

A. Brunstad
W. E. Lotz
C. L. Robinson

2 Atlantic Richfield Hanford Company

G. R. Kiel
ARHCO Files

3 Battelle Memorial Institute

No. of Copies

8 Douglas United Nuclear

J. E. Mecca
N. R. Miller
W. F. Nechodom
R. W. Reid
J. W. Riches
D. L. Renberger
J. R. Spink
DUN Files

64 Battelle-Northwest

F. W. Albaugh
J. M. Batch
A. L. Bement
S. H. Bush
J. J. Cadwell
L. A. Carter
T. T. Claudson
D. L. Condotta
G. J. Dau
F. G. Dawson
D. R. de Halas
R. F. Foster
J. C. Fox
J. J. Fuquay
W. A. Haney
H. Harty
M. M. Hendrickson
R. G. Hoagland
J. F. Honstead
P. A. Hutton
R. T. Jaske
B. M. Johnson (2)
R. L. Junkins
H. V. Larson
R. D. Leggett
J. M. Nielson
R. E. Nightingale
D. P. O'Keefe
H. M. Parker
D. W. Pearce
L. T. Pedersen
H. N. Pederson
A. M. Platt
D. L. Reid
R. L. Richardson
W. D. Richmond
G. J. Rogers (10)
L. C. Schwendiman
D. E. Simpson
J. C. Spanner
E. E. Voiland
R. G. Wheeler
J. A. Williams
N. G. Wittenbrock
D. C. Worlton
Patent Section (2)
Technical Information Files (5)
Technical Publications (3)